

# FIBRE CAVITIES FOR MICROCAVITY POLARITONS

By

Andrew Wood

A THESIS SUBMITTED TO MACQUARIE UNIVERSITY  
FOR THE DEGREE OF MASTER OF RESEARCH  
DEPARTMENT OF PHYSICS  
FEBRUARY 2015



MACQUARIE  
UNIVERSITY

SYDNEY ~ AUSTRALIA



Except where acknowledged in the customary manner, the material presented in this thesis is, to the best of my knowledge, original and has not been submitted in whole or part for a degree in any university.

---

Andrew Wood



# Acknowledgements

This past year, the challenges I have met have tested me as a physicist and as a person. There were times where I didn't think I was ready or able to do what was asked of me, but through the support of so many, I finished what I started. I would first then like to thank my friends. The times when you let me vent when things were not going well as well as providing me with much needed distractions, helped me from not giving up. I'm sorry that work always seemed to get in the way of things.

To the engineers down in METS, especially Ben. You have my tremendous thanks for helping me design and build the components needed for this project. Your guidance in the design process, precision engineering as well as always having time for me when I came running back repeatedly with problems, enabled me to get this intricate concept into a working project.

My deep gratitude and thanks goes to my parents, brother and sisters. Your love, thoughtfulness, emotional support and confidence kept me propped up and moving forward when it felt like everything was going wrong. You all bore the brunt of my frustrations and I appreciate your understanding and comforting advice. I'm sorry that I wasn't there more to be more apart of the family.

To Mr Egan. Although we didn't see much of each other this year, every time we talked, you told me that I, and the work I was doing, was important and that there was a hand always out stretched to help. Your motivation and trust in me gave me the confidence to complete this year and for that you have my sincere thanks. I hope that this work here has justified your faith in me.

As and extra ear to pull, many many thanks to Carlo, Mathieu and Luke. Your opinions and help with my many problems ranging from optics instrumentation to understanding equations to performing AFM scans allowed me to understand and improve the work that I was undertaking.

Although I only worked with you a couple of times, a great thank you to Andreas for the initial working design for the FIMS project. Your ingenuity and versatility in your design allowed us to develop a successful system, the first of its kind in this country. I hope you're proud of what we accomplished.

To my good mates, Tom and Daniel. Your constant hilarious jokes and conversations as well as your unending help with creating graphs, running code and not breaking physics, kept me from not cracking under the strain. Your time and friendship was invaluable to me and you have my greatest thanks. I hope you both do very well in your theses.

I would lastly like to give my most heartfelt thanks and gratitude to Nitin, Ben and Thomas. To Nitin, I don't know how you put up with me in the lab for so long, but without

your help with solving technical problems, performing measurements and finally making these fibres, I would simply not have been able to do this project. Thank you so very much for your support in getting me through this, especially when I thought I couldn't. To Ben, your guidance and knowledge helped me learn and understand what I was doing, why I was doing it and how it all worked. I look back and see how much I have learnt from you and, although I still have a lot to learn, you have given me a firm, working understanding of the physics behind these polariton systems. My greatest thanks for being a mentor for me this year. Also, a big thank you Ben for providing the python programme we used to characterise the indentation. Without it, we would have struggled.

And finally, to Thomas. I don't know what you saw in me that made you take me onto the team, but you never lost faith in what I could do, even when I had. My deepest and profound thanks for the words of encouragement, answers to stupid questions, re-answering those stupid questions when I forgot, helping me understand the physics, checking I was doing alright and not getting too angry when I broke something. Thanks for being my mentor and friend and making me feel that I can do it. I hope the work we have worked hard for this year has justified your confidence in me and bears much fruit.

To everyone again a tremendous thank you.

*“By three methods do we learn wisdom: First, by reflection, which is noblest; second, by imitation, which is easiest; and thirdly, by experience, which is the bitterest.”*

*– confucius*



# Abstract

This thesis reports on the implementation of a CO<sub>2</sub> laser-machining setup for making smooth concave mirror substrates at the end of optical fibres. Once coated with a highly-reflective DBR mirror (reflectivity larger than 99.9999%), the mirrors serve as one end of an open, tunable fibre coupled microcavity, so called fibre cavities. The main characteristic of the mirror substrates machined with the present setup is their very small curvature radius in the range of 8-10 $\mu$ m. Through systematic variation of the main laser parameters, such as pulse duration, power and position of the beam waist a large parameter range can be accessed. Beside the capability for making small mirror substrates, other key features of the setup include the high reproducibility and the large number of fibres that can be machined and analysed in parallel. An integrated interferometric setup allows for *in-situ* analysis of the machined fibre surfaces. In the course of this work, a first batch of 96 fibres, mainly with small curvature radii, was fabricated and sent for coating. The small curvature radii achieved with the setup are expected to be favourable for the realization of the polariton blockade effect with semiconductor quantum-well polaritons.



# Contents

Acknowledgements	v
Abstract	ix
<b>1 Introduction</b>	<b>1</b>
<b>2 Single Emitter Cavity-QED</b>	<b>6</b>
2.1 Jaynes-Cummings Model . . . . .	6
2.2 Weak and Strong Coupling Regime . . . . .	10
2.3 Photon Blockade . . . . .	11
2.4 Quantum Dots . . . . .	14
<b>3 Cavity-QED with Quantum Well Polaritons</b>	<b>18</b>
3.1 Quantum Wells . . . . .	18
3.1.1 From N Quantum Emitters coupled to a cavity mode to two coupled harmonic oscillators . . . . .	19
3.1.2 2D Microcavity Polaritons . . . . .	21
3.2 Polariton Interaction . . . . .	24
3.2.1 Polariton Blockade . . . . .	24
3.2.2 Polariton Confinement . . . . .	27
3.3 Fabry-Pérot Fibre Microcavities . . . . .	29
3.3.1 Gaussian Optics and $TEM_{00}$ Fundamental Mode . . . . .	29
3.3.2 The Optical Resonator . . . . .	30
3.3.3 Fibre Microcavities . . . . .	32
<b>4 Fabry-Pérot Fibre Microcavity Fabrication</b>	<b>34</b>
4.1 Fibre Imaging and Machining System - FIMS . . . . .	35
4.2 CO <sub>2</sub> Laser Ablation System . . . . .	37
4.2.1 Laser Interferometry Imaging System . . . . .	40
4.3 Fibre Indentation Analysis . . . . .	46
4.3.1 Multiple Fibre Holder . . . . .	50
4.4 Distributed Bragg Reflectors (DBR) . . . . .	51
<b>5 Results</b>	<b>56</b>
5.1 Next Steps . . . . .	64

<b>6 Future Work</b>	<b>68</b>
<b>References</b>	<b>70</b>

# Chapter 1

## Introduction

The field of cavity-quantum electrodynamics (cavity-QED or cQED) focuses on light-matter interactions at the quantum level with one or more two-level quantum emitters coupled to a single radiation field mode of an optical cavity [1]. When the coupling rate between emitter and cavity mode exceeds the dissipation rates due to cavity and emitter decay, the system enters the strong coupling regime of cavity QED. As a result of strong coupling, a set of new eigenstates or dressed states arises, so-called *polaritons*, which are a coherent superposition of the quantum emitter and the cavity field. Polaritons can be viewed as quasi-particles that are half-light/half-matter in character with distinct spectral separation. With the ability to probe polaritons through their photonic component and possibly the presence of strong interactions mediated through the matter-part of the dressed state, polariton systems are both interesting from a fundamental point of view but also for a range of possible applications. In particular, engineering of polariton systems exhibiting strong single-photon non-linearities, i.e. systems where the response to light can be altered through the presence of a single photon, is a primary goal in the field. Applications range from quantum information processing with light [2] to quantum simulations in coupled non-linear cavity arrays [3–5] for the exploration of new material systems and phase transitions. In this sense, polariton systems, which are the main context/focus of this Masters thesis, are a prime example for an engineered quantum system with the potential for real-world impact. This introduction gives a short overview of the main concepts and the main development in cavity QED/polaritonic systems over the past decades with a main focus on semiconductor systems which are clearly desirable in light of applications.

**Single Emitter Cavity-QED** The most fundamental system for light-matter interaction is the single, two level quantum emitter coupled to a single cavity mode. For a system far in the strong coupling regime, the resulting excitation spectrum, called the Jaynes-Cummings ladder of excitations [6], is anharmonic at the single-photon level. This anharmonicity is directly inherited from the anharmonic two-level nature of the quantum emitter and is ultimately due to the quantization of the cavity field. A direct consequence of this anharmonicity is the non-linear behaviour of single photons. Due to energy mismatch, a first photon resonant with the fundamental polariton transition will block the entrance of a second photon of the same colour into the system. This effect is called photon blockade [7] and was

termed in analogy to the electron blockade effect in condensed matter. Photon blockade was first demonstrated using caesium atoms in a Fabry-Perot cavity in 2005 [8] by looking at the photon statistics of photons transmitted through the cavity: Since there is only ever one photon in the cavity, the photons exhibit strong anti-bunching. Shortly after this discovery, photon blockade was also demonstrated with atoms coupled to toroidal cavities [9] and at about the same time first traces of quantum correlations were detected for a quantum dot (QD) strongly coupled to a photonic crystal cavity [10]. Clear photon blockade in quantum-dot cavity QED, however, was only demonstrated in 2012 [11]. In the microwave domain, photon blockade was observed with superconducting qubits coupled to stripline resonators [12]. Meanwhile, several experiments working with semiconductor quantum dots in microcavities have made use of the strong (single-photon) non-linearities to demonstrate potential applications in ultrafast single-photon switching [13–16] and quantum information processing [2]. Quantum dots coupled to so-called photonic-crystal cavities that confine light on extremely small length scales are ideal candidates to observe ultrafast conditional dynamics for photons due to their large coupling strength combined with relatively fast cavity decay rate. While being ideal in many ways, quantum dots unfortunately suffer from a major drawback due to the random nature of the quantum-dot growth process: their fundamental transition frequencies and their spatial position exhibit a strong variability hindering the easy scalability of coupled QD-cavity systems to coupled, non-linear many-cavity systems. Hence, for realizing the anticipated applications that rely on identical non-linear coupled systems, a different approach, preferably also on a semiconductor chip, is desirable.

**Multi-emitter cavity QED with quantum wells** Alternative semiconductor systems with the potential to provide strong non-linearities for photons are quantum-well (QW) cavity polaritons in micro-cavities. These half-matter/half-light quasi particles are formed by the collective coupling of 2D quantum-well excitons to a planar micro-cavity. The first experimental demonstration of quantum-well cavity polaritons in a planar DBR micro-cavity was reported in a seminal paper by Weisbuch *et al.* [17]. Since then, the QW polariton field has been highly active. Due to the collective nature of the coupling and the underlying bosonic nature of the quantum-well excitons, however, quantum-well cavity polariton systems are intrinsically linear in the low excitation regime. While this absence of intrinsic non-linearity is not ideal for easily creating single-photon non-linearities, other experimentation is possible. In particular, cavity polaritons are an ideal system to demonstrate Bose-Einstein condensation in the solid state [18]. We briefly turn our attention to this very active branch of research before returning again to the question of single-photon non-linearities:

Due to their photonic nature, quantum-well cavity polaritons have a very small effective mass, several orders of magnitude smaller than that of a single atom. This means that Bose-Einstein condensation of polaritons should occur at normal cryogenic temperatures in stark contrast to the case of atomic BECs [19, 20]. In 2006, Kasprzak *et al* [21] published observations consistent with the formation of a polariton BEC in a semi-conductor micro-cavity containing CdSe quantum wells. In traditional atomic BEC, the temperature is the main factor driving the phase transition as the atoms are in thermal equilibrium. In contrast, the polaritons have a very short lifetime on the order of a few picoseconds. This would not enable the polariton gas to reach thermal equilibrium. However, exciton-exciton interactions

[22], which lead to a blue-shift of the polariton energy, are shown to be fast enough to quasi-thermalize the polariton gas compensating for the continuous leaking of polaritons (or rather photons) out of the cavity. To replenish polaritons lost out of the system and to encourage a high-enough interaction rate between polaritons, large polariton densities are needed. This requires high excitation power indicating that the excitation laser power is the driving factor behind the formation of polariton BEC rather than temperature as in the atomic case. Under non-resonant, high-power excitation, the polaritons relax down into the lower polariton branch via phonon emission and into the system ground state, forming a nonequilibrium BEC.

A main drive in polariton research after the initial demonstration of polariton BEC by several groups [21, 23, 24] was aimed at revealing the quantum fluid behaviour of polaritons [25]. In the following years, experiments reported the observation of superfluid or frictionless flow around obstacles [26], the observation of Bogoliubov excitations [27, 28], Josephson oscillations [29], vortices [30–32] and solitons [33] all highlighting the quantum-fluid nature of weakly-confined polaritons. While for all of these phenomena, including the formation of BEC itself, polariton interactions are essential, the parameters in these experiments were such that the polariton ensembles were still in the so-called weakly interacting regime [25]. However, for the purpose of this work, we are particularly interested in the opposite limit, the regime of strong interactions between single polaritons.

**Quantum-well cavity polariton blockade** The regime of strong polariton interactions was first anticipated in a paper by Verger et al in 2006 [34]. In this paper, the authors sketch the idea of polariton blockade that is somewhat reminiscent of the Rydberg blockade effect in atomic physics [35]: The basic idea is to engineer the photonic part of the wavefunction of quantum-well cavity polaritons through strong confinement of the cavity mode and at the same time keep the quality factor of the cavity high. The strong confinement results in a strong overlap integral between two polaritons leading to an enhanced non-linear interaction coefficient. As a result, the two-polariton state experiences a strong interaction shift. On the other hand, assuming the dominant polariton loss channel to be given by the leakage of photons out of the cavity, a high Q-factor ensures a narrow linewidth for the two-polariton state. If the polariton interaction strength exceeds the linewidth, the resulting polariton excitation spectrum becomes anharmonic. Hence, a first photon resonantly exciting a polariton in the system will block the entrance of a second photon of the same colour due to the strong polariton-polariton interaction hence the term polariton blockade. As in the case of photon blockade, the signature would be the observation of anti-bunching for resonantly scattered/transmitted photons. A few years after the first prediction of the polariton blockade effect, another proposal suggested to yet enhance polariton interactions even further by addressing a biexciton Feshbach resonance, reminiscent of the Feshbach resonance effect in atomic gases [36]: through the resonant coupling to the bound biexciton state, two interacting polaritons pick up a resonant phase shift that is potentially much larger than in a normal polariton-polariton collision. The authors argue that with the help of a Feshbach resonance, the blockade regime could be accessed more easily and coined the term Feshbach blockade [37]. In 2013, a group in Lausanne reported the first observation of the biexciton Feshbach resonance [38] but could not show blockade in their system. Many groups at present are

actively pursuing research in the direction of polariton blockade but to date the blockade regime has not been reported.

The confinement necessary for achieving polariton blockade can be induced through post-growth engineering of the photonic part but also of the excitonic part of the wavefunction. Exciton confinement has been achieved by controlled application of sample stress [23, 39] and recently by light-induced creation of spatially modulated excitonic reservoirs [40, 41]. In particular the latter method provides very precise control over the potential landscape but the achievable confinement length scales are limited by the excitonic diffusion length of several  $\mu\text{m}$ . Polariton confinement through its photonic part has been demonstrated by the use of mesa structures [42], micropillars [43], photonic-crystal cavities [44] and plasmonic structures [45]. However, these systems typically suffer from enhanced excitonic or photonic losses, once the spatial dimensions approach the  $\mu$ -scale. In addition, their spectral tunability is limited.

**Mechanically tunable confined polariton systems** Very recently, two groups have reported the realization of high-Q mechanically tuneable confined polariton systems based on similar approaches: the main idea is to use only one semiconductor-grown DBR mirror with a single quantum well on top. The second mirror consists of a concave indent either in a glass cover slip [46] or at the end of an optical fiber [47], coated with a highly reflective dielectric DBR coating. The two parts are spatially separated and the distance is controlled using piezo positioners allowing for tuning the cavity resonance frequency and the polariton lifetime. The mirror curvature can be rather small and hence rather strong confinement can be achieved. At the same time, the high-quality coating ensures a high cavity finesse implying a long polariton lifetime. Hence, such mechanically tuneable systems seem favourable for entering the polariton blockade regime. In addition, due to the tunability a detailed study of the Feshbach resonance effect seems feasible.

In this thesis, we pursue the fiber-cavity approach described in Reference [47, 48]. The ongoing work in the Quantum Materials and Applications Group (QMAPP) at Macquarie University is a direct follow-up on the work described in that reference. The main topic of this Masters thesis is the description of a laser machining and fiber imaging setup aimed at the fabrication of improved fibers for polariton experiments. In particular, the fibers made with the new setup exhibit much smaller curvature radii than before which should enable much stronger polariton confinement. The improved fibers described in this work together with a new batch of samples showing less disorder than described in Reference [47] will allow for a new generation of polariton experiments.

**Scope of this thesis** The thesis is structured as follows:

**Chapter 2** introduces the physics of a single quantum emitter coupled to a single mode of a cavity. The conditions for reaching strong coupling are discussed. Next, the effect of photon blockade is introduced, and quantum dots as prime semiconductor systems exhibiting strong single-photon non-linearities are presented.

**Chapter 3** starts off by exploring a simple model for the coupling of many emitters to a single cavity mode. Quantum well polaritons are introduced and after a short discussion of a typical polariton dispersion relation and polariton interactions, the effect of polariton

blockade is discussed. The chapter ends with a detailed description of fibre Fabry-Perot micro-cavities including a discussion of the relevant parameters for entering the blockade regime.

In **Chapter 4**, the experimental assembly for our fibre laser machining is presented. The analytical tools used to characterise the machined fibres are introduced. The chapter closes with a discussion of the ideal Bragg layers for the anticipated polariton experiments.

**Chapter 5** presents the results from a detailed characterization of the first batch of fibres machined with the newly built setup. The analysis reveals small curvature radii down to  $\sim 8\text{-}10\mu\text{m}$ .

Finally, **Chapter 6** concludes with an outlook and gives a broader perspective on the possible directions of research opened up by the work described in this thesis.

# Chapter 2

## Single Emitter Cavity-QED

In this chapter, the physics of a single, two-level quantum emitter coupled to the electromagnetic field of a single cavity mode is described using the Jaynes-Cummings model (section 2.1). This description is followed by studying the results from the Jaynes-Cummings model in the strong coupling regime of CQED (section 2.2), introducing the known anharmonic Jaynes-Cummings energy ladder. Based on the anharmonicity of the Jaynes-Cummings ladder, the effect of photon blockade (section 2.3) is introduced and a particular realisation with semiconductor Quantum Dots is discussed (section 2.4).

### 2.1 Jaynes-Cummings Model

The two-level quantum emitter coupled to a single mode of a radiation field is one of the most fundamental systems in quantum physics. Atoms, which are inherently multi-energy level quantum emitters, can be simplified to a two-level energy system. This view can be taken due to the anharmonic nature of the energy level structure. The simplest case then to consider is a single emitter which interacts with a single cavity mode shown in Fig[2.2]. For the strongest interaction, the emitter is placed at an anti-node of the cavity electric field. Although cavities operating at microwave frequencies have been shown to achieve better results in terms of non-linearity, for the scope of this thesis, only optical frequency modes of linear polarisation will be considered. This line of inquiry is taken as there is significant scope for study of these systems in the optical frequencies, even though they do not produce the same quality of results as for the microwave frequencies. Also as a consideration, the detection of photons in the optical frequencies is far easier than those in the microwave frequencies. To study the mechanics of the single emitter interacting with a single cavity mode, the remainder of this chapter will closely follow theory given in [49]. The interaction of the single emitter with the single cavity mode is modelled using the well known *Jaynes-Cummings* model Hamiltonian which has the form of [6],

$$\hat{H}_{JC} = \hat{H}_A + \hat{H}_C + \hat{H}_{int}, \quad (2.1)$$

where  $\hat{H}_A$ ,  $\hat{H}_C$  and  $\hat{H}_{int}$  are the Hamiltonians for the atom, cavity and atom-cavity interaction respectively. The  $\hat{H}_A$  and  $\hat{H}_C$  are defined with the use of the photon creation and

annihilation operators  $\hat{a}^\dagger$  and  $\hat{a}$  and the atomic raising and lowering operators  $\hat{\sigma}_+$  and  $\hat{\sigma}_-$

$$\hat{H}_A = \hbar\omega_A\hat{\sigma}_+\hat{\sigma}_-, \quad (2.2)$$

$$\hat{H}_C = \hbar\omega_C\hat{a}^\dagger\hat{a}, \quad (2.3)$$

where  $\omega_A$  and  $\omega_C$  are the resonant frequencies of the atomic transition and the cavity mode respectively. The  $\hat{H}_{int}$  is the interaction term which describes the interaction between the atom and the cavity field. Under the electric dipole approximation, this Hamiltonian is defined by,

$$\hat{H}_{int} = -e\hat{\mathbf{r}} \cdot \hat{\mathbf{E}}(\mathbf{r}_A), \quad (2.4)$$

where  $-e\hat{\mathbf{r}}$  is the dipole operator which represents the atomic transition and  $\hat{\mathbf{E}}(\mathbf{r}_A)$  is the electric field operator at the point where the atom is situated. Both these operators can be written as follows,

$$e\hat{\mathbf{r}} = \mathbf{d}_{eg}\hat{\sigma}_+ + \mathbf{d}_{ge}\hat{\sigma}_-, \quad (2.5)$$

$$\hat{\mathbf{E}}(\mathbf{r}) = i\sqrt{\frac{\hbar\omega_c}{2\epsilon_0 n^2 V_{eff}}} (\phi(\mathbf{r})\hat{a} - \phi^*(\mathbf{r})\hat{a}^\dagger), \quad (2.6)$$

with  $\mathbf{d}_{eg} = \langle e_a | e\hat{\mathbf{r}} | g_a \rangle$  being the atomic transition dipole element and  $\phi(\mathbf{r})$  the complex electric field wavefunction defined by,

$$\phi(\mathbf{r}) = \frac{\mathbf{E}(\mathbf{r})}{|\mathbf{E}(\mathbf{r}_{max})|}, \quad (2.7)$$

which is given at the position,  $\mathbf{r}_{max}$ , of the maximum of the intra-cavity field. The mode volume,  $V_{eff}$  normalises the electric field operator and is given by,

$$V_{eff} = \iiint \frac{n^2(\mathbf{r})}{n^2} |\phi(\mathbf{r})|^2 d^3r = \iiint \frac{n^2(\mathbf{r})}{n^2} \left| \frac{\mathbf{E}(\mathbf{r})}{|\mathbf{E}(\mathbf{r}_{max})|} \right|^2 d^3r, \quad (2.8)$$

where  $n = n(\mathbf{r}_{max})$  is the index of refraction at the maximum of the cavity field and  $n(\mathbf{r})$  is the position dependent refractive index. By substituting eq. 2.5 and 2.6 into eq. 2.4, the rotating wave approximation (RWA) is now applied [50] by placing the interaction Hamiltonian into the interaction picture. The RWA arises from the interaction Hamiltonian containing different time scales and is a standard approximation for cavity-QED systems. For Eq. 2.4, the time dependent Hamiltonian has the form,

$$\begin{aligned} \hat{H}_{int} = & -\hbar \left( \Omega e^{-i(\omega_c - \omega_A)t} + \tilde{\Omega} e^{i(\omega_c + \omega_A)t} \right) |e\rangle \langle g| \\ & -\hbar (\Omega^* e^{i(\omega_c - \omega_A)t} + \tilde{\Omega}^* e^{-i(\omega_c + \omega_A)t}) |g\rangle \langle e|, \end{aligned} \quad (2.9)$$

where  $\Omega = \hbar^{-1} \mathbf{d}_{eg} \cdot \mathbf{E}_0$  is the Rabi frequency and  $\tilde{\Omega} = \hbar^{-1} \mathbf{d}_{eg} \cdot \mathbf{E}_0^*$  is the counter-rotating frequency. The terms with  $\omega_c + \omega_A$  oscillate at optical frequencies and due to their rapid oscillations, time average to zero. The RWA thus neglects these terms which, upon going

back to the Schrödinger picture, finally leaves the interaction Hamiltonian in the form,

$$\hat{H}_{int} = \hbar g (\hat{\sigma}_+ \hat{a} + \hat{a}^\dagger \hat{\sigma}_-), \quad (2.10)$$

with

$$g = \sqrt{\frac{\omega_C}{2\hbar\epsilon_0 n^2 V_{eff}}} |\phi(\mathbf{r}_a) \cdot \mathbf{d}_{eg}|, \quad (2.11)$$

as the coherent coupling constant for this system. The Hamiltonian for the system can be written in the Jaynes Cummings form as,

$$\hat{H}_{JC} = \hbar\omega_A \hat{\sigma}_+ \hat{\sigma}_- + \hbar\omega_C \hat{a}^\dagger \hat{a} + \hbar g (\hat{\sigma}_+ \hat{a} + \hat{a}^\dagger \hat{\sigma}_-). \quad (2.12)$$

The dressed eigenstates of the system present themselves [49],

$$|g\rangle = |g, 0\rangle, \quad (2.13)$$

$$|n, +\rangle = \cos\theta_n |e, n-1\rangle + \sin\theta_n |g, n\rangle, \quad (2.14)$$

$$|n, -\rangle = \sin\theta_n |e, n-1\rangle - \cos\theta_n |g, n\rangle, \quad n \geq 1, \quad (2.15)$$

with corresponding eigenenergies:

$$E_0 = 0, \quad (2.16)$$

$$E_n^+ = \hbar \left( n\omega_A + \frac{\delta}{2} + \sqrt{ng^2 + \frac{\delta^2}{4}} \right), \quad (2.17)$$

$$E_n^- = \hbar \left( n\omega_A + \frac{\delta}{2} - \sqrt{ng^2 + \frac{\delta^2}{4}} \right), \quad n \geq 1, \quad (2.18)$$

With the detuning  $\delta = \omega_C - \omega_A$  as the difference between the cavity mode frequency and the atomic transition resonant frequency. At  $\delta = 0$  in the lowest manifold of the Jaynes-Cummings ladder, the distinct spectral separation of the normal modes is called the *Vacuum Rabi splitting* ( $\Omega_R = 2g$ ) shown in Fig[2.1]. As a function of detuning, the coupling between the atom and cavity field results in a typical avoided crossing. These eigenstates of the system and their distinct spectral identity are known as *dressed states* which are a coherent super-position of the atom and cavity photon parts. This new system has an intrinsic *anharmonicity* present as the higher manifold energy splitting scales as  $\sqrt{n}$  as shown in Fig[2.1].

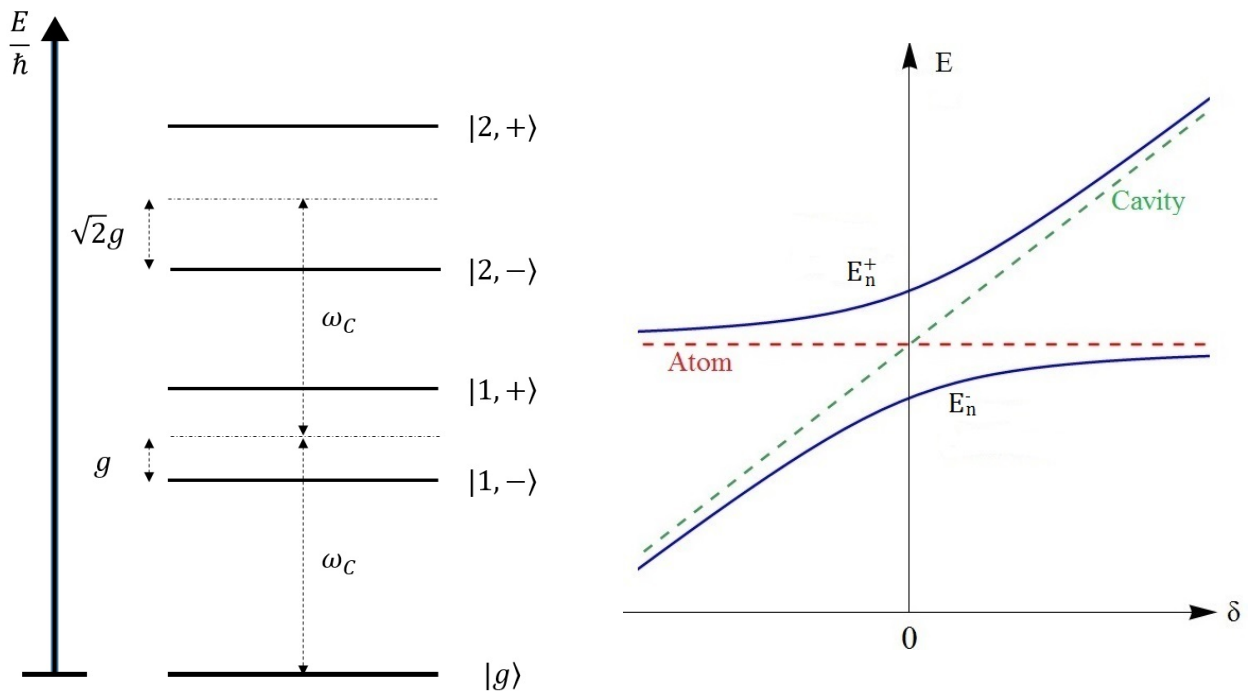


FIGURE 2.1: The left figure shows Jaynes-Cummings energy ladder for the two lowest manifolds at zero detuning. The right figure shows spectral anti-crossing for the first Jaynes-Cummings manifold as a function of detuning. The splitting between first manifold dressed states, on resonance, is  $2\hbar g$ .

## 2.2 Weak and Strong Coupling Regime

All quantum systems suffer from losses which limit the light-matter interactions. In the case of the interaction between the cavity field and the quantum emitter, losses result from different mechanisms. The main sources of loss arise from light escaping from the cavity due to imperfect mirrors at rate ' $\kappa$ '.

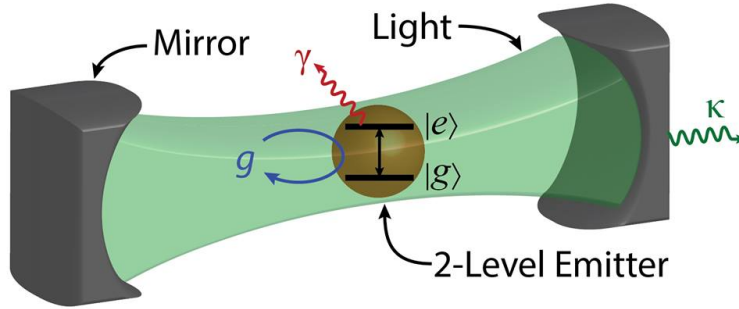


FIGURE 2.2: A two-level quantum emitter, with the ground state  $|g\rangle$  and the excited state  $|e\rangle$  coupled to a cavity mode with coupling strength ' $g$ '. The cavity energy loss rate is given by ' $\kappa$ ' which includes absorption losses and out-coupling through the mirrors. The spontaneous emitter decay rate into free space given by ' $\gamma$ '.

Inside the cavity, the photons are retained only until they are transmitted through, scattered or absorbed by the cavity mirrors. This means that the photons remain confined for a finite time inside the cavity which is described by the exponential decay of the intensity,

$$I(t) = I_0 \exp\left[-\frac{t}{\tau}\right], \quad (2.19)$$

where  $I(t)$  is the intra-cavity intensity at time  $t$ ,  $\tau = 1/\kappa$  is the cavity lifetime and  $I_0 = I(0)$ . The cavity lifetime  $\tau$  can also be described with regard to the Q-factor of the cavity, which is the ratio of the round trip loss of the cavity with respect to the total energy inside the cavity,

$$\tau = \frac{Q}{\omega_C}, \quad (2.20)$$

Where  $\omega_C$  is the frequency of the cavity. However, having some light transmitted by the mirrors is not all together an undesirable trait, as this allows probing to be performed on the system. The other main loss mechanism present is the spontaneous decay of the emitter, which can emit photons into modes other than the cavity mode which are lost to the environment. This loss mechanism occurs at rate ' $\gamma$ '. Cavity and emitter losses need to be considered in the Jaynes-Cummings model. In order to accurately incorporate decoherence into the evolution of the system the master equation must be solved,

$$\frac{\partial \rho}{\partial t} = -\frac{i}{\hbar} [\hat{H}, \rho] + L(\rho), \quad (2.21)$$

which contains the term  $L(\rho)$  which describes the losses of the system and the corresponding dephasing,

$$L(\rho) = \frac{\gamma}{2}(2\hat{\sigma}_-\rho\hat{\sigma}_+ - \hat{\sigma}_+\hat{\sigma}_-\rho - \rho\hat{\sigma}_+\hat{\sigma}_-) + \frac{\kappa}{2}(2\hat{a}\rho\hat{a}^\dagger - \hat{a}^\dagger\hat{a}\rho - \rho\hat{a}^\dagger\hat{a}). \quad (2.22)$$

This expression results in the linear differential equation describing the time evolution of the expectation values  $\langle\hat{\sigma}_+(t)\rangle$  and  $\langle\hat{a}^\dagger(t)\rangle$  [49],

$$\frac{\partial}{\partial t} \begin{pmatrix} \langle\hat{\sigma}_+(t)\rangle \\ \langle\hat{a}^\dagger(t)\rangle \end{pmatrix} = \begin{bmatrix} -\left(\frac{\kappa+\gamma}{4} - i\frac{\delta}{2} - i\omega_a\right) \\ +\left(\frac{\kappa-\gamma}{4} - i\frac{\delta}{2} \quad ig \right) \\ ig \quad -\frac{\kappa-\gamma}{4} + i\frac{\delta}{2} \end{bmatrix} \cdot \begin{pmatrix} \langle\hat{\sigma}_+(t)\rangle \\ \langle\hat{a}^\dagger(t)\rangle \end{pmatrix} \quad (2.23)$$

Solving these linear differential equations describing the time evolution of the expectation values, the complex eigenenergies emerge with the real part [49],

$$E^\pm = \hbar \left( \omega_A + \frac{\delta}{2} \pm \text{Re} \sqrt{g^2 - \left(\frac{\kappa-\gamma}{4} - i\frac{\delta}{2}\right)^2} \right), \quad (2.24)$$

which are the energies of the excited state of the system. The imaginary components describe the corresponding dissipation rates of the system [49],

$$\frac{\Upsilon^\pm}{2} = - \left( \frac{\kappa+\gamma}{4} \pm \text{Im} \sqrt{g^2 - \left(\frac{\kappa-\gamma}{4} - i\frac{\delta}{2}\right)^2} \right). \quad (2.25)$$

From these two equations, it is clear that at zero detuning  $\delta = 0$ , the sign of the square root term will depend on the ratio of  $g$  to  $\frac{\kappa-\gamma}{4}$ . If  $g < \frac{\kappa-\gamma}{4}$ , the square root is imaginary, such that the losses do not allow the formation of polaritons. This scenario is known as the weak coupling regime of cavity-QED. If, on the other hand,  $g > \frac{\kappa-\gamma}{4}$ , the square root is real, thus the coherent coupling of the cavity and emitter dominates over the decoherence of the system. This results in the excited energy levels splitting with the formation of the dressed states. This is known as the strong coupling regime of cavity-QED. To realise a strongly coupled, single atom-cavity system, losses must be minimised by large Q-factors (see eq. 2.24) and the coupling strength ‘ $g$ ’ maximised by reducing the cavity mode volume  $V_{eff}$  (see eq. (2.11)).

## 2.3 Photon Blockade

As was mentioned above, the Jaynes-Cummings ladder is intrinsically anharmonic. This characteristic stems from the quantised nature of the cavity field and the inherent anharmonicity of the two-level emitter. This anharmonicity becomes clear when describing the transition energy from  $n^{th}$  to the  $(n+1)^{th}$  eigenstates of the Jaynes Cummings manifold.

On resonance, this transition energy is given by,

$$E_{n \rightarrow n+1}^- = \hbar(\omega_C - (\sqrt{n+1} - \sqrt{n})g), \quad (2.26)$$

using eq.(2.24). Even though this equation clearly shows the anharmonic separation of the energy levels, the polariton linewidth must also be sufficiently small such that energies are distinguishable between successive transitions. With the polariton linewidth given as  $\hbar\kappa/2$  where  $\kappa$  is the cavity energy loss rate, the ratio of the energy level difference with respect to the linewidth must be greater than one [49],

$$\frac{|E_{0 \rightarrow 1}^- - E_{1 \rightarrow 2}^-|}{\hbar\kappa/2} = 2(2 - \sqrt{2})\frac{g}{\kappa} > 1, \quad (2.27)$$

which is the case when  $g \gg \kappa$ . The rate  $\gamma$  is not included in these calculations as the rate  $\kappa$  is typically the dominant loss mechanism in such systems. One such phenomenon with great potential that has been shown in such non-linear systems is the photon blockade. The photon blockade was first proposed by Imamoglu *et.al.* [7] in 1997, whereby the presence of one photon impedes the transmission of a second photon due to photon-photon interactions mediated through the ‘matter’ part of strongly coupled systems.

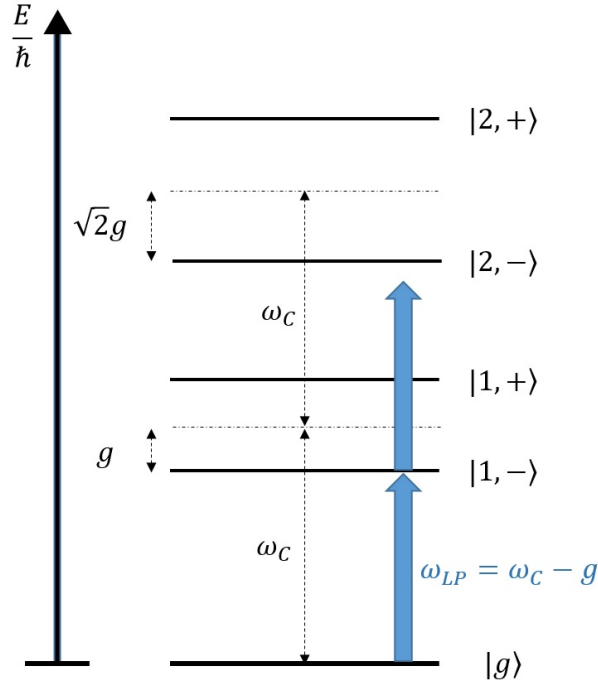


FIGURE 2.3: The Jaynes-Cummings energy ladder showing the two lowest energy manifolds. At zero detuning ( $\omega_C = \omega_A$ ) two photon absorption of the probe field  $\omega_{LP}$  tuned to the lower state of the first energy manifold is inhibited.

In this case, a light field with energy equal to the transition energy of the lower polariton branch of the first Jaynes-Cummings manifold,  $\omega_{LP}$ , drives the lower polariton transition. A

further addition of a photon of frequency  $\omega_{LP}$  into the system, however, would not excite the system into higher energy states as the photon is no longer in resonance with the excitation frequency (see Fig[2.3]). This would result in a phenomenon known as photon anti-bunching. Photon anti-bunching is a characteristic of photon number with sub-Poissonian statistics [51]. Anti-bunching of photons occurs when an emitter only emits one photon at a time which is observed by the use of a Hanbury Brown and Twiss interferometer [52] shown in Fig[2.4].

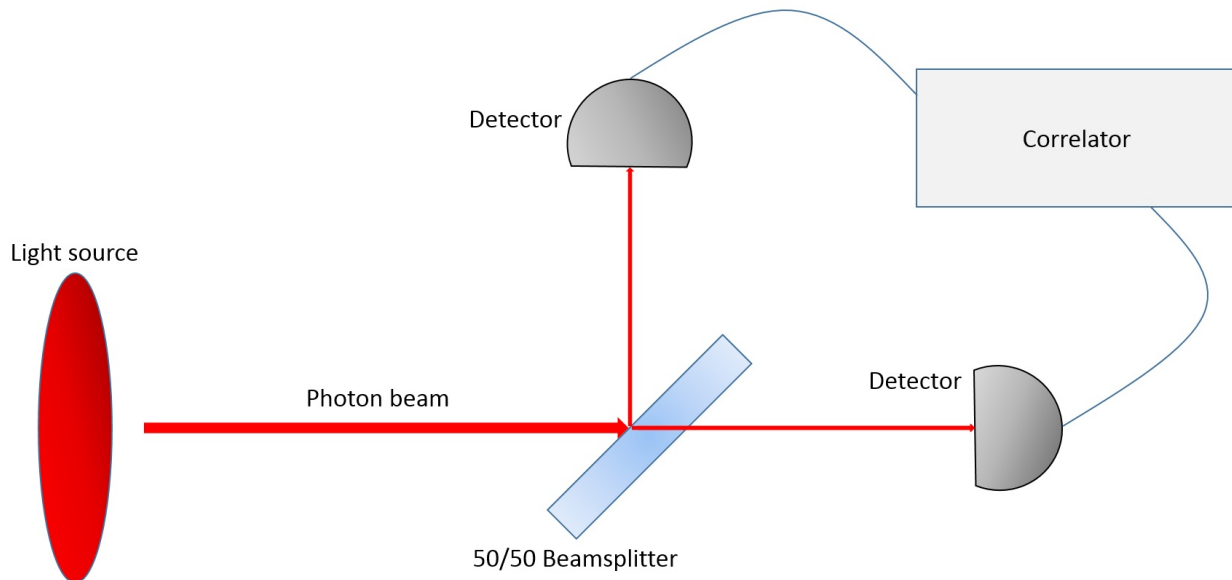


FIGURE 2.4: Hanbury Brown and Twiss interferometer. One detector has a time delay which correlates the photons detected within this time window between the two detectors.

This interferometer functions by the use of two detectors measuring photon numbers after a photon beams passes through a 50/50 beamsplitter. When a photon is detected by one of the detectors, a timer is started which is stopped when the other detector registers a photon. This is known as a coincidence event. Over time, a histogram is formed of the number of coincidence events. The coincidence events as a function of time delay between detectors is represented by the normalised second order auto-correlation function. This function, for a single mode light field is defined by [53],

$$g^{(2)}(t, \tau) = \frac{\langle \hat{a}^\dagger(t) \hat{a}^\dagger(t + \tau) \hat{a}(t + \tau) \hat{a}(t) \rangle}{\langle \hat{a}^\dagger(t) \hat{a}(t) \rangle \langle \hat{a}^\dagger(t + \tau) \hat{a}(t + \tau) \rangle}, \quad (2.28)$$

where  $\hat{a}^\dagger(t)$  and  $\hat{a}(t)$  are the photon creation and annihilation operators respectively. This correlation function stipulates the probability of detecting two photons with a time delay  $\tau$  under both continuous wave (CW) and pulsed laser regimes. Anti-bunching is the situation when photons have a lower probability of arriving at the detectors at the same time. This means that as  $\tau$  approaches zero, there is a distinctive ‘dip’ in the second order auto-correlation function as  $g^{(2)}(0)$  should be smaller than one. The first instance of the photon

blockade was observed using  $g^{(2)}(\tau)$  measurements in 2005 by Birnbaum *et.al.*[8] using Caesium atoms.

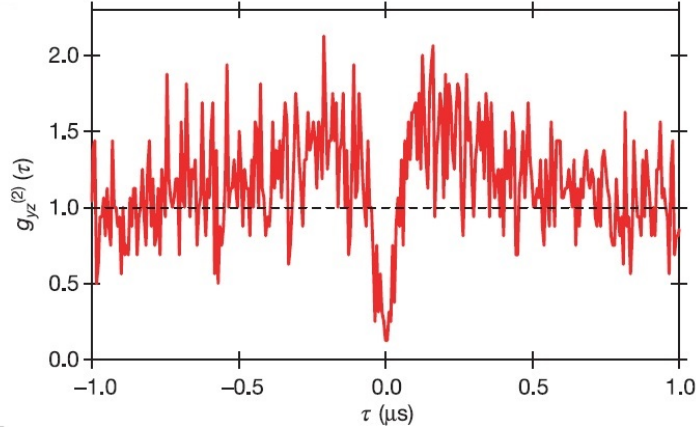


FIGURE 2.5: The second order auto-correlation function for strongly coupled atom-cavity system. Note the pronounced ‘dip’ at  $\tau = 0$  which indicates photon anti-bunching [8]

## 2.4 Quantum Dots

While atom-cavity system have reached an exquisite level of control, in light of applications, there is great emphasis to develop semi-conductor, ‘on chip’ based systems which employ light-emitter interactions. In the past decades, Quantum Dot (QD) technology has proven an alternative into probing coupled, non-linear systems, while maintaining the single, two-level quantum emitter properties of the single atom. Quantum dots are nano-structures composed of semi-conductor materials which exhibit atom like narrow emission lines. The QD is formed by a droplet of low band gap semiconductor material surrounded by a higher band gap semiconductor material, allowing for 3D confinement of electron-hole pair. As such, QD are sometimes referred to as *artificial atoms*. This, together with anti-bunching characteristics [54], QD are ideal candidates for engineering light-emitter interfaces with strong Jaynes-Cummings non-linearity.

**Quantum Dot Growth** Optically active QD are typically grown by Molecular Beam Epitaxy (MBE) [55] and are formed using a ‘self-assembling’ technique [56]. This involves the spontaneous release of mechanical strain of different semi-conductor material to form small ‘droplets’ of low energy gap semi-conductor material, hence the ‘self-assembling’ name. A semiconductor wafer of Gallium Arsenide (GaAs) in an ultra-high vacuum is deposited with Indium (In) and Arsenic (As). Because of a lattice constant mismatch of  $\sim 7\%$  between the GaAs and InAs, the InAs layer is intrinsically strained when grown on a GaAs matrix. This strain can be released by the careful choice of growth temperature and materials such that there is a spontaneous formation of small droplets of InAs at random locations on the wafer [57]. These droplets typically have an in-plane size of 5-20nm and a height of  $\sim 4$ nm which typically varies strongly from QD to QD. A capping layer of GaAs is grown on the

substrate while simultaneously, an “annealing” process takes place to reduce the height of the QD droplet by evaporation. The final step in the fabrication process is the growth of a GaAs protective layer to protect the QD from surface effects, diffusion and oxidation.

**Quantum Dot Energy Level Structure** The different semiconductor materials in QD growth create a potential trap in the structure due to InAs possessing a smaller energy gap ( $\Delta E_g = 0.36eV$ ) compared to the GaAs ( $\Delta E_g = 1.43eV$ ) [58]. The strong confinement provided by the nanoscale band deformation within the QD, leads to a quantised, anharmonic energy level structure for both electron and hole wavefunctions. These ‘electrons’ and ‘holes’ referred to here result from the absorption of a photon equal to or greater than the energy of the energy band gap. Hence, an electron is lifted from the valence band into the conduction band leaving a positive ‘hole’ in the valence band. Due to coulomb attraction, this electron-hole pair form a quasi-particle known as an *exciton* which resembles the configuration of a Hydrogen atom. Eventually, an exciton decays or ‘recombines’, emitting a photon. In the case of QD, confinement of the electron and holes on a size comparable with the exciton Bohr radius  $a_X$ , results in bound exciton states which display distinct transition energies (see fig[2.6]). This occurs by virtue of different charge configurations within the quantised electron-hole structure.

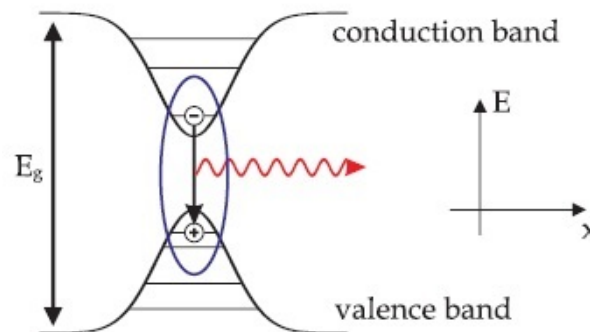


FIGURE 2.6: Excitons in a Quantum Dot. A photon is absorbed by the system, promoting an electron into the conduction band, forming an exciton. Note the discrete energy states within the band structure. Taken from [49].

The most typical form of an exciton state is the **neutral exciton** ( $X^0$ ) which is a single electron-hole pair. This gives rise to four excitonic configurations which are degenerate. The **neutral biexciton** ( $XX^0$ ) is a state occurring from two electron-hole pairs within the QD. However, when one of the electron-hole pairs recombine, the emitted photon is slightly red-shifted in energy to that of the neutral exciton recombination energy by virtue of the complex interactions between the charge carriers which red-shifts the  $XX^0$  line compared to the neutral exciton transition energy. Other excitonic states which can occur are the trion states whereby a net charge is carried by the excitons. In the case of an extra electron present, the creation of an electron-hole pair will form the negatively charged  $X^-$  state with the positively charged  $X^+$  forming due to the presence of an extra hole.

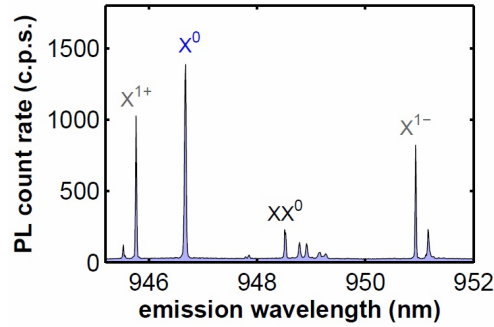


FIGURE 2.7: Quantum Dot spectrum. The peaks show the neutral, biexciton and trion exciton excitations. Taken from [58].

**Photonic-Crystal Microcavities** Implementation of QD into strongly coupled systems requires a means by which photons are confined for a sufficiently long time. A method which has proven highly effective is the photonic-Crystal (PC) microcavity [59]. PC is typically a 2-dimensional dielectric substrate which has holes periodically drilled into it, usually forming a triangle lattice. The periodic lattice structure results in an optical ‘band gap’ in the dispersion relation architecture which inhibits the propagation of all in-plane wave-vectors within this band gap. The incorporation of a defect into the lattice is accomplished by not drilling holes at one or more lattice sites, ensures that wave-vectors within the band gap can only exist within this defect site and do not propagate out. This defect creates the ‘cavity’ with the lattice acting as the ‘highly reflective mirrors’. With careful choice of hole sizes and defect lengths, strong coupling to QD can be achieved in such devices [60].

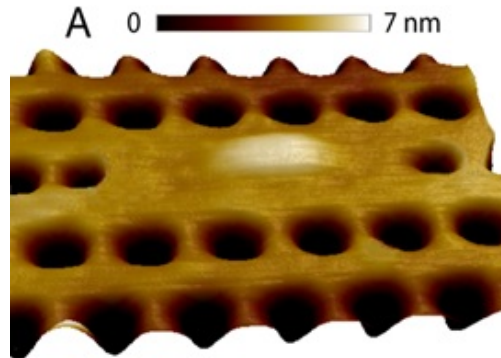


FIGURE 2.8: A photonic crystal microcavity. Note that the white lump is not the QD but the capping layer over QD. Taken from [60].

**Photon Blockade in Quantum Dots** Quantum dots exhibit distinct and well separated energy levels similar to those of the atom and as such, can be treated as a two-level system. This enables the use of the Jaynes-Cummings model to describe the coupling of a cavity field mode to a single quantum emitter as already outlined earlier in this chapter. With the ability to place QD in high Q-factor microcavities, the strong single photon non-linearity has been realised with QDs. While early works have demonstrated some degree of anti-bunching [10],

single photon non-linearity has been shown in the work by Reinhard *et.al.* (2012) [11] where the second order autocorrelation function exhibiting distinct anti-bunching (see Fig[2.9]).

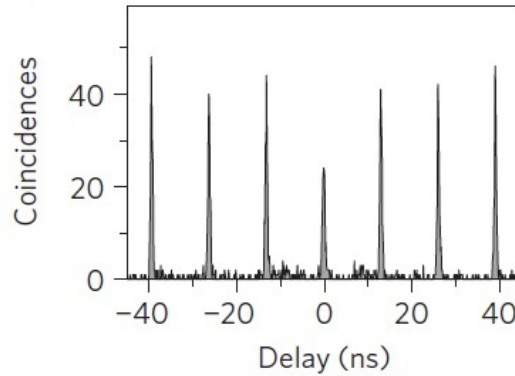


FIGURE 2.9: Auto-correlation graph for a QD in a photonic crystal demonstrating photon anti-bunching under pulsed resonant pumping of the polariton states [11]

QD systems has proven that single photon non-linearities can be realised in fully integrated semiconductor devices. As pointed out in the introduction, the next step towards quantum information processing and quantum simulation would be to scale up the system by coupling several identical cavity-QD systems and to be able to observe nonlinearity in larger systems. However, as mentioned in section 2.4, QD growth occurs randomly on the wafer and can vary greatly in size (see Fig[2.10]). Thus, uniformity is difficult to maintain when attempting to grow QDs [61]. For this reason, QD systems have limited scalability and thus an alternative is needed.

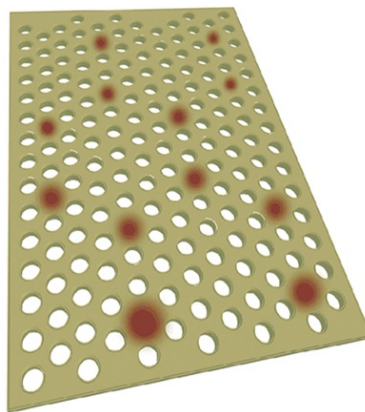


FIGURE 2.10: QDs grown on photonic crystal. Due spontaneous nature of the growth process, QD positioning and sizes are random. Taken from [62].

# Chapter 3

## Cavity-QED with Quantum Well Polaritons

This chapter describes the Quantum Well as a means of scaling up strongly coupled systems. The physics of coupling a quantum well to a single cavity mode is explored by considering the quantum well as a system of  $N$  emitters (section 3.1). Quantum well 2D microcavity polariton generation is then discussed (section 3.1.2). The introduction of nonlinearity originating in polariton-polariton interaction leads into the proposal of the polariton blockade (section 3.2). Finally, Fabry-Pérot fibre microcavities are introduced as an experimental means of accessing the Polariton Blockade (section 3.3).

In the previous chapter, the non-linear capabilities of the Jaynes-Cummings model have been effectively demonstrated in QD systems. However, due to the random nature of the QD fabrication process, the size and placement of the QDs is difficult to control despite extensive efforts using *in situ* lithography [63] and site-controlled QD nucleation [64]. This results in differing spectral qualities from one to another which makes QD unsuited for scaling up these systems. This prompts the step towards using many, two level emitter systems which have greater uniformity in their construction. However, as we will see, in the low excitation regime, anharmonicity is not present for  $N$  two level emitters and thus,  $N$  two level emitters can be considered as a single linear system.

### 3.1 Quantum Wells

Quantum wells (QW) are ideal structures for an  $N$  emitters system whose parameters are considerably easier to control when they are grown, unlike the QDs mentioned previously. The QW is a two dimensional planar structure composed of layered, low energy band-gap semiconductor material sandwiched between high energy band-gap material, for example, InGaAs sandwiched between GaAs, with a thickness close to the exciton (see section 2.4) Bohr radius  $a_X \sim 10$  nm (see Fig[3.1]). This layering creates a potential well, quantising the energy level structure in the growth direction.

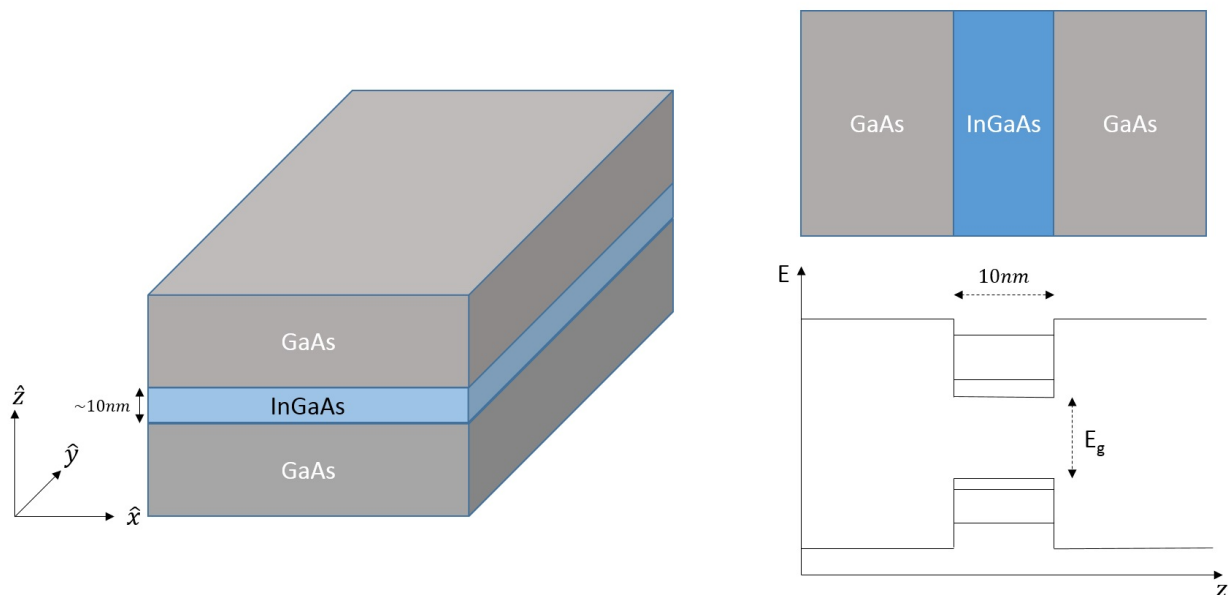


FIGURE 3.1: Quantum Well structure. Confinement in the growth direction ( $z$  axis), quantises the exciton energy levels in one dimension. Excitons are free to move in the  $XY$  plane.

However, excitons have free movement in-plane unlike QD, which confines excitons in all three dimensions. This allows the creation of several excitons within the QW. As a first approximation, these excitons can be considered as a system of  $N$  two level emitters. As we will see, the  $N$  emitters can be approximated by a harmonic oscillator in the low excitation regime. Indeed, because of the charge carriers that compose the exciton are able to be delocalised over a distance greater than the Bohr radius  $a_X$ , the Pauli exclusion principle will begin to take effect when the 2D density  $d_X$  is such that  $d_X^{-\frac{1}{2}} \gtrsim a_X$ . As QW excitons can occupy the same quantum state at low densities, they can be considered a boson like particle.

### 3.1.1 From $N$ Quantum Emitters coupled to a cavity mode to two coupled harmonic oscillators

To describe the QW in a strongly coupled light-matter interface, the following theory draws extensively from [49]. For the strongly coupled system, the QW can be viewed as a system of  $N$  two-level emitters interacting with a single cavity mode. It is assumed that the emitters do not interact with each other and couple with the same strength ' $g_0$ ' to a single cavity mode. The atomic occupation states are given by the Dicke states in the spin angular momentum

basis [49],

$$\{|m\rangle\}, \quad m = -\frac{N}{2}, -\frac{N}{2} + 1, \dots, \frac{N}{2} - 1, \frac{N}{2}, \quad (3.1)$$

$$\left| -\frac{N}{2} \right\rangle = |g\rangle_1 |g\rangle_2 \dots |g\rangle_N,$$

$$\left| \frac{N}{2} \right\rangle = |e\rangle_1 |e\rangle_2 \dots |e\rangle_N, \quad (3.2)$$

$$\left| -\frac{N}{2} + 1 \right\rangle = \frac{1}{\sqrt{N}} \sum_{j=1}^N |g\rangle_1 |g\rangle_2 \dots |e\rangle_j \dots |g\rangle_N,$$

where the subscript ‘ $j$ ’ is the exciton label. The states  $\left| -\frac{N}{2} \right\rangle$  and  $\left| \frac{N}{2} \right\rangle$  define the all the emitters in the ground ( $|g\rangle_j$ ) and excited ( $|e\rangle_j$ ) states respectively. For instance the state  $\left| -\frac{N}{2} + 1 \right\rangle$  describes a single excitation shared by all the emitters. The angular momentum operators,  $\hat{J}_z, \hat{J}_+$  and  $\hat{J}_-$  which are the pseudo-spin, raising and lowering operators respectively, describe the system of  $N$  emitters defined as,

$$\begin{aligned} \hat{J}_z |m\rangle &= m |m\rangle, \\ \hat{J}_+ |m\rangle &= \sqrt{\frac{N}{2} \left( \frac{N}{2} + 1 \right) - m(m+1)} |m+1\rangle, \\ \hat{J}_- |m\rangle &= \sqrt{\frac{N}{2} \left( \frac{N}{2} + 1 \right) - m(m-1)} |m-1\rangle, \end{aligned} \quad (3.3)$$

with,

$$\hat{J}_- \left| -\frac{N}{2} \right\rangle = \hat{J}_+ \left| \frac{N}{2} \right\rangle = 0. \quad (3.4)$$

The ensemble of  $N$  emitters coupled to a single cavity mode is then described by the Tavis-Cummings Hamiltonian given by [65],

$$\hat{H} = \hbar\omega_A \hat{J}_z + \hbar\omega_C \hat{a}^\dagger \hat{a} + \hbar g_0 (\hat{a} \hat{J}_+ + \hat{a}^\dagger \hat{J}_-) \quad (3.5)$$

where  $\omega_A$  and  $\omega_C$  are the resonant atomic and cavity frequency respectively,  $\hat{a}^\dagger$  and  $\hat{a}$  are the creation and annihilation operators respectively. The entire system in the uncoupled basis of the emitters and cavity mode can be defined by the tensor product of the Dicke and Fock states  $|m\rangle \otimes |n\rangle = |m, n\rangle$ . The eigenstates emerging from the coupling of the cavity mode to the excitons are called polaritons. On resonance ( $\omega_A = \omega_C$ ), the polaritonic states for a single quanta of energy, can be shown to be [49],

$$\begin{aligned} |\Psi_1^{+1/2}\rangle &= \frac{1}{\sqrt{2}} \left( \left| -\frac{N}{2}, 1 \right\rangle + \left| -\frac{N}{2} + 1, 0 \right\rangle \right), \\ |\Psi_1^{-1/2}\rangle &= \frac{1}{\sqrt{2}} \left( \left| -\frac{N}{2}, 1 \right\rangle - \left| -\frac{N}{2} + 1, 0 \right\rangle \right), \end{aligned} \quad (3.6)$$

with the corresponding eigenenergies,

$$\begin{aligned} E_1^{+1/2} &= \hbar(\omega_A + \sqrt{N}g_0) && \text{Upper Polariton,} \\ E_1^{-1/2} &= \hbar(\omega_A - \sqrt{N}g_0) && \text{Lower Polariton.} \end{aligned} \quad (3.7)$$

The Vacuum Rabi splitting for N emitters is thus given as [49],

$$\Delta E = 2\sqrt{N}\hbar g_0, \quad (3.8)$$

with the energy separation scaling with  $\sqrt{N}$ . For larger numbers of quanta  $q$  (still with  $q < N$ ) in the system, the number of eigenstates of the system scales as  $q + 1$ . For these states, the eigenenergies are given as [49],

$$E_q^s = \hbar(q\omega_A + 2s\sqrt{N}g_0), \quad s = -\frac{q}{2}, -\frac{q}{2} + 1, \dots, \frac{q}{2}. \quad (3.9)$$

This shows that transition energies for successive manifolds are  $\Delta E = \hbar(\omega_A \pm \sqrt{N}g_0)$  which clearly shows the linearity of the polariton states. The inherent linear nature of N emitter systems is in stark contrast to the single emitter case. In the low excitation regime, this system of N two level emitters can be considered as a single linear system which has boson like properties. When this view is taken, the model of N emitters coupled to a cavity mode is equivalent to the two coupled harmonic oscillators model (Holstein Primakoff approximation [66]). The collective coupling constant ‘ $g_{QW}$ ’ is defined by,

$$g_{QW} = \sqrt{N}g_0. \quad (3.10)$$

This shows a marked increase in comparison with the single emitter coupling constant ‘ $g_{QD}$ ’ (see eq.(2.11)) due to the collective coupling of N emitters. The energy splitting between polariton states can therefore be written as [49],

$$\Delta E = 2\hbar g_{QW} = 2\hbar \sqrt{\frac{4\pi\omega_C f_{2D}}{L_{eff}}} |\phi(\mathbf{r}_a)|, \quad (3.11)$$

where  $f_{2D}$  is the oscillator between the two-dimensional QW exciton and cavity field,  $L_{eff}$  is the effective cavity length and  $\phi(\mathbf{r}_a)$  is the transverse complex electric field function.

### 3.1.2 2D Microcavity Polaritons

Quantum well structures requires a large intensity light field with small cavity lengths to achieve high coupling strengths. One means of providing these requirements is an optical microcavity. A microcavity is very small optical resonator, whose length is on the order of the wavelength of light. This feature facilitates the creation of large electric fields, confining the field along the longitudinal axis. As we are interested in semiconductor emitters, one way is to build the microcavity directly around them. This result in a fully integrated, solid state design. A solid state microcavity is made of two mirrors sandwiching the emitter.

The mirrors are made by layers of semiconductor materials known as Distributed Bragg Reflectors (DBR) (see section [4.4]) and the emitter placed at one antinode of the field as shown in Fig[3.2].

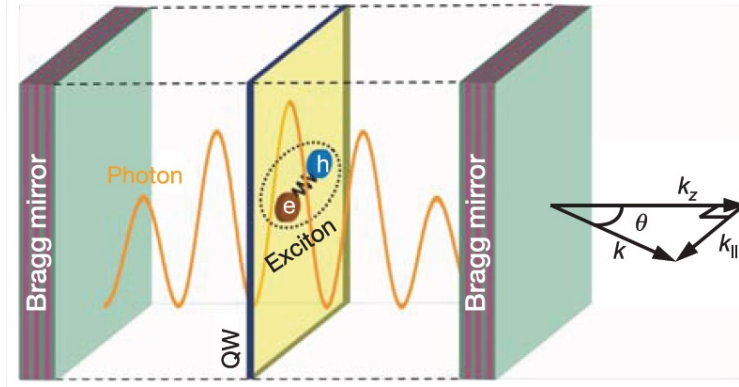


FIGURE 3.2: 2D microcavity formed by a QW in between two DBR mirrors. The QW is placed at the anti-node of the electric field to ensure maximum coupling between the 2D excitons and cavity field. The polariton dispersion curves can be obtained using angle resolved photoluminescence. Taken from [21].

The DBRs provide a high reflectivity of the cavity field, ensuring large electric fields are maintained inside the cavity. Due to the 2D symmetry of the microcavity, the in-plane wavevector  $\vec{k}_{\parallel}$  is conserved and the eigenstates of the system can be expressed in the wavevector basis. So the eigenenergies of the system can be written in terms of the in-plane wavevector of the excitons and cavity photons [49],

$$E^{\pm}(\vec{k}_{\parallel}) = \frac{\hbar}{2}(\omega_C(\vec{k}_{\parallel}) + \omega_X(\vec{k}_{\parallel})) \pm \hbar\sqrt{g_{QW} + \frac{1}{4}(\omega_C(\vec{k}_{\parallel}) - \omega_X(\vec{k}_{\parallel}))^2}, \quad (3.12)$$

where  $\omega_C(\vec{k}_{\parallel})$  and  $\omega_X(\vec{k}_{\parallel})$  are the cavity and exciton in-plane dispersion relations respectively. In 1992, Weisbuch *et.al.* [17] recorded the first observations of polaritons in a QW semiconductor microcavity achieving strong coupling through the detection of normal mode splitting shown in Fig[3.3].

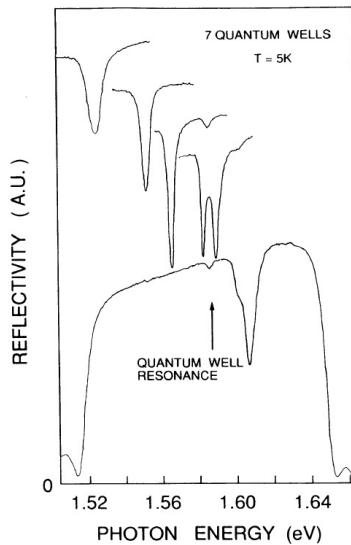


FIGURE 3.3: Reflection spectra showing the exciton-photon mode splitting in a seven QWs microcavity. Taken from [17].

Because of the in-plane wave vector dependence on the polariton energy, the dispersion for such a system can be obtained using angle resolved photo-luminescence spectroscopy (see Fig[3.4]), as

$$\vec{k}_{\parallel} = \frac{\omega}{c} \sin\theta. \quad (3.13)$$

This technique involves the pumping the system with a high photon energy such that electrons are excited into high energy states. The electrons relax down into the lowest energy state via phonon emission, where they recombine and emit photons. By measuring the in-plane momentum and energy of the photons escaping the microcavity, the polariton dispersion can be obtained (see Fig[3.4]).

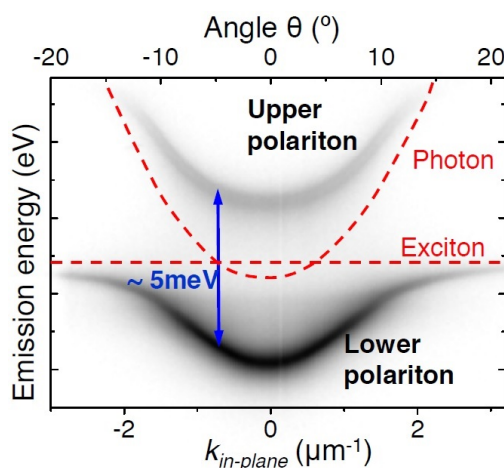


FIGURE 3.4: Angle resolved photoluminescence spectroscopy of the upper and lower branch 2D Quantum well polaritons. The dashed lines show the bare photon and exciton energies. Taken from [67].

From polariton dispersion, one can extract the effective mass of the polariton which is given by [68],

$$k_B T_C \sim \frac{\hbar^2 n_{eff}}{2m_P} \quad (3.14)$$

where  $n_{eff}$  is the effective refractive index. Polariton mass is on the order of  $\sim 10^{-4}m_e$ . The bosonic character of polaritons and their very low mass (orders of magnitude smaller than atoms) make polaritons ideal for Bose-Einstein condensation (BEC), even at high temperatures. Indeed, in 2006, Kasprzak *et.al.* [21] observed the Bose-Einstein condensation of exciton-polaritons in microcavity containing CdSe QWs (see Fig[3.5]).

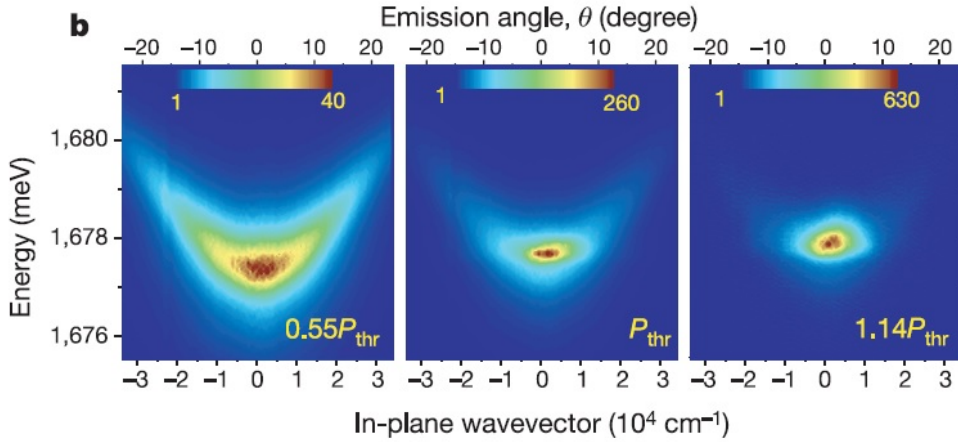


FIGURE 3.5: The energy and angle resolved emission from microcavity polaritons for increasing pump power. The far right image shows polariton condensation. Taken from [21].

Together with BEC of polaritons, the quantum behaviour of polaritonic systems was studied [26]. However these experiment were carried out in the weakly interacting regime. To be able to exploit a nonlinearity in polaritonic systems, one needs to increase polariton interactions. As we will see, this could be achieved through in-plane confinement leading to zero dimensional (0D) polaritons.

## 3.2 Polariton Interaction

### 3.2.1 Polariton Blockade

Strongly coupled systems using QW have been shown to have a distinct linear structure at low system energies, unlike the single emitter QD. However, if non-linearity could be introduced into this linear system, the polariton equivalent of the photon blockade could be achieved without the non-uniformity and coupling issues of the QD [11]. In 2008, Verger *et.al.* [34] proposed a polariton quantum blockade effect, a non-linear phenomenon, which could be realised in QW polaritons. They theorised that by having strong polariton-polariton interactions through its excitonic part, that this will blue shift the polariton resonant frequency such that the presence of one polariton inhibits the injection of another polariton.

Unlike the photon blockade where non-linearity is due to the anharmonic Jaynes-Cummings energy ladder, the polariton blockade relies on nonlinearity due to interactions. In previous discussions, interactions between emitters and hence excitons, have been excluded from consideration to describe the dynamics of the strong coupling of quantum emitters to a single cavity mode. This, in reality, is not the case as excitons do interact with each other due to Coulomb dipole repulsion. As such, the Hamiltonian for the system, as given in [34], in the rotating frame described after the unitary transformation  $R(t) = e^{i\omega_L t(\hat{a}^\dagger \hat{a} + \hat{b}^\dagger \hat{b})}$  is given by [34],

$$\begin{aligned} \hat{H}_{eff} = \hbar \left[ \omega_X \hat{b}^\dagger \hat{b} + \omega_C \hat{a}^\dagger \hat{a} + \Omega_R \hat{b} \hat{a}^\dagger + \frac{\omega_{nl}}{2} \hat{b}^\dagger \hat{b}^\dagger \hat{b} \hat{b} - \alpha_{sat} \Omega_R \hat{b}^\dagger \hat{b}^\dagger \hat{a} \hat{b} \right. \\ \left. - \alpha_{sat} \Omega \hat{a}^\dagger \hat{b}^\dagger \hat{b} \hat{b} + \mathcal{F}_0(t) e^{-i\omega_p t} \hat{a}^\dagger + \mathcal{F}_0^*(t) e^{-i\omega_p t} \hat{a} \right] \end{aligned} \quad (3.15)$$

where  $\hat{a}$  and  $\hat{b}$  are the creation and annihilation operators of the ‘photonic dot’ and the excitons respectively. This Hamiltonian is a standard, but extensive derivation with the first and second term defining the exciton and cavity mode energies respectively. The next term along with the fifth and sixth term describe the interaction between the exciton reservoir and cavity mode, with  $\Omega_R$  is the vacuum Rabi frequency and  $\alpha_{sat}$  is the saturation co-efficient. The final two terms are the projection of the pump laser on the cavity mode  $\mathcal{F}_0(t)$  and its complex conjugate, given by,

$$\mathcal{F}_0(t) = \int d\mathbf{x} F_p(\mathbf{x}, t) \phi_C^*(\mathbf{x}), \quad (3.16)$$

where  $F_p(\mathbf{x}, t)$  describes the applied pump field with frequency  $\omega_p$  and  $\phi_C^*(\mathbf{x})$  is the complex conjugate of the ‘photonic dot’ (polariton mode) spatial wavefunction. The fourth term of this Hamiltonian holds the greatest interest as this term describes the exciton-exciton interaction and is given by [34],

$$\frac{\hbar\omega_{nl}}{2} \hat{b}^\dagger \hat{b}^\dagger \hat{b} \hat{b}, \quad (3.17)$$

where  $\hbar\omega_{nl}$  is the interaction energy between two excitons and  $\omega_{nl}$  is the effective non-linear co-efficient defined by the integral,

$$\omega_{nl} = \kappa^{int} \int d\mathbf{x} |\phi_C(\mathbf{x})|^4 \quad (3.18)$$

where  $\kappa^{int}$  is the interaction constant and  $\phi_C(\mathbf{x})$  is the exciton spatial wavefunction. Since exciton generation occurs only within the region of the interaction between the quantum emitter and the cavity mode, the exciton and cavity mode have the same spatial wavefunction. With the non-linear co-efficient defined as above and possessing the same spatial wavefunction as the cavity mode, the dependence on photonic confinement can be clearly shown by integrating over different geometries such as a micropillar, for example, which is cylindrical,

$$\int_{cylinder} d\mathbf{x} |\phi_C(\mathbf{x})|^4 = 2.67/(2R)^2, \quad (3.19)$$

where  $R$  is the radius of the micropillar. This clearly shows an inverse proportionality of  $\omega_{nl}$  to the lateral area of the cavity mode. This inverse proportionality becomes significant when describing the second order coherence function for the system. The signature of such a system in the polariton blockade is distinctive anti-bunching  $g_{phot}^2(0) < 1$ . The second order auto-correlation function depends critically on the ratio of the non-linear co-efficient to the polariton linewidth  $\frac{\omega_{nl}}{\gamma}$  shown in Fig[3.6].

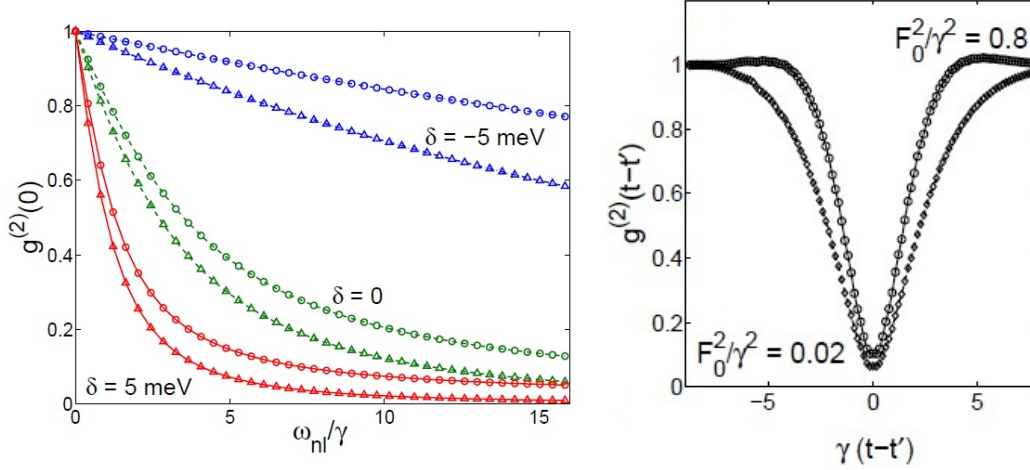


FIGURE 3.6: The left figure shows second order auto-correlation function for photons (circles) and excitons (triangles) as a function of normalised non-linear co-efficient  $\omega_{nl}/\gamma$  for three different detunings,  $\delta = 5 \text{ meV}$ ,  $\delta = -5 \text{ meV}$  and  $\delta = 0$  where  $\delta = \hbar(\omega_C - \omega_X)$ .  $\hbar\gamma_C = \hbar\gamma_X = 0.1 \text{ meV}$  and  $\omega_{pump} = \omega_{LP}$ . Experimentally, only the photon components can be probed. the right figure shows the second order auto-correlation function at fixed  $t'$  as a function of time for two different pump powers.  $\hbar(\omega_C - \omega_X) = 5 \text{ meV}$ ,  $\hbar\omega_{nl} = 1 \text{ meV}$  and  $\hbar\gamma_C = \hbar\gamma_X = 0.1 \text{ meV}$  where  $\gamma_C$  and  $\gamma_X$  are the homogeneous broadening of the exciton and cavity modes respectively. Both figures taken from [34].

The three curves on the left-hand figure in Fig[3.6] demonstrate the effect of the excitonic fraction of the polariton mode on the overall blockade effect, since the interaction strength is dependent on this excitonic fraction. For positive detunings,  $\delta > 0$ , the polariton mode has a higher excitonic fraction which promotes increased polariton-polariton interactions. For values of  $\frac{\omega_{nl}}{\gamma} \sim 1$ , anti-bunching behaviour starts to become significant. At values  $\frac{\omega_{nl}}{\gamma} \gg 1$ , the system enters the strong polariton blockade regime. Thus, only one polariton is present in the system with the probability of having two polaritons at the same time rapidly vanishing due to the interaction-induced blue shift of polariton resonance energy shown in Fig[3.7].

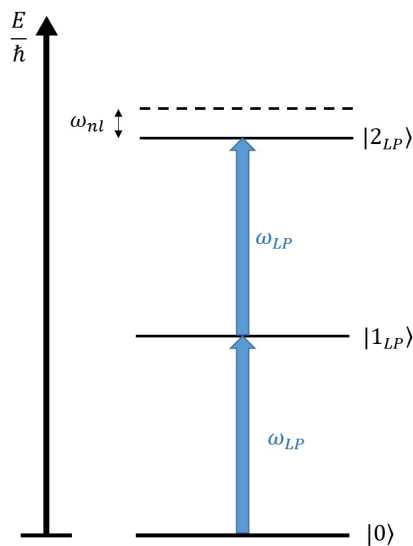


FIGURE 3.7: The symmetry of the polariton energy structure is broken with a blue shift of the higher polariton energy states induced by strong polariton-polariton interactions.

With the critical dependence on  $\frac{\omega_{nl}}{\gamma}$  which itself is inversely proportional to the lateral extent of the cavity mode, a means must be introduced that reduces the cavity lateral size ( $\omega_0$ ) to produce an increased photonic confinement of the exciton wavefunction.

### 3.2.2 Polariton Confinement

In their paper, Verger *et.al.* suggest that strong polariton-polariton interactions can be achieved through polariton confinement through its photonic component to reach the polariton blockade regime. As such, several techniques have been in development to realise this regime. One such technique is the micropillar microcavity [69]. The micropillar is a micrometer sized pillar etched from a 2D microcavity using electron beam lithography. The small lateral extent of the micropillar ( $\sim 2\text{-}4\mu\text{m}$ ) provides the lateral confinement. In such systems, strong polariton-polariton interactions have been shown through polariton condensation [70] which demonstrate characteristic blue shift in the condensate emissions.

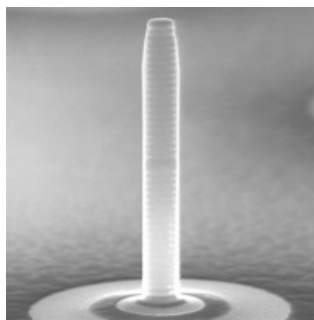


FIGURE 3.8: A SEM image of a high finesse micropillar cavity. The large gap in the middle of the pillar is the quantum well. Diameter of the pillar is  $\sim 0.8\mu\text{m}$ . Take from [71].

Other techniques shown include the use of mesa structures which locally lowers the cavity mode energy through differently spaced DBR layers [42]. However, there is considerable photon losses due to the high intensity emissions from the cavity. This restricts the ability to enter the non-linear regime even though confinement is small  $\sim 3\mu\text{m}$ . This limitation is also compounded by limited tunability which inhibits the ability to probe over a range of polariton energies. As such, these systems, while able to offer photonic confinement, incur significant losses through their sides, such that they are unsuitable to reach the strong, non-linear regime.

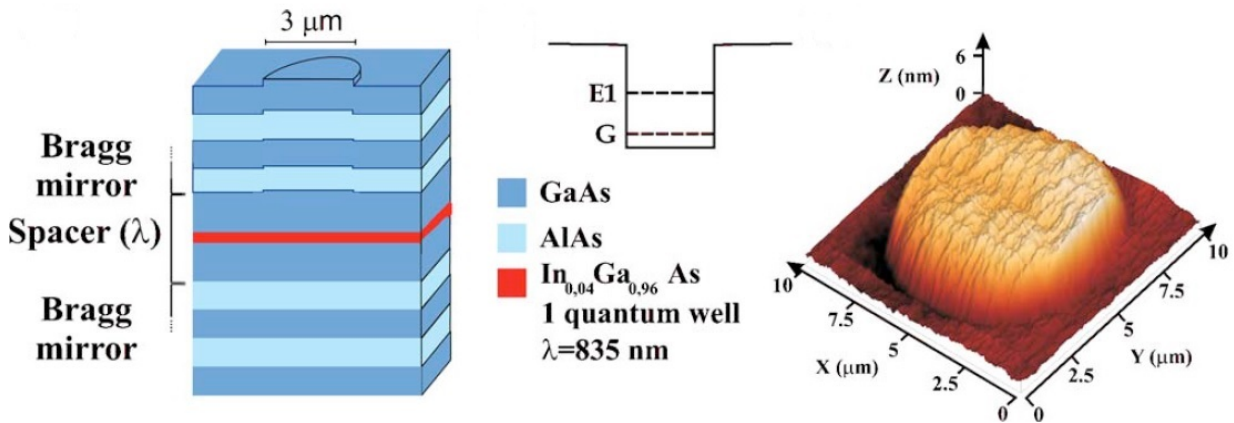


FIGURE 3.9: Circular mesa microcavity structures. The DBR layers are displaced, slightly lengthening the cavity, spatially and spectrally separating the mesa structure from the rest of the cavity. The middle picture shows the energy level diagram for the mesa with an AFM image of the circular mesa structure. Taken from [42].

### 3.3 Fabry-Pérot Fibre Microcavities

Recently, a new type of microcavity has been shown to generate polaritons, without the restrictions of the fully integrated, semi-conductor microcavity; the semi-integrated, Fabry-Pérot fibre Microcavity [47].

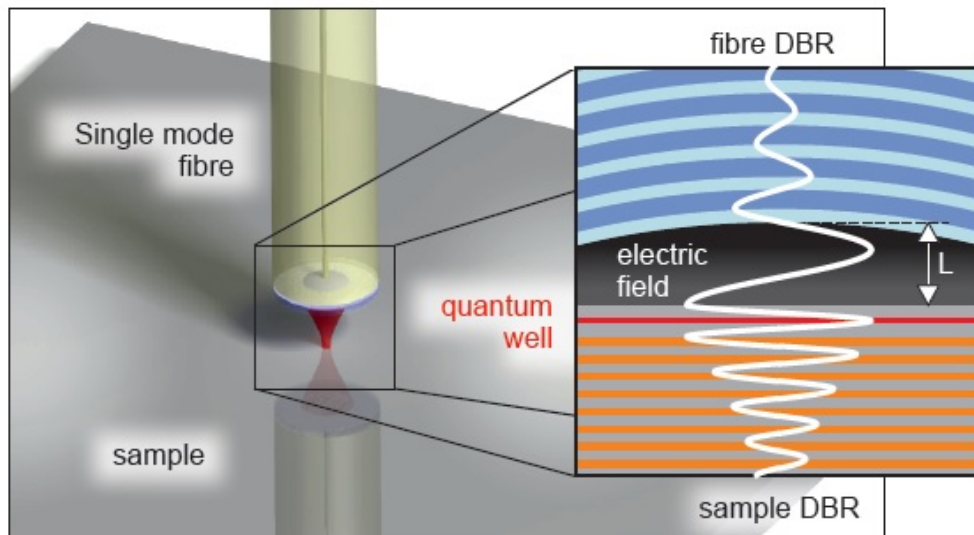


FIGURE 3.10: Semi-integrated fibre microcavity showing the concave fibre mirror with DBR layers. The insert shows the electric field distribution inside the cavity with the Quantum Well placed at an anti-node of the field. Taken from [47].

These fibre microcavities are composed of two separate parts. One half is composed of the familiar emitter with only one side deposited with a semiconductor DBR. The other half of the device is comprised of a cleaved optical fibre, whose end facet has a small concave impression manufactured upon it, with a dielectric DBR deposited over this impression. This forms the other mirror of the cavity which is shown in Fig[3.10]. With the fibre separate from the QW substrate, it is possible to change the cavity length, hence change the frequency of the cavity field and the polariton lifetime. With these improvements and others such as enhanced Q-factors and reduced mode volume due to the ability to machine small Radius of Curvature (ROC) onto the fibres, the Fabry-Pérot Fibre microcavity has been shown [47] as a clear alternative for realising the polariton blockade regime.

#### 3.3.1 Gaussian Optics and $TEM_{00}$ Fundamental Mode

Gaussian optics are used extensively to illustrate the workings of electromagnetic fields as they propagate inside optical resonators. Using the Helmholtz equation under the paraxial wave approximation, the scalar electric field wave equation propagating in free space is given by [72],

$$\left( \frac{\partial^2}{\partial x^2} + \frac{\partial^2}{\partial y^2} - 2ik \frac{\partial}{\partial z} \right) E(x, y, z) = 0 \quad (3.20)$$

where  $k = 2\pi/\lambda$  is the wavenumber and  $E(x, y, z)$  is the complex wave amplitude. The fundamental mode  $TEM_{00}$  solution to this equation is given by [72],

$$E(r, z) = E_0 \frac{W_0}{W(z)} \exp\left(-\frac{r^2}{W^2(z)}\right) \exp\left(-i\left(k\frac{r^2}{2R^2(z)} + q(z)\right)\right), \quad (3.21)$$

where  $r^2 = x^2 + y^2$ ,  $W(z)$  is the spot size,  $R(z)$  is the radius of curvature of the phase front and  $q(z)$  is the *Gouy* phase,

$$\begin{aligned} W_0 & \quad \text{beam waist,} \\ z_0 & = \frac{\pi W_0^2}{\lambda} \quad \text{Rayleigh range,} \\ W(z) & = W_0 \sqrt{1 + \left(\frac{z}{z_0}\right)^2}, \\ R(z) & = z \left[1 + \left(\frac{z_0}{z}\right)^2\right], \\ q(z) & = \tan^{-1}\left(\frac{z}{z_0}\right). \end{aligned}$$

The radial distribution for the intensity is given by,

$$I(r) = I_0 \exp\left(-\frac{2r^2}{W^2(z)}\right). \quad (3.22)$$

### 3.3.2 The Optical Resonator

An optical resonator is, in its most basic form, two highly reflective mirrors which bounce light between them known as a Fabry-Pérot cavity. To produce a stable cavity mode the phase front curvature of the intracavity field must match to the mirror curvature. In this respect, the mode waist of the cavity field  $W_0$  is related to the length  $L$  between the mirrors as [72],

$$W_0^2 = \frac{L\lambda}{\pi} \sqrt{\frac{g_1 g_2 (1 - g_1 g_2)}{(g_1 + g_2 - 2g_1 g_2)^2}}, \quad (3.23)$$

with,

$$g_{1,2} = 1 - \frac{L}{R_{1,2}}, \quad (3.24)$$

where  $R_{1,2}$  refer to the radius of curvature of each mirror and  $\lambda$  is the wavelength and where the stability range must fall within,

$$0 \leq g_1 g_2 \leq 1. \quad (3.25)$$

The next consideration, which is of particular importance in cavity-QED, is the mode volume of the cavity mode. For a typical gaussian standing wave in the cavity the mode function is given by,

$$\psi(r, z) \propto \sin(kz) \exp\left(-\frac{r^2}{W_0^2}\right). \quad (3.26)$$

By integrating over both  $r$  and  $z$ , this will give us the volume under the curve, hence the mode volume  $V$ ,

$$V = 2\pi \int_0^\infty \int_{-L/2}^{L/2} r |\psi(r, z)|^2 dr dz, \quad (3.27)$$

$$= \frac{\pi W_0^2 L}{4}. \quad (3.28)$$

Finally, considerations need to be addressed regarding the spectral qualities of the cavity. The transmission function from the cavity has distinct spectral peaks at resonance. Between successive TEM<sub>00</sub> peaks, this spacing is known as the *Free Spectral Range* or *FSR* and relates to the separation between the cavity mirrors as defined by [72],

$$\Delta v_{FSR} = \frac{c}{2L}. \quad (3.29)$$

Another important quality of the resonator also is the FWHM or more commonly known as the *linewidth* of the peak transmission is given by [72],

$$\delta v = \frac{1-R}{\sqrt{\pi R}} \Delta v, \quad (3.30)$$

where  $R$  is the reflectivity of the mirrors used. Here it is assumed that both mirrors have the same reflectivity. This leads to the quantity known as the *Finesse*  $F$  which demonstrates the spectral resolution of the cavity defined by the ratio between the FSR and the linewidth,

$$F = \frac{\Delta v_{FSR}}{\delta v} = \frac{\pi\sqrt{R}}{1-R} \simeq \frac{\pi}{1-R} = \frac{\pi}{T+L}, \quad (3.31)$$

where  $L$  is the round trip losses and  $T$  is the transmittivity and  $T + L + R = 1$ . A more appropriate way to look at the *Finesse* can be expressed in the form of the number of round trips  $N$  a photon takes through the cavity before it is lost out of the cavity mode,

$$F = \pi N. \quad (3.32)$$

A final quantity extensively used describe to the quality of a particular cavity is the *Q-factor* (Quality factor). This is defined by the resonant frequency divided by the *linewidth* [72],

$$Q = \frac{v}{\delta v} = \frac{2Lv}{c} F, \quad (3.33)$$

where  $L$  is the cavity length. Q-factor can also be explained as the ratio of round trip loss of the cavity with respect to the total energy inside the cavity. For cavity-QED, it is a necessity to attain high Q-factors on the order of  $\sim 10^5$ .

### 3.3.3 Fibre Microcavities

Fibre microcavities are hemispherical type resonators as shown in Fig[3.11].

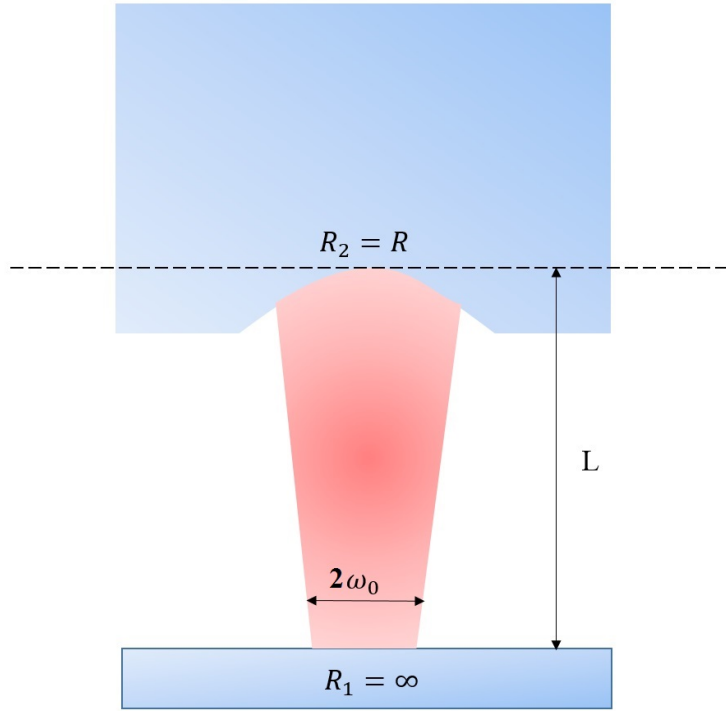


FIGURE 3.11: The hemispherical resonator. The fibre has a radius of curvature  $R$  while the quantum well is a planar structure with  $\text{ROC} = \infty$ .  $L$  is the cavity length and  $\omega_0$  is the mode field diameter.

By substituting  $g_1 = 1$  and  $g_2 = 1 - \frac{L}{R_2}$  into eq. 3.23, the mode field diameter simplifies to,

$$W_o^2 = \frac{\lambda}{\pi} \sqrt{L(R_2 - L)}, \quad (3.34)$$

where  $\lambda$  is the wavelength,  $L$  is the length of the cavity and  $R_2$  is the ROC of the curved mirror. With the ability to tune the cavity length with these microcavities, the mode field diameter then as a function of the cavity length for a given ROC is shown in Fig[3.12].

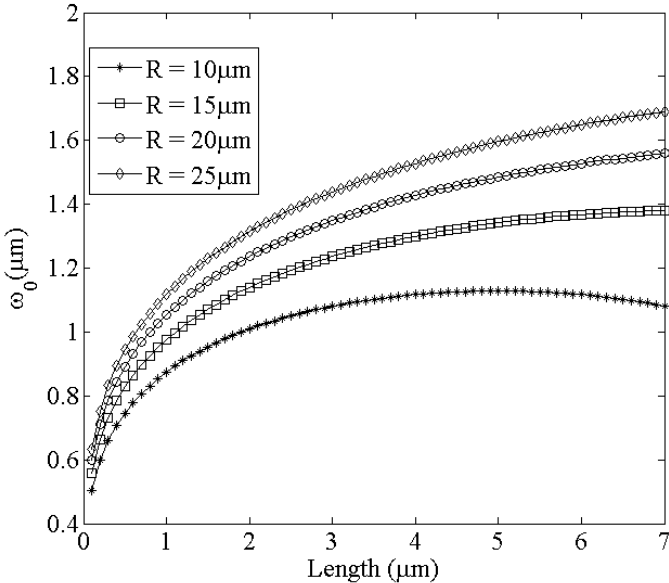


FIGURE 3.12: The mode field diameter of a cavity as a function of cavity length for several values of radius of curvature ( $R$ ).

# Chapter 4

## Fabry-Pérot Fibre Microcavity Fabrication

This chapter explains the experimental setup for machining fibre microcavities to reach the polariton blockade regime. As an introduction, we give a brief description of the CO<sub>2</sub> laser ablation process. Secondly, a summary of the CO<sub>2</sub> laser setup is given to explain key parameter control for desired indentation machining (section 4.2). Thirdly, an outline of the experimental setup with emphasis placed upon the imaging system capabilities (section 4.1). Fourthly, indentation analysis is explained using optical profilometry (section 4.3). Finally, Distributed Bragg Reflectors are discussed and their function explained using the Transfer Matrix Method (section 4.4).

To reach the polariton blockade regime stated in the previous chapter, a Fabry-Pérot Fibre microcavity approach is chosen due to its controllability and excellent optical qualities. However, to achieve the necessary polariton confinement through its photonic component, the fibre components of the microcavity must be machined to produce a reduced mode volume while maintaining high Q-factors. To this end, concave indentations with small ROC and low surface roughness are required to be machined onto cleaved fibre facets which can then be coated with a dielectric DBR. In our experimental setup, we develop a system to manufacture a large number of fibres with ROCs as small as 10 $\mu$ m using a 10.6 $\mu$ m, CO<sub>2</sub> based laser ablation system equipped with a laser interferometry characterisation capability in real time.

CO<sub>2</sub> laser systems are the ideal tool for fused silica machining. These types of laser systems produce a wavelength in the 10 $\mu$ m region which is readily absorbed within the first few  $\mu$ m of the fibre due to side band absorption from the asymmetrical stretching of the Si-O-Si mode at 9.3 $\mu$ m. This means that the laser radiation is absorbed in a localised area well suited to the small structures intended for our fibre machining. To better understand the energy process occurring when the laser radiation impinges on the fibre, the heat conduction equation describes the evolution of temperature  $T(\mathbf{r}, t)$  at time  $t$  and position  $\mathbf{r}$  [72],

$$\rho C \frac{\partial T(\mathbf{r}, t)}{\partial t} - \nabla(\kappa \nabla T(\mathbf{r}, t)) = Q(\mathbf{r}, t), \quad (4.1)$$

where  $\rho$  is the density of the fused silica,  $C$  is the specific heat capacity,  $\kappa$  is the thermal conductivity,  $T(\mathbf{r}, t)$  is the fibre surface temperature profile and  $Q(\mathbf{r}, t)$  is the heat source. In the case of the CO<sub>2</sub> laser radiation,  $Q(\mathbf{r}, t)$  has a Gaussian shape given by the gaussian profile of the CO<sub>2</sub> beam [72],

$$Q(\mathbf{r}, t) \propto \frac{P}{\pi\omega_0^2} \exp\left[-\frac{2(x^2 + y^2)}{\omega_0^2}\right], \quad (4.2)$$

where  $P$  is the power of the beam and  $\omega_0$  is the waist. The solution to the surface temperature profile is evaluated using cylindrical co-ordinates  $(\rho, \varphi, z)$  due to the shape of the fibre using the appropriate Green function [72]

$$T(\rho, z = 0, \tau) = \frac{P(1 - R)}{\pi^{3/2}} \frac{\sqrt{D}}{\kappa} \int_0^\tau \frac{\exp\left[-\frac{\rho^2}{4Dt + \omega_0^2/\sqrt{2}}\right]}{t^{1/2}(4Dt + \omega_0^2/\sqrt{2})} dt, \quad (4.3)$$

where  $\tau$  is the pulselength,  $D$  is the diffusion constant  $D = \kappa/\rho C$ . The temperature at the centre of the beam is given by [72],

$$T(\rho = 0, z = 0, \tau) = \frac{(1 - R)P}{\sqrt{2\pi^3}\omega_0\kappa} \arctan\sqrt{\frac{t}{\tau_0}}, \quad (4.4)$$

where  $\tau_0$  is the diffusion time  $\tau_0 = \omega_0^2/2D$ . The material from the fibre will thus be removed predominately from the centre of the incident laser beam. Using a parabolic approximation for the central temperature  $T(\rho, \tau) \simeq T(0, \tau)(1 - \rho^2/\omega_0^2)$ , the expected ablation structures will have a near gaussian shape [72]. These near gaussian ablation structures are then approximated to be spherical near the centre of the structure as the ROC variation is small in this area (see section 4.3). To achieve these ablation structures with high quality and previously mentioned specifications, laser parameters such as beam waist, power and pulse duration  $\tau$ , must be carefully chosen and very well controlled. This will allow the ablation process to be in the regime of evaporation with a smoothing effect due to surface tension, reducing surface roughness. The created geometries are exponentially dependent upon the control parameters,  $P$ ,  $\omega_0$  and  $\tau$ . For a more complete analysis of the complex processes that occur for CO<sub>2</sub> laser ablation of silica surfaces, refer to [72].

## 4.1 Fibre Imaging and Machining System - FIMS

Our experimental setup for the FIMS incorporates a CO<sub>2</sub> laser ablation system for fibre machining and a laser interferometry imaging system for real-time fibre indentation analysis. The experimental setup was constructed as shown in Fig[4.1].

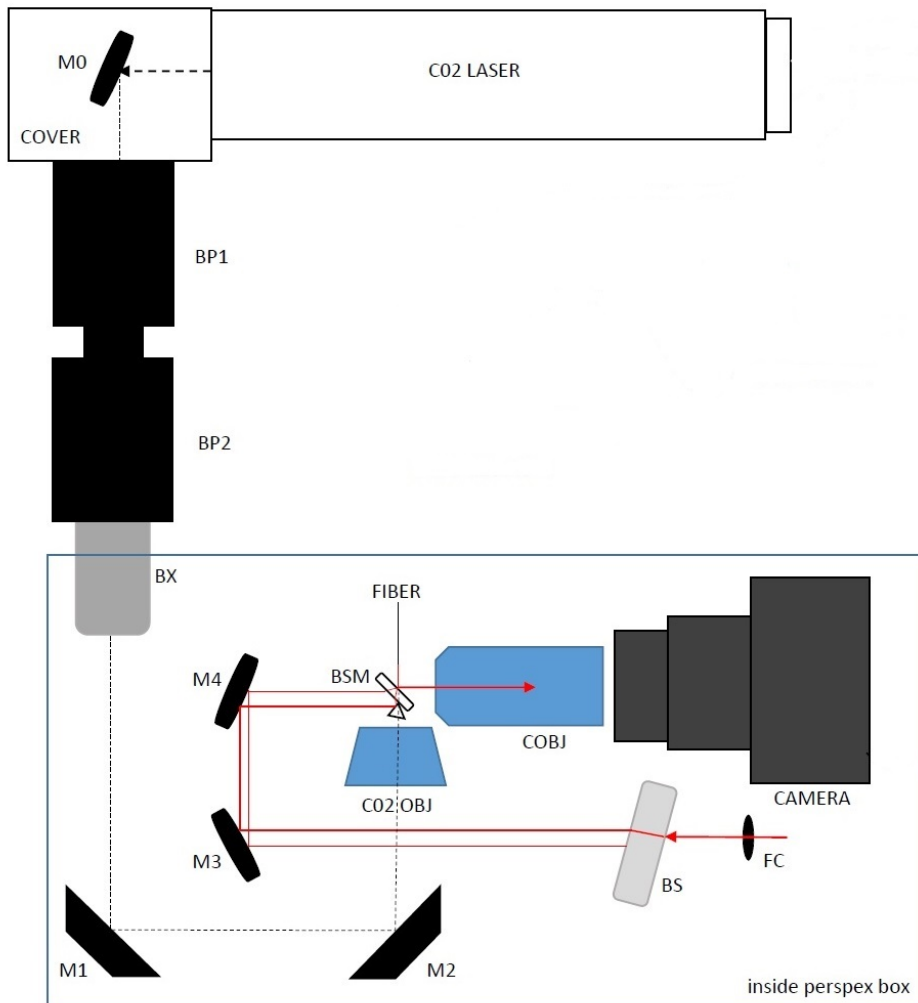


FIGURE 4.1: FIMS experimental setup. This system comprises of two subsystems, the CO<sub>2</sub> laser ablation system and laser interferometry imaging system. The CO<sub>2</sub> laser ablation system starts in the top right corner with the water-cooled Synrad Firestar v30 CO<sub>2</sub> laser. Following the path of the beam left out of the laser is M0 which is a silicon coated mirror to guide the beam into the Brewster attenuators. The beam passes through BP1 and BP2 which are the Brewster attenuators which control beam power and polarisation. The beam exits BP2 into the beam expander BX which alters the size and position of the beam waist. The beam then reflects from M1 which is a silicon coated mirror onto M2 which is a  $\lambda/4$  reflecting phase retarder for conversion of linearly polarised light into circularly polarised light. The CO<sub>2</sub> beam then passes through CO<sub>2</sub> OBJ which is the aberration free focussing double lens for beam focussing onto the fibre, with a working distance of 20.5mm. The laser interferometry imaging system starts in the lower right corner with a HeNe laser (632.8nm) coupled into the system with the fibre coupler, FC, which incorporates a focal screw and polariser for maximum interference contrast. The beam then impinges on the large fused silica beamsplitter, BS, used to create the two arms of the interferometer. The split beams are reflected off the silver mirrors M3 then M4. The beams travel towards the beamsplitter/mirror combination, BSM (see section 4.2.1). The beams are collected by COBJ which is a Mitotuyo microscope objective with a 50x magnification. Finally, the camera is a DSLR Canon CCD camera for image capture of the fibre facet.

The most notable and novel aspect of this design, utilises an unusual beam splitter and mirror combination (BS/M) to perform interferometry on the cleaved fibre facet for indentation analysis. This unique combination serves twofold. It reduces the size of the interferometer as to fit in the available working space as well as to characterise the indentations *in situ* without the need to remove the fibre.

## 4.2 CO<sub>2</sub> Laser Ablation System

This experimental setup employed the use of a pulsed  $10.6\mu\text{m}$  CO<sub>2</sub> laser system for the indentation machining on the fibre end facet. The model of laser used was the Synrad Firestar v30, water-cooled CO<sub>2</sub> laser producing 30W, horizontally polarised,  $10.6\mu\text{m}$  laser radiation. To produce fibres with low surface roughness, small ROC and non-elliptical indentations, key parameters such as laser power, pulse duration, beam waist and polarisation must be controlled. Power is of critical importance to this type of procedure. As such, a careful choice of laser power is required to create indentation with different characteristics.

In this experimental setup, laser power was controlled by beam attenuation. Attenuation of the beam was accomplished by the use of two coupled, water-cooled, ZnSe coated, Brewster window attenuators supplied by ULO optics. These brewster attenuator work using the brewster angle principle whereby transmission of the beam is dependent upon the incident polarisation compared to the ZnSe coated window titled at the brewster angle. By coupling two attenuators together, the first attenuator acts as the main power attenuation for the beam while the second attenuator, while still attenuating the beam to a lesser extent, sets the polarisation angle of the beam. This polarisation becomes important for conversion into circularly polarised light.

In the past, when machining with CO<sub>2</sub> laser based systems, it was found that material being machined responded differently to the polarisation of the laser radiation. Figure 4.2 shows a cut made with linearly polarised light as well as by circularly polarised light.

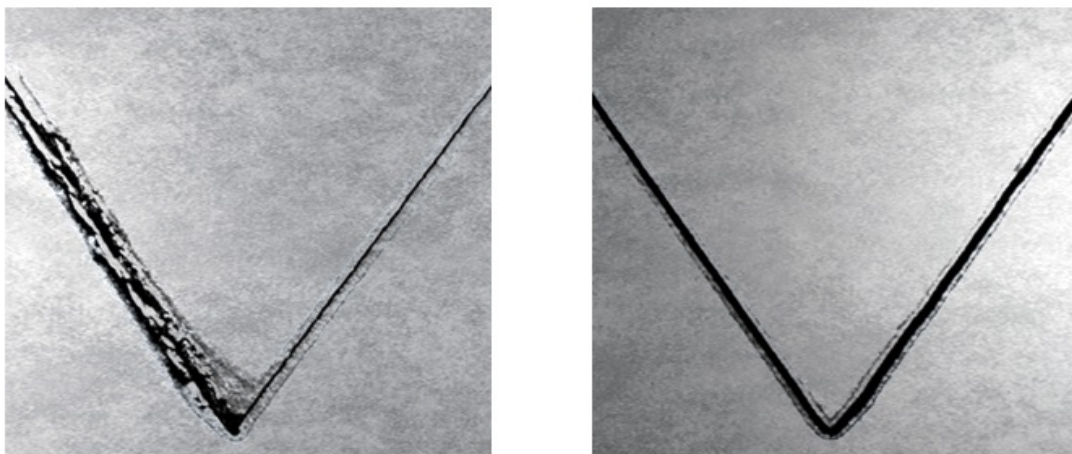


FIGURE 4.2: Two cuts produced by a CO<sub>2</sub> laser system, The left figure shows a cut made by linearly polarised light while the right shows a cut made by circularly polarised light. Taken from [73].

This clearly shows that circularly polarised light produces better results. This result occurs for linearly polarised light due to the increasing angle of incidence of the beam as the cut is made. This means that one polarisation axis is reflected more than the other, depending on the direction of the cut. This leads to a reduced cut quality due to differing energy deposition into the material [73]. Circularly polarised light ensures that equal amounts of both polarisation axes are experienced, regardless of orientation, ensuring uniformity. For this reason, a  $\lambda/4$  reflecting phase retarder is included in the experimental setup. However, for effect use of the phase retarder, the incident beam path must be  $45^\circ$  to the phase retarder as well as the incident polarisation must be  $45^\circ$  to the phase retarder's axis of rotation from the normal. This design principle is shown in Fig[4.3].

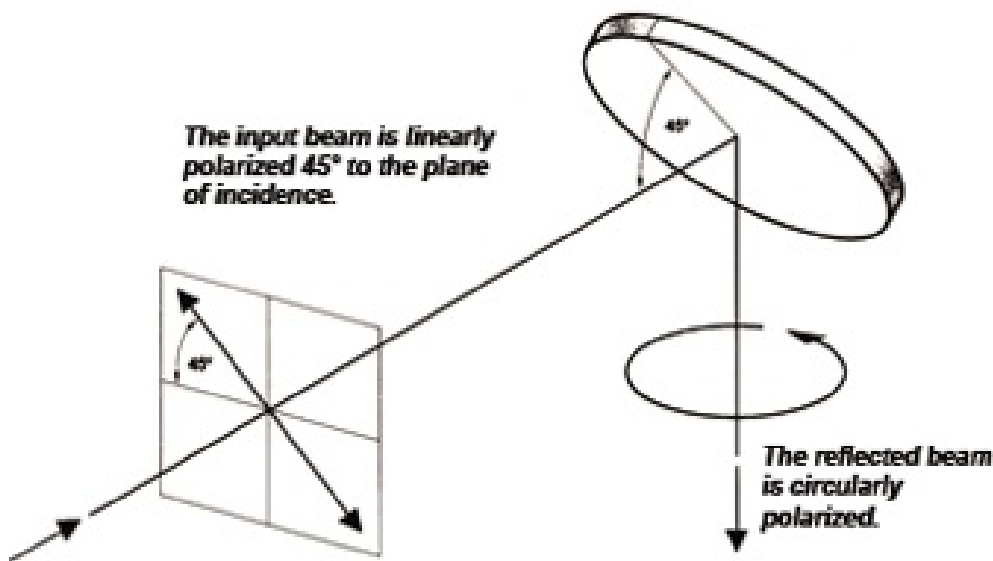


FIGURE 4.3: Silicon  $\lambda/4$  Phase Retarder function. The incoming light must have a 45 degree incident angle with linear polarisation orientated  $45^\circ$  to the axis of rotation of the phase retarder from the normal. Taken from [73].

The use of circularly polarised light also eliminates non-paraxial focussing issues [74]. By utilising circularly polarised light, the polarisation vector is rotating so no preference is given to any one polarisation vector. This ensures that the indentations are nearly circular which is essential for effective microcavities. To produce small ROC indentations, focussing of the laser beam is required. The  $\text{CO}_2$  laser produces a beam waist on the order of  $\sim 2.5\text{mm}$ , thus the beam requires a focussing mechanism to reduce the beam waist to near the wavelength of the light used. As such, a beam expander and an aberration corrected, aspheric double focussing lens assembly are incorporated. The beam expander, as the name suggests, expands the beam before focussing through the double lens. This allows the lenses to reduce the beam waist due to the larger incident beam size. With an aberration free lens assembly and a working distance of 24mm, this ensures most optical aberrations are removed so that the indentations are not distorted. To finally machine the indentations on the fibre facets, short pulses of laser radiation is used to control the amount of radiation released as to not damage the fibre. The duration of these short pulses are controlled by the application of voltage

to the laser RF controller, which in turn drives the RF oscillator which directly stimulates the CO<sub>2</sub> gases. Thus, a digital signal generator is employed which sends a single square wave pulse of set duration to the RF controller. Pulse durations as small as 100 $\mu$ s could be attained. With pulse duration, power, and beam waist control, indentation characteristics such as ROC and depth can altered to meet desired applications.

A consideration of large importance when attempting to fabricate fibre cavities using this technique is ellipticity. The main reason for ellipticity in the indentations is the presence of an astigmatism in the beam profile. This results in different intensities between the two axes along the beam, such that the intensity profile is elliptic rather than circular. Therefore, the beam profile of the laser was tested and analysed for determination of the beam astigmatism. This was performed by incrementally moving a razor blade across the beam cross section and measuring the power in both the horizontal and vertical directions. The results of this profiling is shown in Fig[4.4]. It should be noted here that we used a beam expander to increase the size of the cross section.

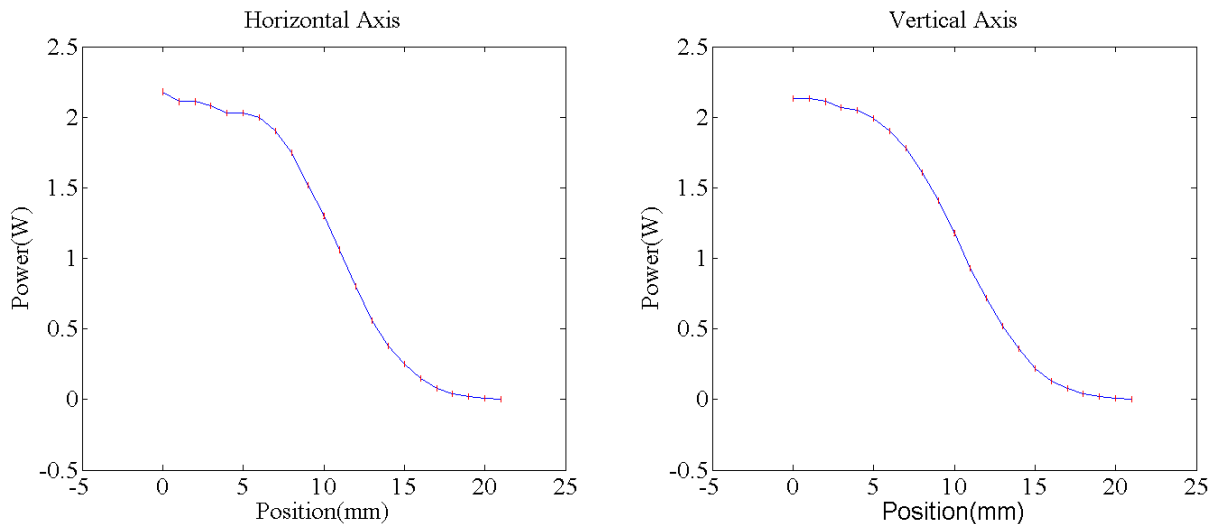


FIGURE 4.4: CO<sub>2</sub> beam profile. The error function is fitted to these profiles to extract the beam profile.

The beam waist was extracted from the beam profiles by applying the gaussian error function [75]. This gave a beam waist of 6.6mm and 7.2mm in the horizontal and vertical axes respectively. This clearly shows that an astigmatism is present and thus will affect the ellipticity of the indentations. However, this was mostly compensated for by a repositioning of the fibres along the beam path to find a position where the effects of the astigmatism are minimal. This position can be found by analysing the ellipticity of the indentations. Analysing the fibre indentation ellipticity was performed by first incrementally displacing the fibre shooting position in the direction of beam propagation i.e. moving away from the beam focus. The ellipticity of the indentations created at each incrementation can thus be calculated through the ratio of the ROC of the horizontal axis to the ROC of the vertical axis as the axes are rotated around the indentations,

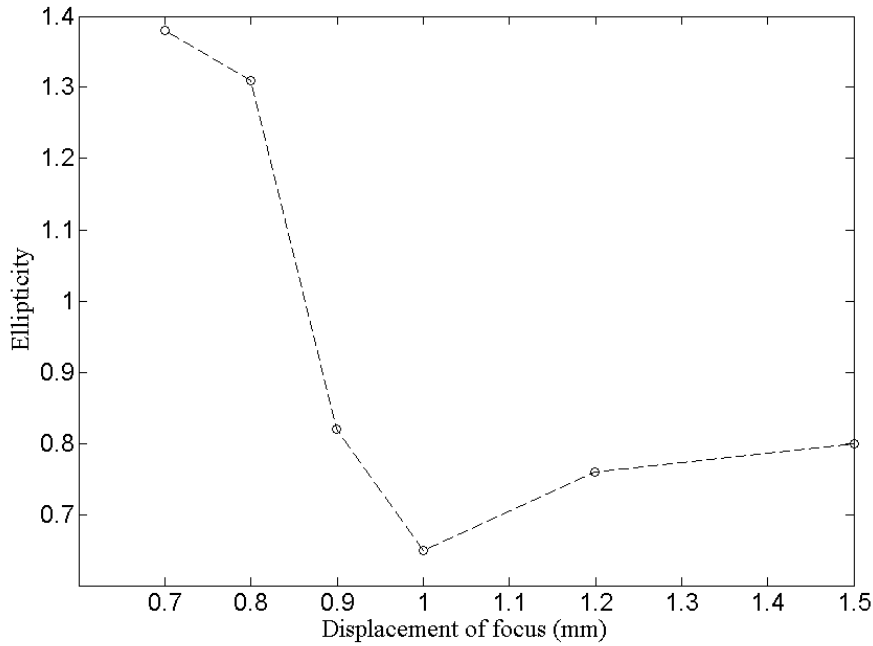


FIGURE 4.5: Ellipticity as a function of focal displacement. The ellipticity becomes worse as the value moves away from unity.

For the least ellipticity, a position with a value as close as possible to one must be used. Fig[4.5] shows that an ellipticity of 1 can be achieved at displacement of  $\sim 0.87$ mm. Thus, the fibre machining position was moved to coincide with this value. However, by shifting the fibre machining position away from the beam focus  $\omega_0$ , the beam waist will increase in size as dictated by,

$$W(z) = W_0 \sqrt{1 + \left(\frac{z}{z_0}\right)^2}.$$

This change in beam waist will affect indentation geometries for a given set of laser parameters. This deviation, however, can be mostly compensated for by altering these laser parameters.

#### 4.2.1 Laser Interferometry Imaging System

In a normal interferometer, the beamsplitter equally splits the intensity of the incident laser beam into two perpendicular arms. In Fig [4.1], the large fused silica beamsplitter after the fibre coupler, produces two horizontally separated parallel beams via internal reflection of the beamsplitter shown in Fig[4.6].

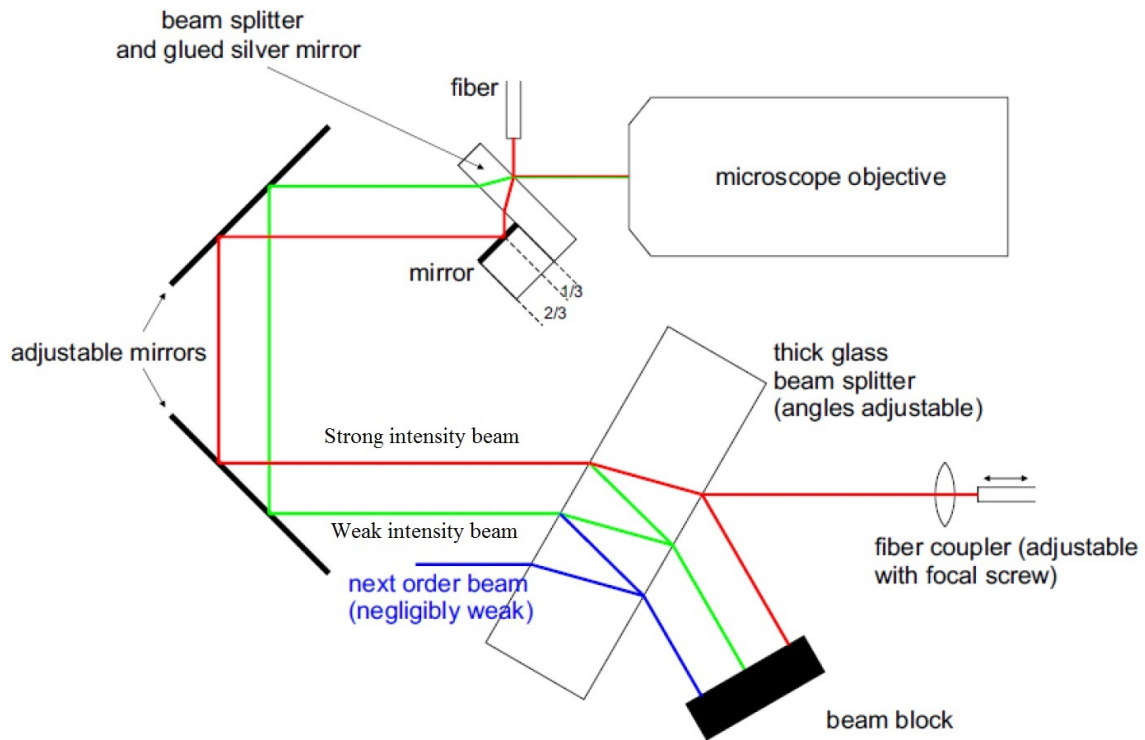


FIGURE 4.6: The laser interferometry imaging system. The large beamsplitter creates two beam paths of different intensities. The two beam paths recombine after the BS/M combination where both beams now have the same intensity.

These two beams, however, are of different intensities as the main portion of the light is transmitted at the surface ( $\sim 96\%$ ). These strong and weak intensity beams, are guided into the BS/M combination which is angled at  $45^\circ$  to the incoming beams, so that the strong intensity beam is incident on the mirror and the weak beam is incident on the fused silica beamsplitter. The beamsplitter transmits the weak intensity beam while the strong intensity beam is reflected perpendicularly into the beamsplitter and partially transmitted through to the fibre facet. The strong intensity beam is reflected from the fibre facet (measurement beam) returns to the beamsplitter where it is partially reflected and combines with the weak intensity beam (reference beam), thus producing an interference pattern image of the fibre facet, which is captured by the CCD camera. The images are later analysed in a custom Python Programme (see section 4.3). An important consideration must be made with regard to the final intensities of the two beams to achieve maximum visibility, thus, both beams must have the same intensity when they recombine. In the case for this setup, the number of reflection off both the beamsplitters and the fibre facet must be taken into account. Since both beamsplitters and fibre is composed of fused silica, the reflections off any of these surfaces can be considered to have the same loss ( $\sim 4\%$ ). In the case of the strong intensity beam, there are only two reflections along the beam path, one from the fibre facet and the other from the BS/M combination. The weak beam also undergoes two reflections along its beam path, inside the first large beamsplitter. At the other points were the two

beams interact with the beamsplitters, they are transmitted through the beamsplitters. In this case, each beam is transmitted through at three places. So with equal number of reflections of both beam paths, this gives two equal intensity beams of  $0.96^3 \times 0.04^2 \simeq 0.14\%$  of the initial laser intensity. It should be noted that clipping losses at the fibre i.e the beamspot is larger than the fibre facet area, as well as dispersion have been neglected in this calculation.

For accurate and reliable measurements with interferometry, visibility of the interference fringes is of significant importance. This requires that the measurement and reference beam intensities must be equal. The large silica beamsplitter is used to create two beam paths. However, the intensity of the beam paths are dependent of the polarisation orientation of the incident laser radiation. This is due to the reflected intensity dependence upon polarisation. This requires that the incident polarisation must be orientated such that both beams paths have equal intensity at the second beamsplitter. This was experimentally achieved through the use of a linear polariser situated just after the fibre coupler (see Fig[4.1]) as the HeNe laser used in this setup is un-polarised.

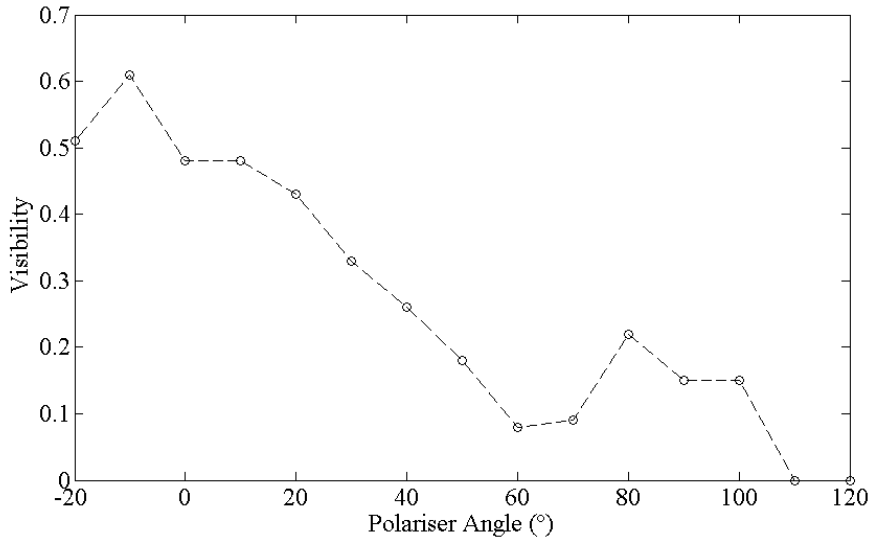


FIGURE 4.7: Visibility as a function of polariser orientation.

As shown from Fig[4.7], the best visibility of 0.61 was achieved. Fringe visibility was calculated using the following equation,

$$Visibility = \frac{I_{max} - I_{min}}{I_{max} + I_{min}},$$

where  $I_{max}$  and  $I_{min}$  are the respective maxima and minima intensity of the interference fringes. These intensity values were collected using the pixel intensity values from images of interference fringes from a cleaved fibre. To ensure the best image contrast for the most reliable interference fringe detection, several camera settings were tested to produce an image of the interference fringes with the best contrast. The camera settings, while not having a direct effect upon the actual visibility, artificially ‘improve’ the contrast between the fringes

for later analysis. Previously, the laser intensity was optimised via a linear polariser to produce a visibility of 0.61.

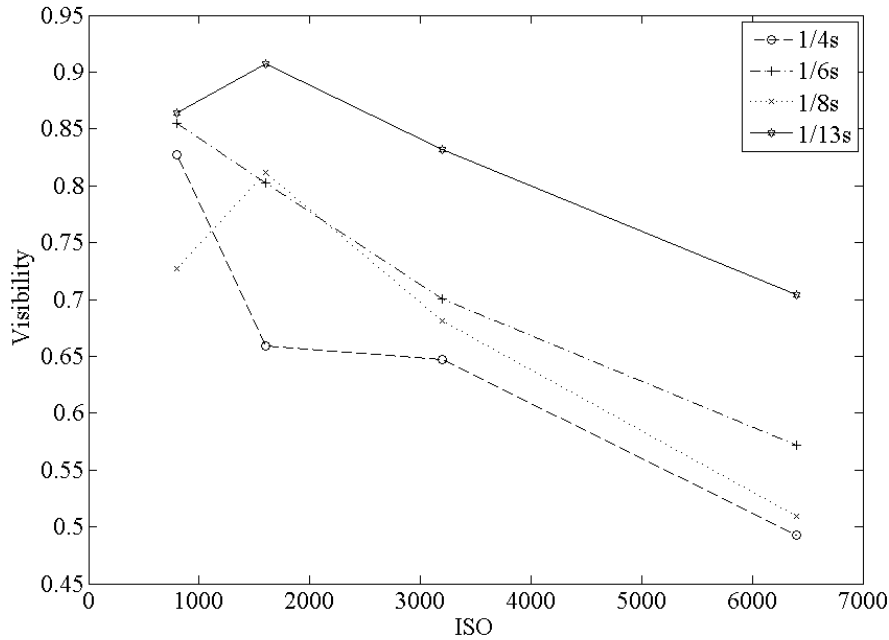


FIGURE 4.8: Interference visibility as a function of ISO (sensitivity) camera settings for four different shutter speeds. Due to shorter exposure times, brightness of the image is slightly reduced.

In Fig[4.8], the visibility clearly increases for decreasing sensitivity (ISO) and shutter speeds. This suggests that the camera CCD is saturating at high sensitivities and longer exposures. Using this data, visibility was further increased to 0.91 through changes to camera settings, with the best settings found at an ISO (sensitivity) value of 1600 and a shutter speed (exposure time) of 1/13 seconds.

For the BS/M combination to work effectively, the beamsplitter and mirror must be perpendicular to each other and to the horizontal plane, as well as,  $45^{\circ}$  to the incident laser beam. These requirements are to guarantee that the two different intensity beams overlap as they pass through to the CCD camera, ensuring maximum fringe visibility. Several design iterations culminated in a final design shown in Fig[4.9]

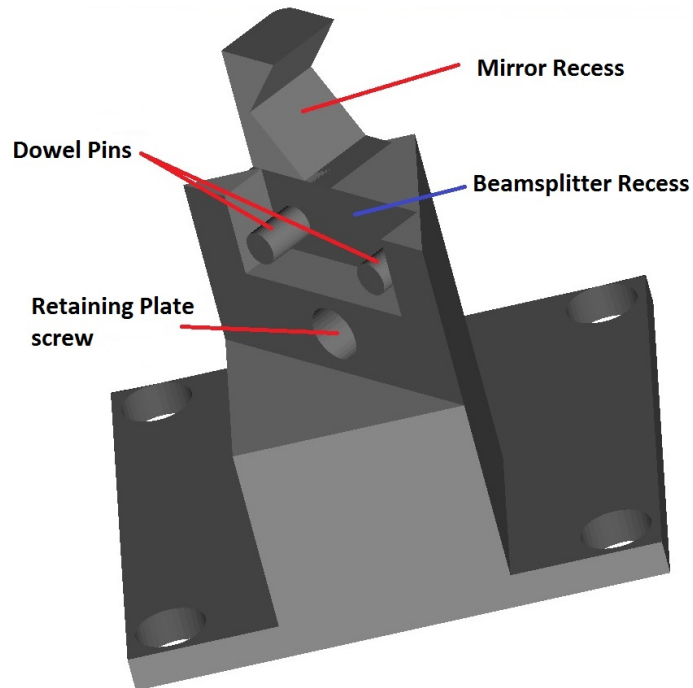


FIGURE 4.9: BS/M combination Holder. The four holes in the base are for screws to attach the holder to the attocube nanopositioner.

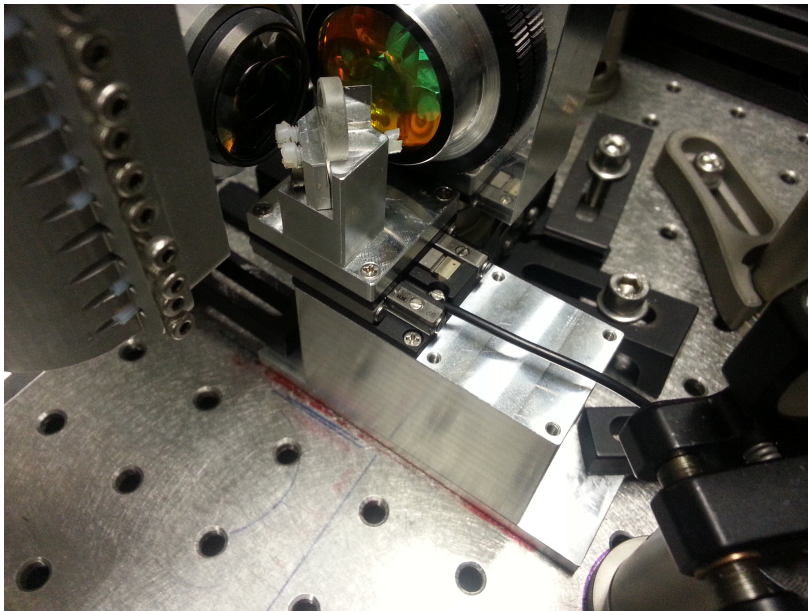


FIGURE 4.10: BS/M combination complete holder mounted on an Aluminium block. The third nylon screw can be seen on the right side of the holder.

The three-sided slot provides a housing for the beamsplitter, the fourth side remains exposed to allow easy of manufacture and for two small dowel pins to be inserted into the

pillar to provide a ‘seat’ for the beamsplitter. On the exposed side of the slot, a retaining plate is clamped down onto the beamsplitter as shown in Fig[4.9]. This retaining plate is fixed by one metal screw underneath and two nylon screws. The metal screw mostly holds the beamsplitter in place, while the two nylon screws secures the beamsplitter. These two nylon screws would also serve as a means to align the BS/M combination. A third nylon screw was inserted into the opposite side of the recess later to provide sufficient leverage for good alignment. The bottom half of the mirror recess was retained to provide the perpendicular orientation for the mirror, with the top half removed for fabrication simplicity.

To mount this holder so that the BS/M combination could be easily removed for fibre machining and replaced for imaging and alignment, a (attocube ECS3030/AL/NUM/RT closed loop) nanopositioner stage mounted on an Aluminium block was employed. With the closed loop feature of this computer-controlled positioner, the BS/M combination can be removed and returned to it’s necessary imaging position with sub-nanometre precision. This ensures reliable imaging of the fibre for analysis as well as reproducible alignment of the fibre to the CO<sub>2</sub> laser.

The images produced by our setup are shown in Fig[4.11].

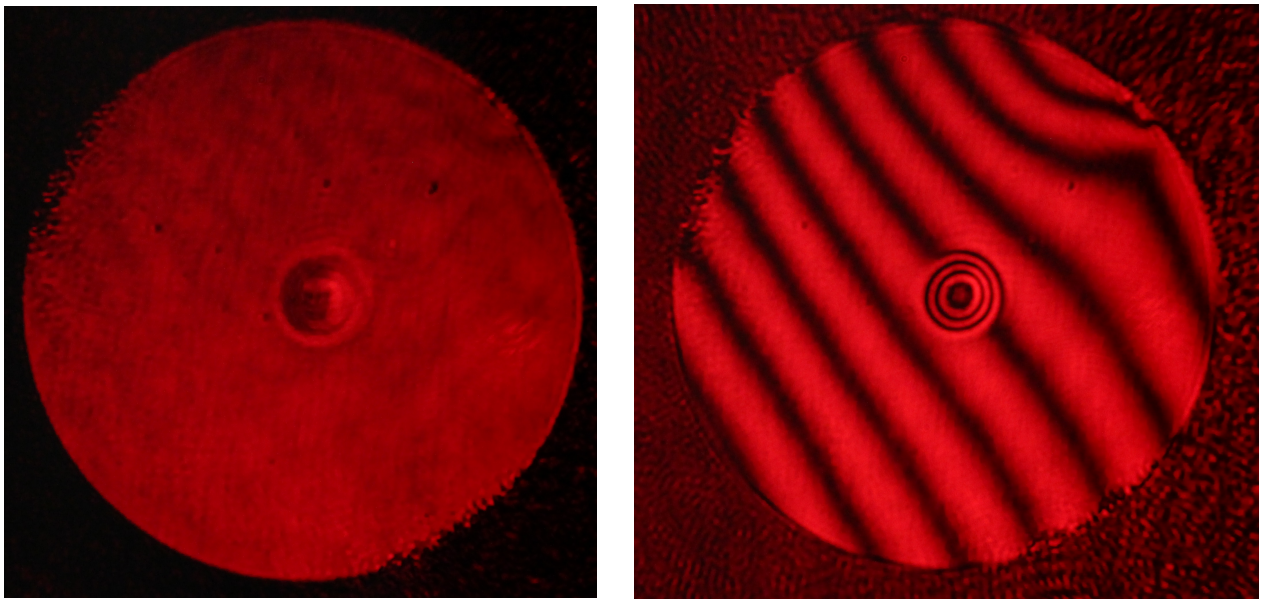


FIGURE 4.11: Images of fibres using our interferometry system. The left image shows the fibre with the weak intensity beam (reference beam) blocked. The right image shows the reference beam unblocked, with the resulting interference pattern.

### 4.3 Fibre Indentation Analysis

Fibre indentation characterisation is performed by pixel analysis of CCD images of the interference patterns in a custom Python programme. The false colour images employed by the Python programme interface shown in Fig[4.12], are a graphic representation of the topography of the fibre facet due to constructive and destructive interference of light reflected from the fibre facet.

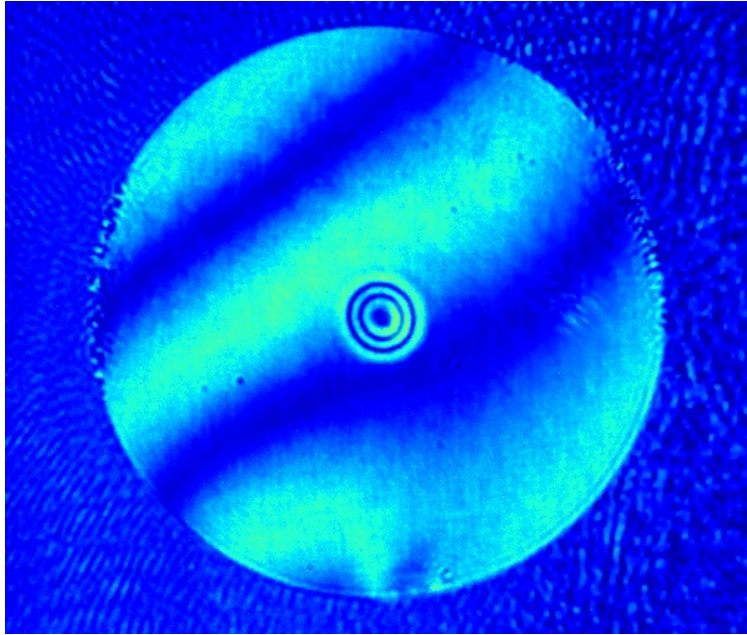


FIGURE 4.12: A false colour interference image for analysis within the Python programme interface.

Constructive interference occurs only when the difference of the phases of two overlapping EM waves are zero. Similarly, destructive interference only occurs when the phase difference is exactly  $\pi$  or  $\lambda/2$ . Because the total optical path length is twice the distance between the fibre and BS/M combination, this means for successive maximums and minimums of the interference patterns, there is a  $\lambda/4$  difference in depth. This is the principle on which this programme operates.

After fibre indentation machining, the captured CCD image is imported into the Python programme (see Fig[4.12]). As explained at the beginning of this chapter, the concave indentation will have a gaussian form. As such the profile of the indentation is not spherical and varies in ROC. However, at the centre of the profile, the ROC variation is small, and as such, can be approximated to being spherical, thus giving an ROC for this mirror [76].

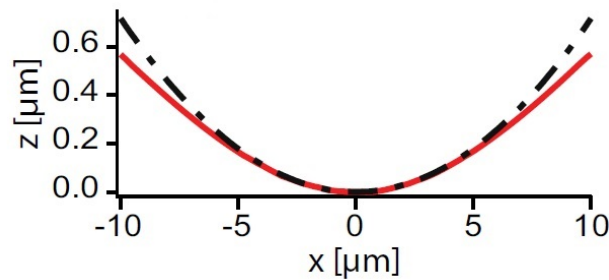


FIGURE 4.13: A zoomed graph of a Gaussian profile (red) compared to a circle at  $x=0$ . Over a small region, the ROC of the gaussian profile can be approximated by a circle. Taken from [76].

The ROC is therefore calculated by the following; first, consider the general form of a Gaussian function and the equation for a circle,

$$z(x) = -A \exp \left[ \frac{-(x-x_0)^2}{2\sigma^2} \right] \quad (\text{Gaussian}), \quad (4.5)$$

$$z(x, R) = \sqrt{R^2 - (x-x_0)^2} \quad (\text{Circle}). \quad (4.6)$$

The second derivatives with respect to  $x$  of both functions are taken and equated at  $x = 0$ . This is not done with the first derivative as this will simply yield the result that the gradient of both functions is equal to zero,

$$\frac{\partial^2 z}{\partial x^2} = \frac{A}{\sigma^2} \left( 1 - \frac{(x-x_0)^2}{\sigma^2} \right) \exp \left[ \frac{-(x-x_0)^2}{2\sigma^2} \right] \quad (\text{Gaussian}), \quad (4.7)$$

$$\frac{\partial^2 z}{\partial x^2} = \frac{R^2}{(R^2 - (x-x_0)^2)^{3/2}} \quad (\text{Circle}). \quad (4.8)$$

Equating eqs. (4.7) and (4.8) at  $x = 0$  gives,

$$R = \frac{\sigma^2}{A}, \quad (4.9)$$

where  $R$  is the ROC at the centre of the Gaussian profile and  $2\sigma$  is the diameter of the indentation and  $A$  is the depth of the structure. Analysis begins with the programme properly configured to the correct pixel size and wavelength. The pixel size is adjusted using the known diameter of the fibre ( $125\mu\text{m}$ ). The illumination wavelength is  $632.8\text{nm}$  provided by a HeNe laser. Within the interface, the white cursor is placed over the indentation and the radius adjusted so that the cursor encapsulates the indentation as seen in Fig[4.14].

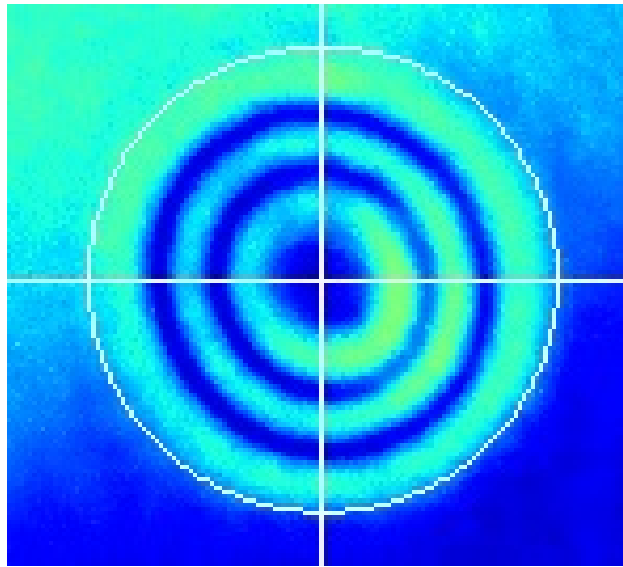


FIGURE 4.14: Fibre indentation inside white circle cursor for analysis

At this point, the programme attempts to determine the positions of relative maximum and minimum intensity which is indicated by red (maximum) and green (minimum) cross indicators shown in Fig[4.15]. The programme takes into account all the data points along the plot and attempts to extract the maximum and minimum values. However, some user input is needed to ensure that interference, rather pixel-to-pixel maximums and minimums are found for analysis.

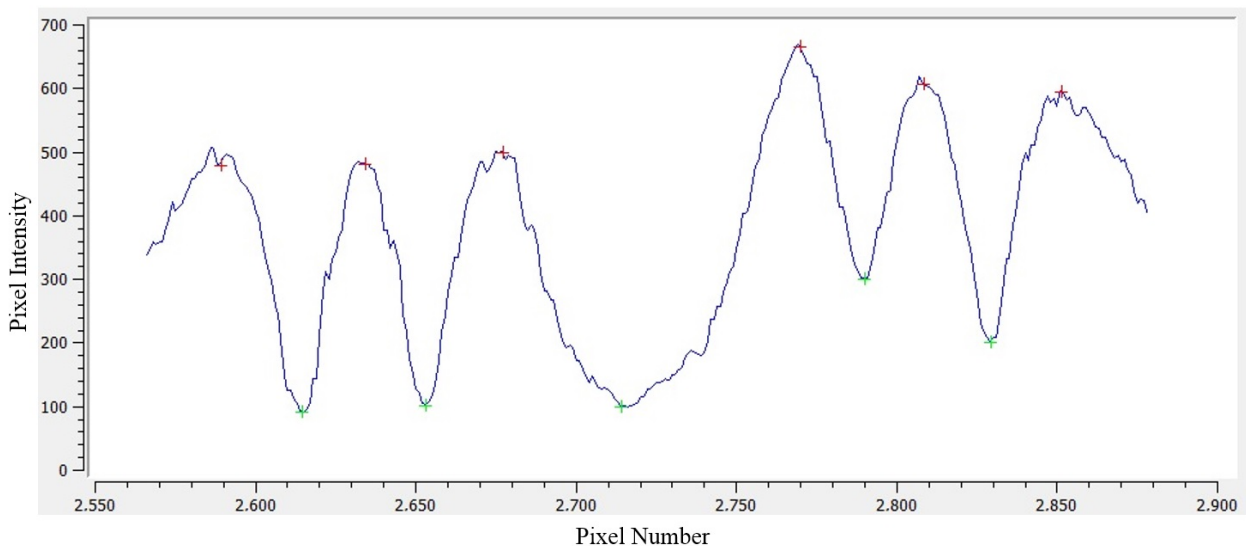


FIGURE 4.15: Pixel intensity values for the horizontal axis. A similar window also opens for the vertical axis.

Within these newly opened windows, the user has at their disposal, the spline error and integration width options to correctly identify the maximas and minimas. The spline error

defines how much deviation the programme is allowed shift the indicated relative maximums and minimums indicators, while the integration width allows the program to ‘smooth’ the image taking an average value over several pixels. Both these settings are modified so that the relative maximum and minimum indicators are correctly placed over respective maximums and minimums of the fringes. These values are kept as low as possible for the highest accuracy. However, at very low settings and depending on the quality of the images, the programme will detect individual pixels and allocate data points to them which will clearly give a false reading. With the correct data points, the third window (see Fig[4.16]) displays the Gaussian profile fitting for both axes. Here, the programme produces a Gaussian profile based on the  $\lambda/4$  spacing between successive maximums and minimums and calculates the ROC, radius ( $\sigma$ ) and depth calculations using eq.(4.9). A quadratic fit is also given as in some cases for larger ROC, this fit gives a higher confidence value for the ROC as there typically fewer data points for a satisfactory gaussian fit. However, it should be noted that this type of fitting typically gives an over-estimation of the ROC. As a means for determining the ellipticity of the indentation, the analysis axes can be rotated allowing the ellipticity to be calculated by the aspect ratio of the largest ROC with the smallest ROC at a given axis rotation.

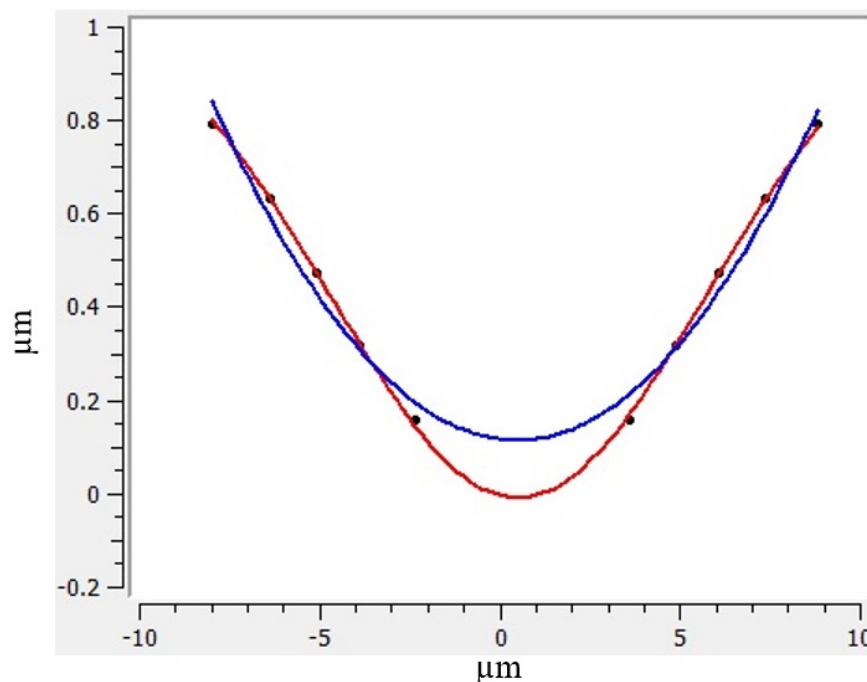


FIGURE 4.16: Gaussian profile fitting to data points. ROC, radius and depth calculations are given for both Gaussian (red) and quadratic (blue) fits. A similar graph is also given for the vertical axis. For this particular fibre the ROC was found to be  $23.8\mu\text{m}$  with a depth of  $1.18\mu\text{m}$  on the horizontal axis and  $27.6\mu\text{m}$  with a depth of  $1.21\mu\text{m}$  on the vertical axis.

### 4.3.1 Multiple Fibre Holder

To facilitate production of large numbers of fibres in a single production run, a fibre holder that could hold sixteen fibres was designed and is shown in Fig[4.17]. Fabricated from Aluminium, this would allow successive machining of sixteen fibres without the need to individually handle each fibre. This holder design is able to also hold the fibres for the DBR coating process and as such, is bead blasted to reduce flaking of material from the DBR process. The holder utilises 1.6mm diameter teflon tubes with a hollow center which allows the fibres to be held without breaking them. The teflon tubing are feed into the drilled bores and clamped in place by small screws. Teflon is used for minimal outgassing in the DBR coating process.

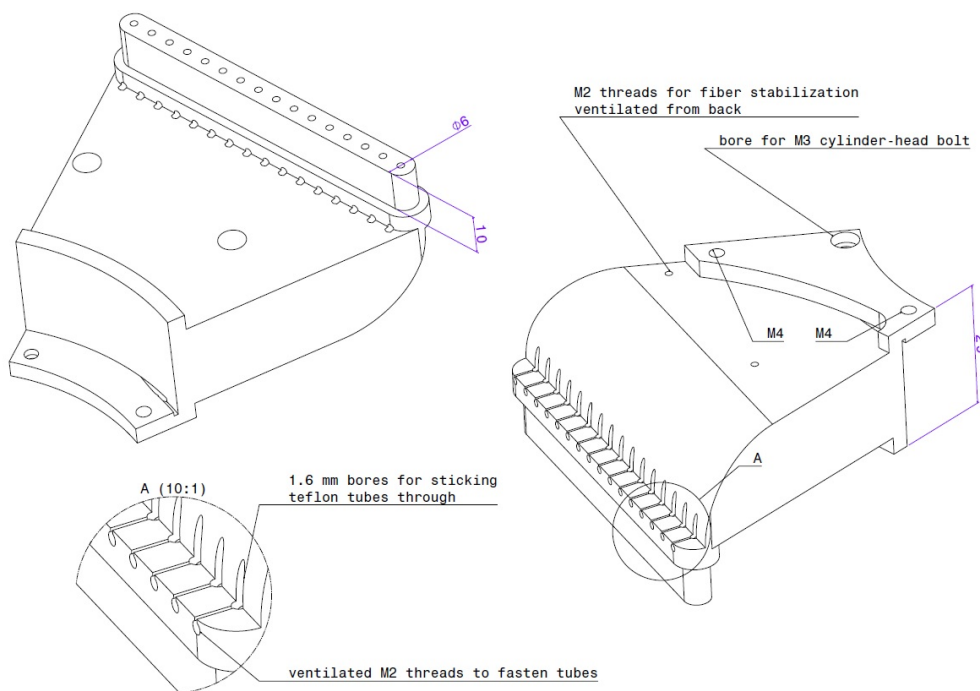


FIGURE 4.17: Fibre Holder for sixteen fibres protected with teflon tubing and secured in place with screws. This was designed using CATIA design programme and machined at Macquarie Engineering a Technical Services (METS).

To provide this fibre holder with the necessary positioning provision, a large 3-D translation stage mounting was designed and is also constructed out of Aluminium. This design employs commercially available X-Y and single Z axis translation stages to provide quick and precise positioning of the fibres for machining in a highly stable mounting. For transporting and storing these fibres once they have been machined, six fibre holders are secured on an Aluminium disk which also serves as the platform from which the fibres will be coated (see Fig[4.18]).

To transport these fibres to the coating facility, a travel holder was designed and constructed out of High Density Poly Ethylene (HDPE). This material is chosen due to very low outgassing and minimal loose particle matter qualities.

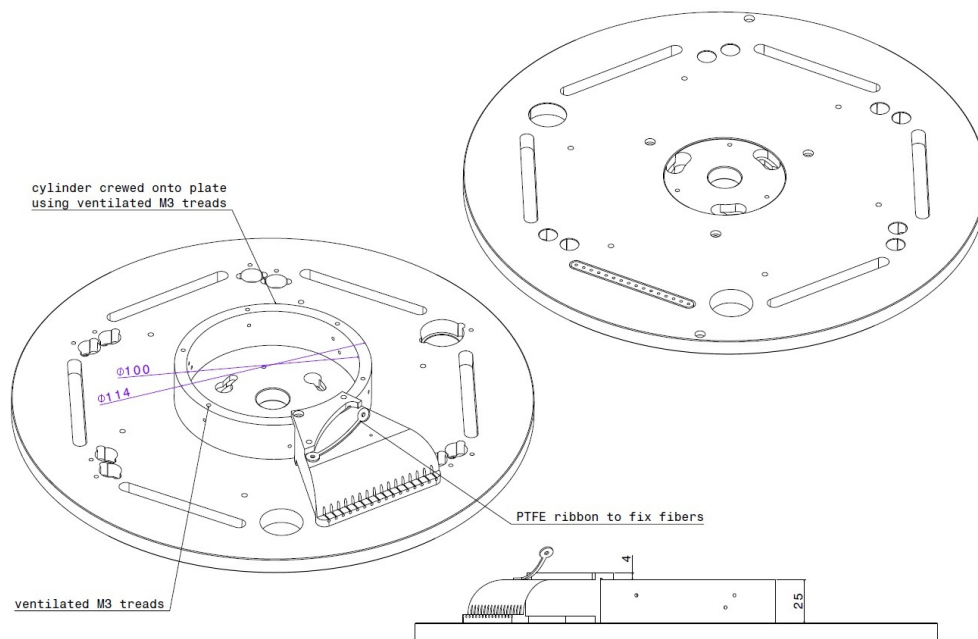


FIGURE 4.18: Fibre Transport Holding plate. The plate also serves as the platform for the DBR coating process.

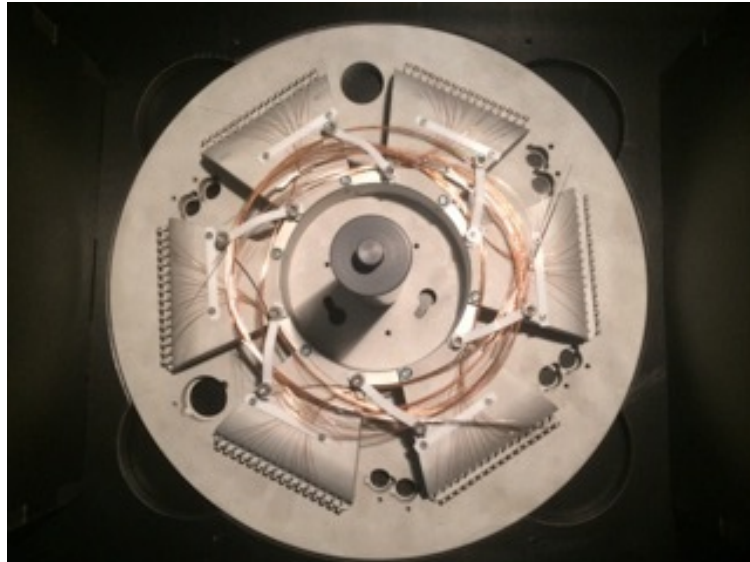


FIGURE 4.19: The complete assembly of the multiple fibre holder with fibres ready to be sent for coating.

## 4.4 Distributed Bragg Reflectors (DBR)

After machining the fibres, they are dispatched to Laseroptic GmbH Germany, to be coated with layers of dielectric material to form highly reflective mirrors (99.995%) required for the

cavity. These coatings are more commonly known as Distributed Bragg Reflectors (DBR) and are crucial to ensure high finesse, thus large Q-factors. The concept behind the operation of the DBR is similar to that of thin film reflectors. When light meets the interface between a low refractive index material and a higher refractive index material, some light is reflected and some is transmitted. The reflected light, however, has a  $\pi$  phase shift imparted on it. If the transmitted light meets a third, higher refractive index material, the reflected light will also gain a  $\pi$  phase shift. If the materials are designed to have a thickness equal to a quarter of the effective wavelength of light in each material i.e.  $\lambda/4n$ , all the reflected light will constructively interfere. In the case of DBRs, several layers of alternating refractive index dielectric material is used to the point that no light penetrates through the stack and so the reflected light back into the cavity is near unity (see Fig[3.10]). However, the DBR is only effective over a range of wavelengths centred at  $\lambda_0$ . This is the so called “stop band” [77] and is a function of the number alternating layers.

A parameter of great importance to any experimentation with polaritons is the requirement of large electric fields inside the cavity to increase the coupling strength ‘g’. This enforces the need to engineer the electric field distribution inside the cavity. The electric field inside the cavity will depend strongly on the construction of the DBR. The electric field distribution can be described using the transfer matrix method [78]. Considering a homogeneous, arbitrary planar structure in one dimension, the electric field of the forward propagating ( $E_1$ ) and back reflected ( $E_r$ ) electric fields at the boundary can be described as a two dimensional vector,

$$\begin{bmatrix} E_r \\ E_1 \end{bmatrix}, \quad (4.10)$$

When both boundaries of this structure (see Fig[4.20]) are considered, the counter-propagating electric fields on both sides can be defined by solving the Maxwell equations across the structure.

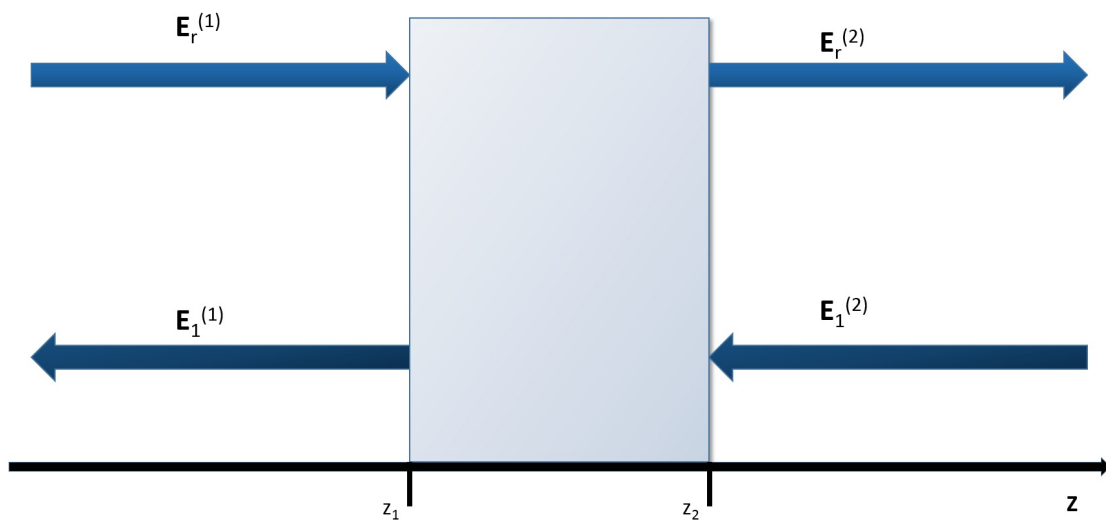


FIGURE 4.20: Transfer Matrix approach. The externally propagating fields evolve after passing through the planar structure.

This will result in a linear relationship of the electric field at both boundaries  $z_1$  and  $z_2$  given by [78],

$$\begin{bmatrix} E_r^{(2)} \\ E_1^{(2)} \end{bmatrix} = \begin{bmatrix} M_{11} & M_{12} \\ M_{21} & M_{22} \end{bmatrix} \begin{bmatrix} E_r^{(1)} \\ E_r^{(1)} \end{bmatrix}, \quad (4.11)$$

with the matrix  $M$  known as the transfer matrix. For the DBR, each layer possesses a transfer matrix. The simple matrix multiplication of all these matrices give a final transfer matrix for the entire structure and hence the electric field inside the cavity (see Fig[4.21]).

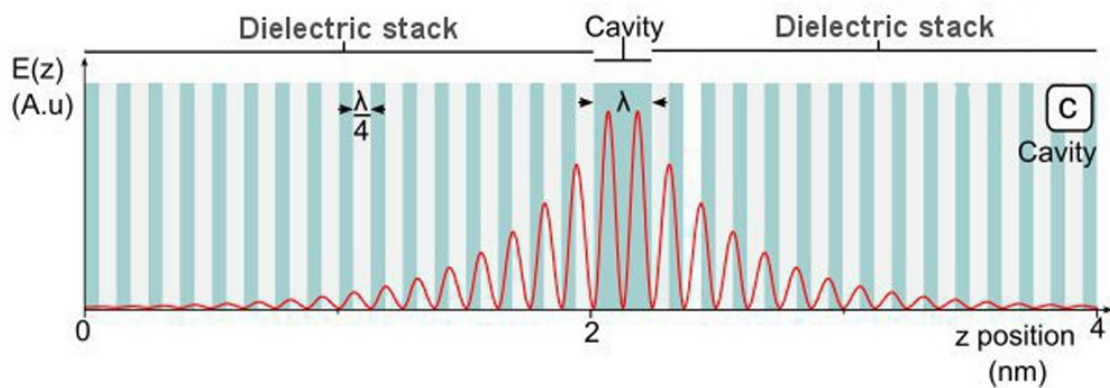


FIGURE 4.21: The electric field distribution using the transfer matrix method for a solid state microcavity. Taken from [79].

For the fibres that we produced, it was chosen that the DBR coatings will consist of 33 layers of Tantalite/Silicon dioxide ( $Ta_2O_5/SiO_2$ ) dielectric material with the stop band centre wavelength of 830nm at normal incidence shown in Fig[4.22].

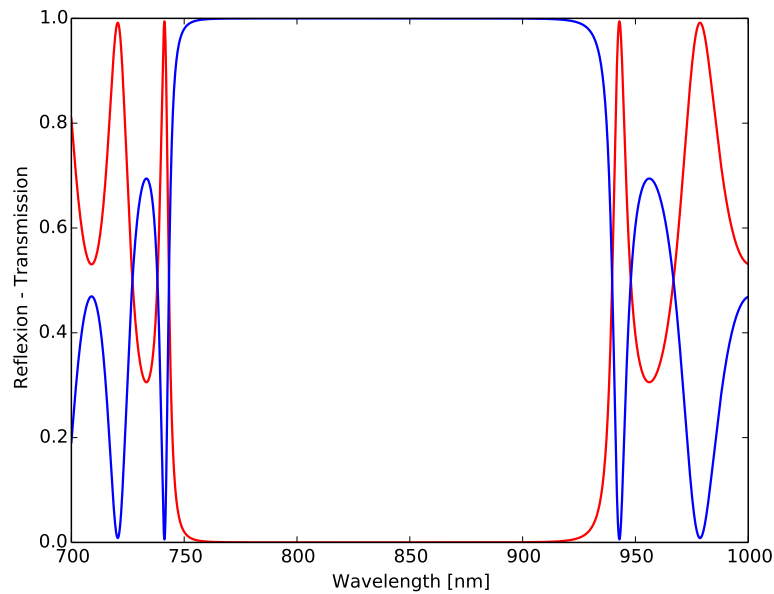


FIGURE 4.22: The function of the  $\text{Ta}_2\text{O}_5/\text{SiO}_2$  DBR coating. The red curve shows transmission and the blue curve shows reflection.

The electric field distribution inside the DBR coating and cavity is shown in Fig[4.23],

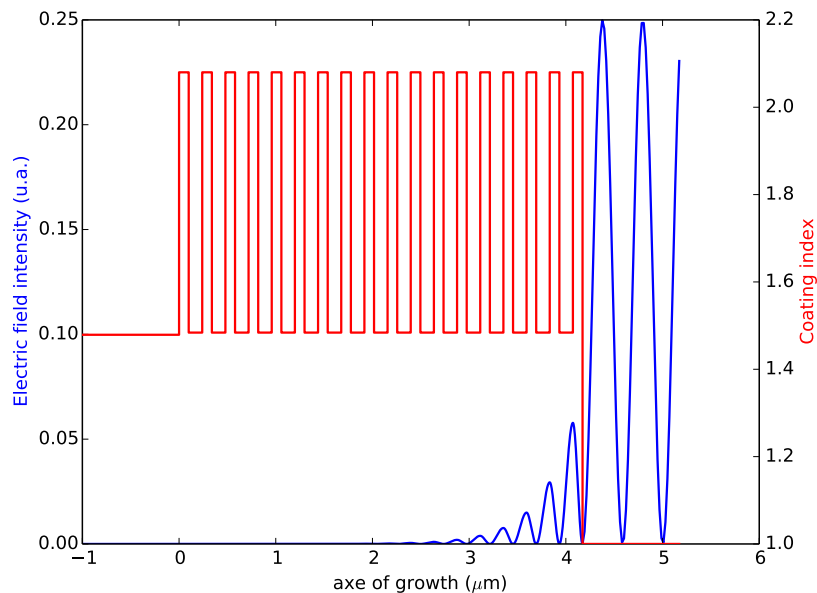


FIGURE 4.23: Electric field distribution for the dielectric DBR coating. The blue line shows the electric field inside the DBR and the red line shows the DBR profile.

and finally, the absolute transmission is shown in Fig[4.24].

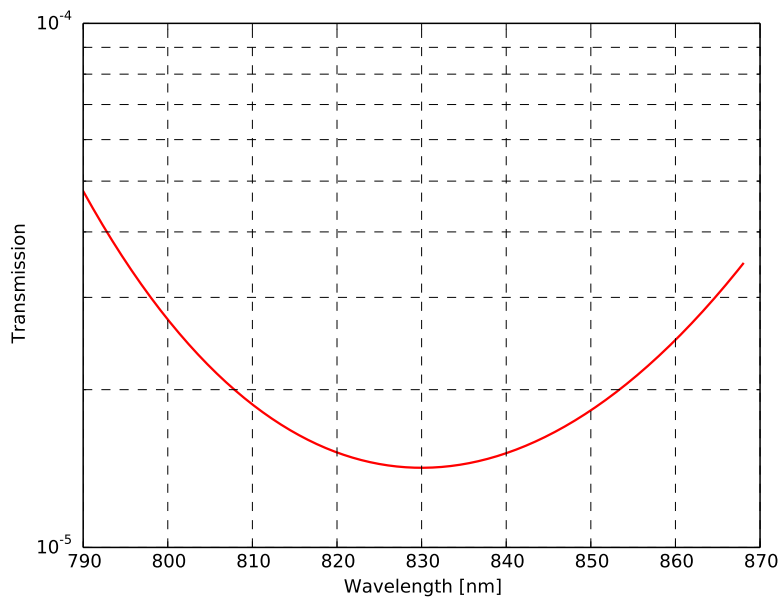


FIGURE 4.24: Transmission of the DBR coating vs. wavelength. At our operating wavelength of 830nm, transmission is approx 15ppm.

With the information provided by transfert matrix calculations (see Fig[4.24]), the transmission at 830nm is  $T = 15\text{ppm}$ . We also estimate the absorption and scattering losses to be  $A \sim 20\text{ppm}$  of  $S \sim 20\text{ppm}$  respectively. Excluding clipping and surface roughness losses, these values give an estimate for the expected cavity Finesse of  $\sim 57000$ .

# Chapter 5

## Results

This chapter presents the results of the characterisation of the fibre indentations we have produced with our FIMS setup. We will first describe the results of a surface characterization using an atomic-force microscope (AFM). In the next step we will discuss the influence of different control parameters on the fiber indentation geometries.

The fibres used in our machining process have been supplied to us by IVG Fibers and have the following specifications;

Cu800	Single mode	Multi-mode
Jacket	Copper Alloy	Copper Alloy
Wavelength Range	800-900nm	800-900nm
Mode Field Diameter	$6\pm 0.5\mu\text{m}$	Core diameter: $50\mu\text{m}$
Cladding Diameter	$125\pm 1\mu\text{m}$	$125\pm 1\mu\text{m}$

A copper alloy jacket was chosen for these fibres as they will need to resist the DBR coating process. However, these fibres must be stripped using a 70% nitric acid ( $\text{HNO}_3$ ) solution.

### AFM Characterisation

Atomic force microscopy (AFM) scans of some of our fibre indentations were performed to provide a high resolution picture of the geometries we created. These scans, while highly detailed, are time consuming and require substantial handling of the fibres after they have been machined. It is for these reasons that a laser profilometry system was chosen which provides real-time characterisation of the indentations without the need for external handling. Therefore, these AFM scans are used only as a reference to indicate the accuracy and hence validity of the laser profilometry setup. Fig[5.2] and Fig[5.1] show the AFM scans of a fibre,

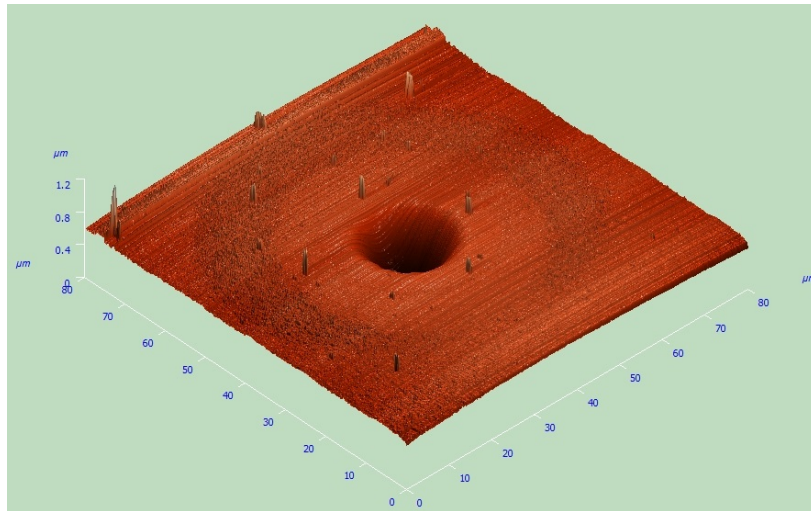


FIGURE 5.1: An  $80 \times 80 \mu\text{m}$  AFM scan of a machined fibre facet. The smoothing effect of the  $\text{CO}_2$  machining can be seen in the centre of the indentation.

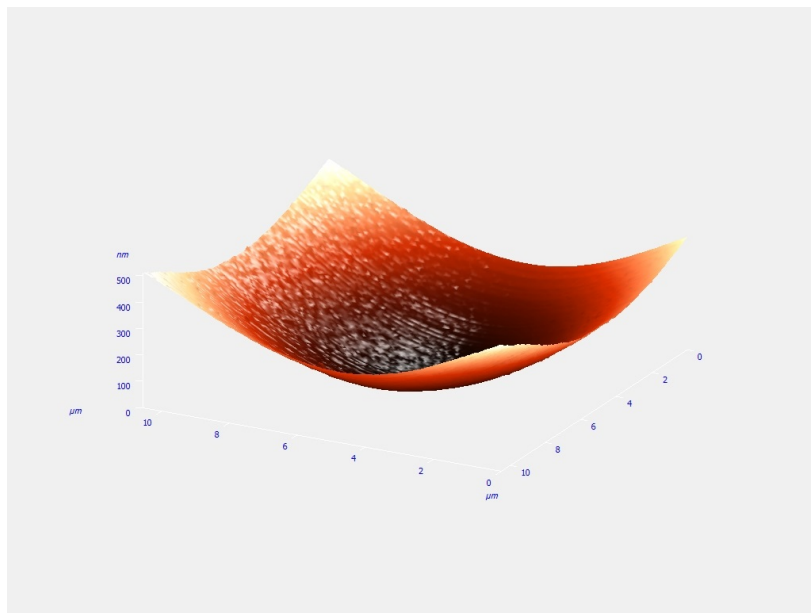


FIGURE 5.2: AFM scan of the machined indentations. The radius of curvature can be extrapolated by taking a cut through the middle of the indentation.

With data points taken  $80\text{nm}$  apart, these scans can be used to extract very precisely the geometry of the indentations with a high degree of precision. Taking a cut through the centre of the indentation produces a cross-section profile of the indentation shown in Fig[5.3].

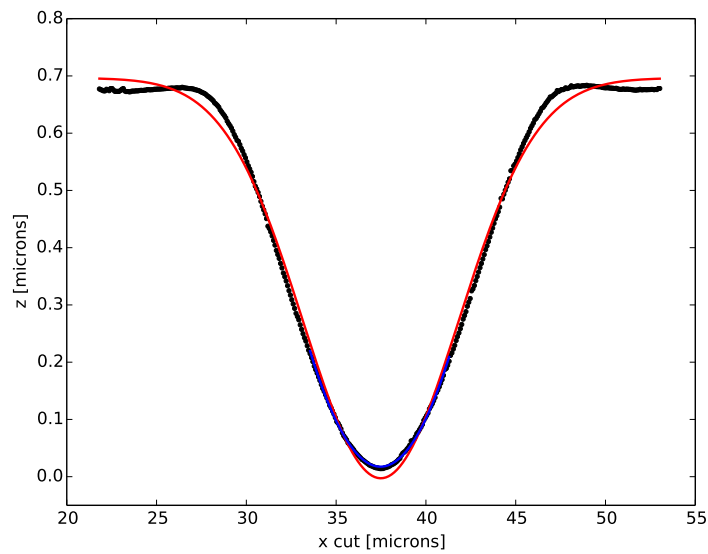


FIGURE 5.3: The indentation cross-section extracted from the AFM scan. The black curve shows the data points, the red curve shows a gaussian profile fit and the blue curve shows a quadratic fit.

This profile has both a gaussian and quadratic profile fitted from which a ROC is extracted. Using the quadratic fit, we obtain an  $ROC=35.8\mu\text{m}$ . From the gaussian fit we find that the depth and diameter of the indentation are  $A=0.7\mu\text{m}$  and  $2\sigma=8.7\mu\text{m}$  respectively. This result is compared with the laser profilometry measurements shown in Fig[5.4].

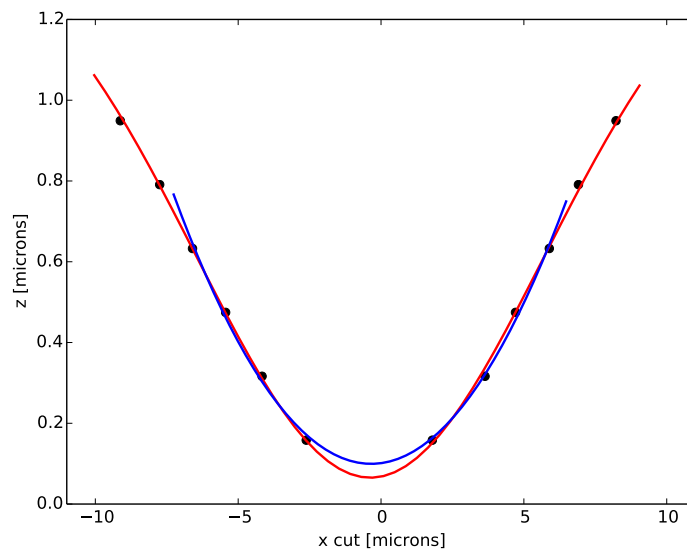


FIGURE 5.4: Laser profilometry analysis of the fibre indentation used in the AFM reading. The red curve is the gaussian fit and the blue curve is the quadratic fit.

The results obtained from the laser profilometry show that a quadratic fit yields an ROC=36 $\mu$ m, and the peak-to-valley value extracted is 0.8 $\mu$ m. These values are in good agreement with the AFM characterisation, which validates the optical characterisation of the created indentations using our profilometry setup.

AFM scans such as the ones taken here, also allows surface roughness to be extracted. Surface roughness is one of the key factors affecting the finesse and must be kept as low as possible to reduce scattering losses. The RMS-surface roughness can be calculated by integrating over the spatial frequency band of the Power Spectral Density (PSD) function given by [80],

$$\sigma^2 = \int_{f_{xmin}}^{f_{xmax}} \int_{f_{ymin}}^{f_{ymax}} S(f_x, f_y) df_x df_y, \quad (5.1)$$

where  $S(f_x, f_y)$  is the PSD function. The PSD function represents the spatial frequency spectrum of the surface deviations. The spatial frequency band is selected such that the lowest spatial frequency is limited to  $f_{min} = 1/L_{scan}$  where  $L_{scan}$  is the AFM scan length. The largest spatial frequency satisfies  $f_{max} = 2/\lambda$ , as higher frequencies do not contribute to the scattering losses. At the time of writing, time limitations prohibited an analysis of the surface roughness, however, this will be carried out in future work.

## Created Fibre Indentation geometries

We present here the created geometries' dependence with the experimental control parameters. Characterisation of the parameter space for the indentation involved three degrees of freedom which were the attenuation of the laser power, pulse duration and displacement from the beam focus. Fig[5.5] and Fig[5.6] show the depth and radius  $\sigma$  values for constant power and beam waist. The shallow depth of the indentations of  $\sim 0.8$ -1.8 $\mu$ m are ideal as this allows the ability to create short cavities thus enabling a further reduction in mode volume (see eq.(3.28)) and reduced clipping losses [76]. For a more complete analysis of clipping losses in these types of system, refer to [81]. However, in shorter cavities, Q-factor values will diminish (see eq.(3.33)) and must be considered in the final experiment. The  $\sigma$  values give the radius of the indentations which, preferably, need to be as large as possible in order to limit clipping losses for longer cavity lengths [76]. The ROC values as a function of pulse duration for individual fibres are given in Fig[5.7].

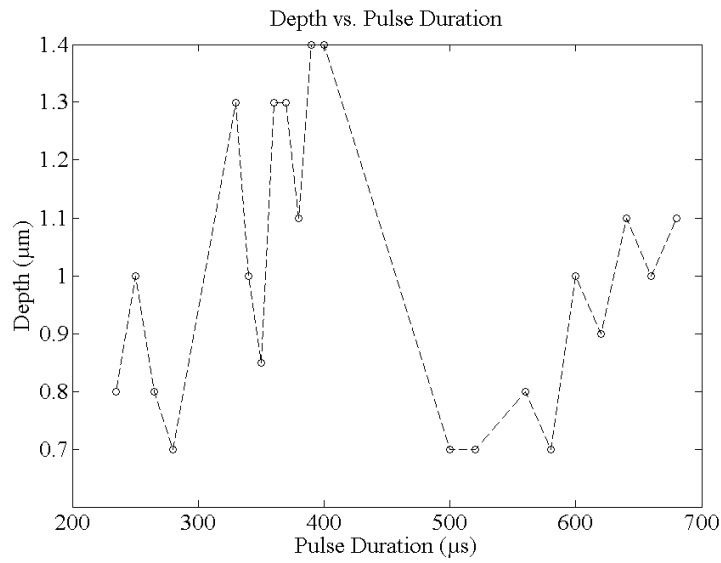


FIGURE 5.5: Indentation depth as a function of pulse duration for constant  $\text{CO}_2$  beam waist and power. The small depth of the indentation allows the possibility for small cavity lengths.

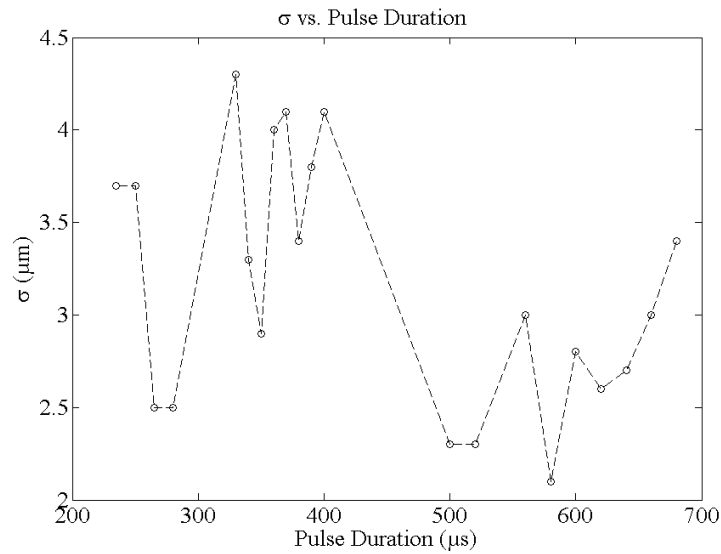


FIGURE 5.6:  $\sigma$  as a function of pulse duration for constant  $\text{CO}_2$  beam waist and power. Larger  $\sigma$  (radius) values are preferable to ensure complete intra-cavity light collection.

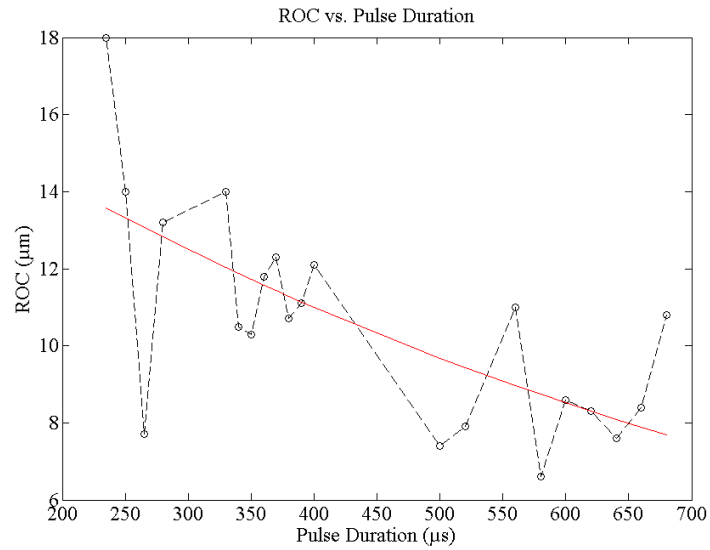


FIGURE 5.7: ROC measurements as a function of pulse duration for constant  $\text{CO}_2$  beam waist and power. The red curve is an exponential fit to the data.

The smallest ROC values gained were  $\sim 10\mu\text{m}$  with an estimated uncertainty of  $\pm 18\text{-}20\%$  for all ROC values. This estimate for the uncertainty originates from the variation of laser power output of  $\pm 3\text{-}5\%$  and the maximum fitting errors of Python program of approximately  $\sim 15\%$ . Increasing the pulse duration further than those indicated, resulted in excessive heating and rippling of the fibre surface. It should be noted that in the actual production run, two fibres were made using the same parameters which did not allow for rigorous statistically analysis of the uncertainties.

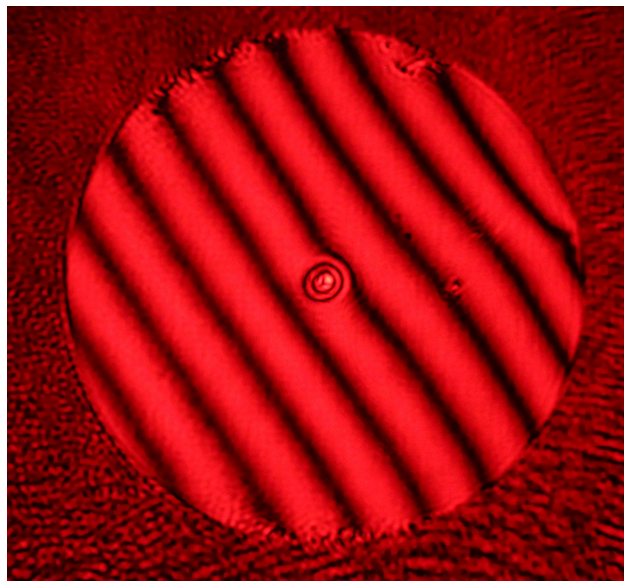


FIGURE 5.8: Interference image of fibre indentation. This indentation has an  $\text{ROC}=9.7\mu\text{m}$ ,  $\text{Depth}=1.07\mu\text{m}$  and  $\sigma=2.95\mu\text{m}$ . The pulse duration was  $265\mu\text{s}$ .

The smaller ROC values we obtained with this setup compare favourably with those produced in similar systems which use fused ion beam milling on planar substrates [82]. With the ability to create indentations with ROCs smaller than the intended  $10\mu\text{m}$ , large ROCs indentations are also explored through displacement of fibres from the beam focus. By displacing the fibres out of focus of the  $\text{CO}_2$  beam, the transverse beam size increases, flattening the intensity profile, thus enlarging the ROC. For constant attenuation and pulse duration, the ROC values for increasing displacement from the focus is shown in Fig[5.9].

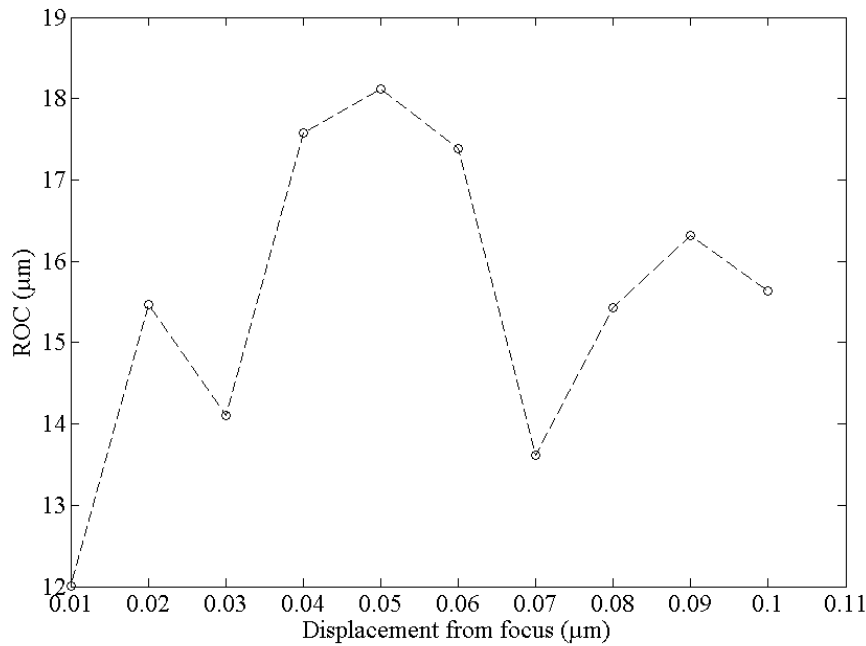


FIGURE 5.9: ROC as a function of displacement from the  $\text{CO}_2$  focus. ROC is generally larger for increasing distance from the focus of the  $\text{CO}_2$  laser beam. The pulse duration is  $500\mu\text{s}$ .

Generally, there is a trend for larger ROC with increasing displacement, however, due to beam astigmatism, ellipticity begins to deteriorate as the fibre is moved away from the focus. As a means of overcoming this limitation, beam expander manipulation is used to change the beam waist size without changing the position of the beam focus. The ROC values for a another beam expander setting are given in Fig[5.10].

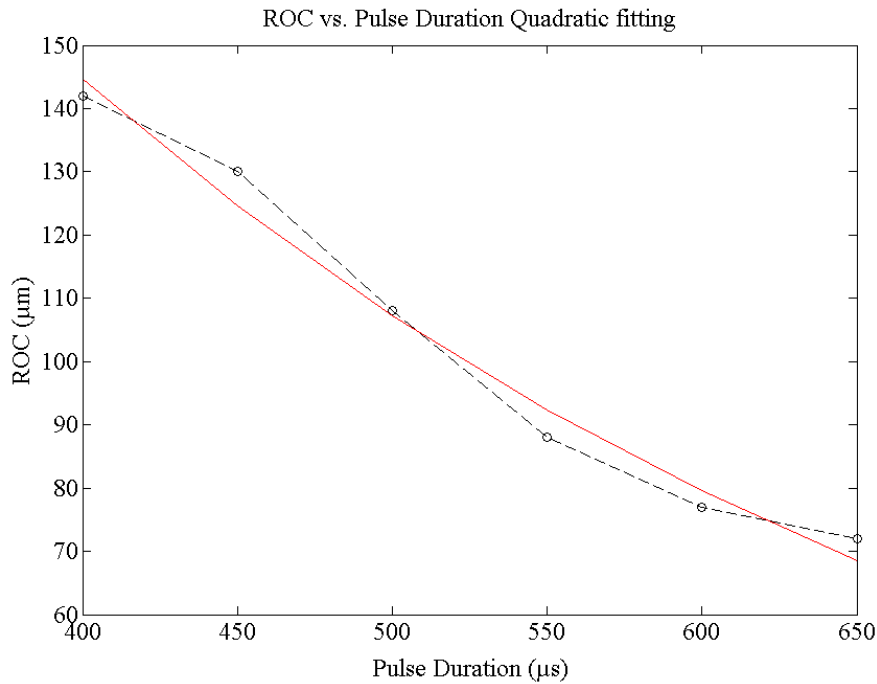


FIGURE 5.10: ROC as a function of pulse duration. The beam expander is moved from its ideal smaller ROC position. The red curve is an exponential fit to the data. A slight increase in power (7% compared to the previous data sets) is required to compensate for the larger transverse beam size.

It should be noted for Fig[5.10], the ROC values are calculated using quadratic fitting. This fitting is used in this case due to the lack of data points extracted from the interference image due to the very shallow structure created for these particular parameters. However, there is a clear increase in ROC for decreasing pulse duration. This defines the range of ROCs accessible in our setup to 8-150  $\mu\text{m}$ . In this case, the ROC values are too large for our needs. Further beam expander adjustments were made by moving back closer the original setting such that ROC values in the 20-60 $\mu\text{m}$  range were achieved (see Fig[5.11]). As a point of interest, several fibres were machined with multiple indentations as shown in Fig[5.12].

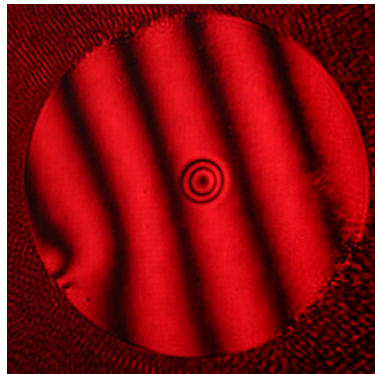


FIGURE 5.11: Interference image of a large ROC indentation. ROC=29.1 $\mu\text{m}$ , depth=1.07 $\mu\text{m}$ ,  $\sigma$ =5.6 $\mu\text{m}$ . pulse duration=510 $\mu\text{s}$ .

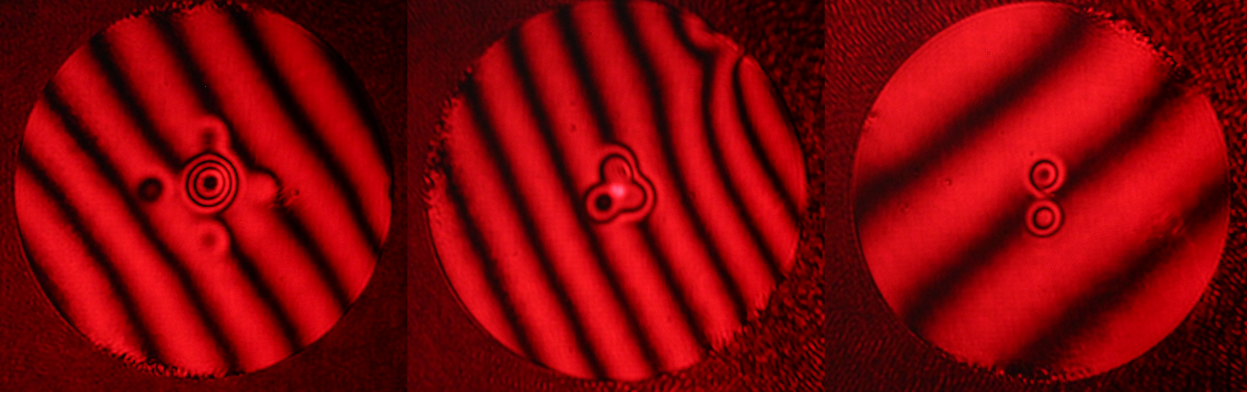


FIGURE 5.12: Multi-structure indentations. The fibre on the left has a large diameter indentation in the centre, surrounded by four smaller diameter indentations, with different spacing from the centre. The other two fibres show a triplet and doublet of indentations centred around the fibre core.

These structure have never been attempted in fiber-microcavity studies before, and it is anticipated that using these multiple indents it may be possible to create a small array of coupled cavities.

## 5.1 Next Steps

At the time of writing, we have prepared, machined and shipped the fibres which are currently undergoing the DBR coating process. Upon receiving the fibres, experimentation will take place in our low-temperature cavity lab at CSIRO Lindfield. We will first characterize the coatings once the fibers are returned. Potentially the fibers will have to be annealed to make sure the coatings reach their specifications. Once this is done, we will use the fibres to study mechanically tunable polariton systems with the particular goal of reaching the regime of strongly interacting polaritons. Based on the parameters of the fibre mirrors we have fabricated we can estimate the expected interaction strength for our polaritons. Using an estimated interaction constant of  $\kappa^{int}=10\mu\text{eV}/\mu\text{m}^2$  for the Quantum well samples, we estimate the nonlinear co-efficient as function of indentation ROC for constant cavity length using the definition,

$$\omega_{nl} = \frac{\kappa^{int}}{\lambda\sqrt{L(R-L)}}, \quad (5.2)$$

where  $R$  is the ROC of the mirror,  $L$  is the cavity length and  $\lambda$  is the wavelength. The resulting graphs are shown in Fig[5.13].

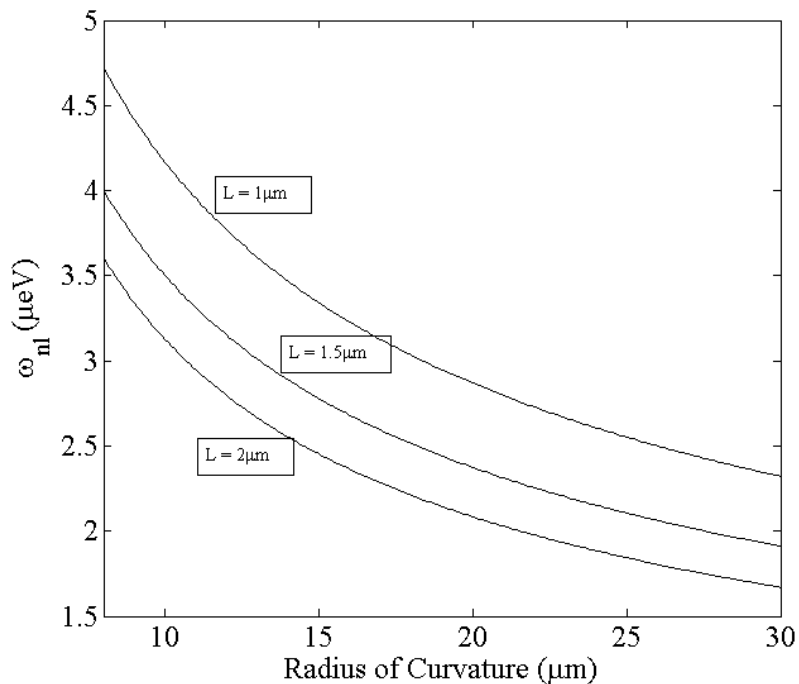


FIGURE 5.13: The nonlinear co-efficient as function of fibre indentation ROC at three different constant cavity lengths of 1, 1.5 and 2  $\mu\text{m}$ .

The values given here for the nonlinear co-efficient should be seen as an upper limit for this parameter. It is uncertain at this time if these results are adequate to reach the regime of strongly interacting polaritons and will depend on the quality of the externally-sourced narrow linewidth quantum well samples. However, comparing these values of the nonlinear co-efficient to other literature [82], values of  $6.8\mu\text{eV}$  are achievable using our estimated interaction constant and cavity length of  $1\mu\text{m}$ . While our results are inferior, they are adequate, provided that the QW linewidth is sufficiently small. The experiment will employ these samples centred at 830 nm and cooled down to liquid-Helium temperatures. In order to probe potential quantum correlations between polaritons, we will carry out autocorrelation measurements determining  $g^{(2)}(\tau)$  both in resonant and photo-luminescence spectroscopy. The sample will be held inside a cylinder suspended at the end of a cage system which is called a “cane”. Photographs of the cane and the cylinder with the sample and the cavity are shown in Fig[5.14].

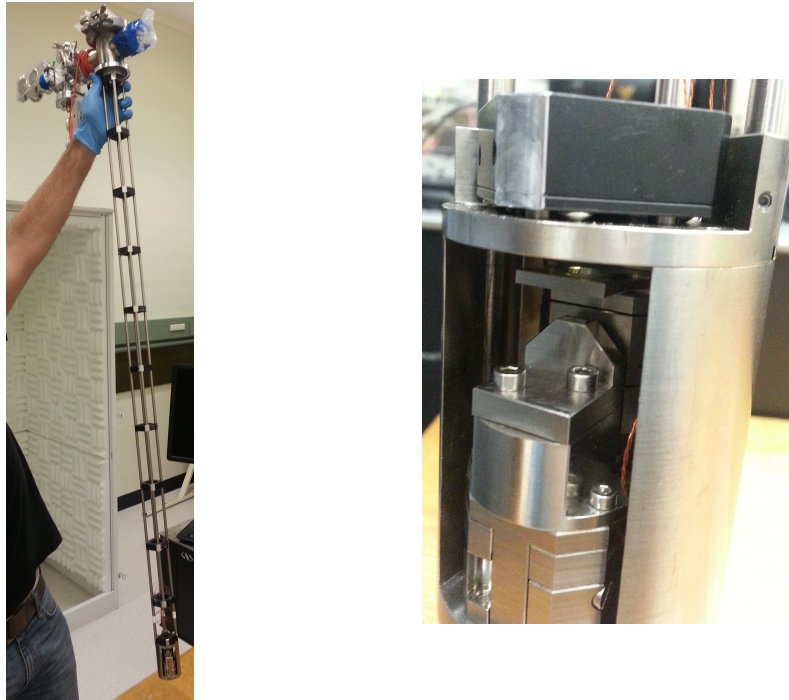


FIGURE 5.14: The left images shows the “cane”. The cylinder at the end of the cane (right image) houses the sample and the fibre microcavity. The light from the cavity is collected through a lens at the top of the cylinder and propagates up the cane through a vacuum window at the very top. The light is then collected and sent to the spectrometer for analysis. The relative position of fiber tip and sample is controlled through a stack of low-temperature slip-stick nanopositioners from attocube. The whole dewar is standing in a home-built acoustically shielded box shown in the background of the left photo.

The fibre is fed down the cane to the cylinder through one of the support tubes. In the cylinder, the fibre is held in place by a V-groove holder and is facing back up towards the top. Three low temperature, nanopositioning attocube translation stages are used to control the accurate alignment of fibre and sample. The sample is suspended above the fibre and the light transmitted by the cavity travels through the top of the cylinder, is collected and focussed by a lens and sent up through the middle of the cane. The light is then extracted from the cane through the top port. The entire device is then placed inside a liquid-Helium dewar and cooled down to 4K. The dewar itself is placed inside a acoustically insulated booth shown in the background of Fig[5.14].

The laser sources available are a pulsed Ti:Sapphire laser (Coherent, MIRA) capable of operating both in CW and picosecond mode, as well as a widely tunable CW Ti:Sapphire laser (M Squared, SOLSTIS). Both lasers can operate between 700nm and 1000nm, but will be used in the 800nm wavelength range for the polariton experiments. Beam preparation incorporates power stabilisation through the use of AOMs and electronic feedback loops.

Experimental measurements will include resonant probing, photo-luminescence spectroscopy and most importantly  $g^{(2)}(\tau)$  measurements. For resonant probing, the wavelength of the cw laser is scanned across the polariton/cavity resonances and the intensity of the signal transmitted through the system is detected using APDs. The MIRA (CW mode)

---

will be used around 780nm to off-resonantly excite the polaritonic system for performing photo-luminescence spectroscopy. The photo-luminescence signal is analysed using a high-resolution spectrometer from ACTON with an integrated Princeton CCD camera. Auto-correlation measurements of  $g^{(2)}(\tau)$  will be carried out using a Hanbury Brown and Twiss interferometer setup as outlined in section 2.3. If necessary, the collected photons can be filtered through the spectrometer before sending them for autocorrelation analysis. The APDs from idQuantique have a timing resolution of 40ps and 7% efficiency at 800nm. We also plan to image the back/plane of the polariton system using a CCD camera to gather information about the spatial mode structure in the fiber cavity.

# Chapter 6

## Future Work

The present work on setting up a fibre machining system capable of producing large quantities fibres with small curvature radii with direct capability to image and analyze the mirror indents is a real technological advancement for the our group. This setup is the first of its kind in Australia and gives the group a unique capability in the Australian scientific community.

In terms of polariton research: with small curvature radii fibre cavities, there is a direct route towards entering the regime of polariton blockade. Besides fibres, new samples with very small amount of disorder will be sourced from LPN through a collaboration with Arisitide Lemaitre, Alberto Amo, and Jaqueline Bloch. This should allow for clean studies of polariton interactions (in particular polariton blockade) and for detailed studies of the Feshbach resonance effect through correlation measurements. A fibre-cavity investigation on Feshbach resonances could yield new insights since the Deveaud group used planar samples in their study [83]. On a more practical side we plan to investigate an electrically driven polariton laser with our fibre cavity system in collaboration with the LPN team. Next steps will also include the study of light carrying orbital angular momentum and the potential creation of quantum-Hall states of light [84] with our fibre cavity setup. Another direction to explore is coupled cavities: the very preliminary multi-indent structures presented in chapter 5 will be interesting to study. The goal here could be to create a small scale Tonks-Girardeau gas of polaritons/photons as suggested in [85]. Once the optimal parameters for reaching strongly interacting polaritons are found, integrated designs based on fibre cavities and on-chip waveguides could be envisaged. Ultimately, the information gained with our fibre-cavity setup could also be employed to design fully-integrated coupled cavity arrays on a chip, similar to [86], for large scale quantum simulation with polaritons/photons [87].

Besides research on quantum-well polaritons, fibre cavities will also be used to study other emitter systems. An immediate project involves the coupling of up-conversion nanocrystals [88] to the fibre cavities in the quest for single-particle nanolasing. Another very active area of research in the group are diamond-based colour centres, in particular NV centres and SiV centres. While NV centers have been coupled to fiber cavities at room temperature [89, 90], there is no report of low-temperature coupling, let alone of reaching the strong coupling regime.

At present, the group is fabricating a second batch of fibre mirrors that will have a

coating suitable for both NV centres and SiV centres. With our low-temperature fibre cavity microscope, we will be ready to perform low-temperature cavity experiments immediately. In particular, there is good prospect of reaching the strong coupling regime for SiV centres due to their favourable optical properties [91]. In terms of NV centres coupled to fibre cavities, there are ideas for building a fibre cavity quantum interface to optically interconnect distant superconducting quantum chips [92].

In addition to the many research directions opened up within the group itself, other researchers in Australia working on atomic physics experiments have already shown interest in using our fibre machining setup to make fibres for atomic cavity-QED experiments. With all of these prospects and open research directions, the fibre machining setup described in this thesis will be a catalyst for many future experiments.

# References

- [1] H. Mabuchi and A. C. Doherty. *Cavity quantum electrodynamics: Coherence in context*. Science **298**(5597), 1372 (2002).
- [2] H. Kim, R. Bose, T. Shen, G. Solomon, and E. Waks. *A quantum logic gate between a solid-state quantum bit and a photon*. Nature Photonics **7**, 373 (2013).
- [3] D. G. Angelakis, M. F. Santos, and S. Bose. *Photon-blockade-induced Mott transitions and  $xy$  spin models in coupled cavity arrays*. Phys. Rev. A **76**, 031805 (2007).
- [4] M. J. Hartmann, F. G. S. L. Brandao, and M. B. Plenio. *Strongly interacting polaritons in coupled arrays of cavities*. Nature Physics **2**, 849 (2006).
- [5] A. Greentree, C. Tahan, J. Cole, and L. Hollenberg. *Quantum phase transitions of light*. Nature Physics **2**, 856 (2006).
- [6] E. Jaynes and F. W. Cummings. *Comparison of quantum and semiclassical radiation theories with application to the beam maser*. Proceedings of the IEEE **51**(1), 89 (1963).
- [7] A. Imamoglu, H. Schmidt, G. Woods, and M. Deutsch. *Strongly interacting photons in a nonlinear cavity*. Phys. Rev. Lett. **79**, 1467 (1997).
- [8] K. M. Birnbaum, A. Boca<sup>1</sup>, R. Miller, A. D. Boozer, T. E. Northup, and H. J. Kimble. *Photon blockade in an optical cavity with one trapped atom*. Nature **436**, 87 (2005).
- [9] B. Dayan, A. Parkins, T. Aoki, E. Ostby, K. Vahala, and H. Kimble. *Photon turnstile dynamically regulated by one atom*. Science **319**, 1062 (2008).
- [10] A. Faraon, I. Fushman, D. Englund, N. Stoltz, P. Petroff, and J. Vuckovic. *Coherent generation of non-classical light on a chip via photon-induced tunnelling and blockade*. Nature Physics **4**, 859 to 863 (2008).
- [11] A. Reinhard, T. Volz, M. Winger, A. Badolato, K. J. Hennessy, E. L. Hu, and A. Imamoglu. *Strongly correlated photons on a chip*. Nature Photonics **6**, 93 to 96 (2012).
- [12] C. Lang, D. Bozyigit, C. Eichler, L. Steffen, J. M. Fink, A. A. Abdumalikov, M. Baur, S. Filipp, M. P. da Silva, A. Blais, and A. Wallraff. *Observation of resonant photon blockade at microwave frequencies using correlation function measurements*. Phys. Rev. Lett. **106**, 243601 (2011).

- [13] T. Volz, A. Reinhard, M. Winger, A. Badolato, K. J. Hennessy, E. L. Hu, and A. Imamoglu. *Ultrafast all-optical switching by single photons*. Nature Photonics **6**, 607 (2012).
- [14] D. Englund, A. Majumdar, M. Bajcsy, A. Faraon, P. Petroff, and J. Vuckovic. *Ultrafast photon-photon interaction in a strongly coupled quantum dot-cavity system*. Phys. Rev. Lett. **108**, 093604 (2012).
- [15] R. Bose, D. Sridharan, H. Kim, G. Solomon, and E. Waks. *Low-photon-number optical switching with a single quantum dot coupled to a photonic crystal cavity*. Physical Review Letters **108**, 227402 (2012).
- [16] V. Loo, C. Arnold, O. Gazzano, A. Lemaitre, I. Sagnes, O. Krebs, P. Voisin, P. Senellart, and L. Lanco. *Optical nonlinearity for few-photon pulses on a quantum dot-pillar cavity device*. Phys. Rev. Lett. **109**, 166806 (2012).
- [17] C. Weisbuch, M. Nishioka, A. Ishikawa, and Y. Arakawa. *Observation of the coupled exciton-photon mode splitting in a semiconductor quantum microcavity*. Phys. Rev. Lett. **69**, 3314 (1992).
- [18] S. P. A. Imamoglu, R. J. Ram and Y. Yamamoto. *Nonequilibrium condensates and lasers without inversion: Exciton-polariton lasers*. Physics Review A **53**, 4250 (1996).
- [19] M. H. Anderson, J. R. Ensher, M. R. Matthews, C. E. Wieman, and E. A. Cornell. *Observation of Bose-Einstein condensation in a dilute atomic vapor*. Science **269**(5221), 198 (1995).
- [20] K. B. Davis, M. O. Mewes, M. R. Andrews, N. J. van Druten, D. S. Durfee, D. M. Kurn, and W. Ketterle. *Bose-Einstein condensation in a gas of sodium atoms*. Phys. Rev. Lett. **75**, 3969 (1995).
- [21] J. Kasprzak, M. Richard, S. Kundermann, A. Baas, J. K. P. Jeambrun, F. Marchetti, M. Szymanska, R. Andre, J. Staehli, V. Savona, P. Littlewood, B. Deveaud, and L. S. Dang. *Bose-Einstein condensation of exciton polaritons*. Nature **443**, 409 to 414 (2006).
- [22] H. Deng, H. Haug, and Y. Yamamoto. *Exciton-polariton Bose-Einstein condensation*. Rev. Mod. Phys. **82**, 1489 (2010).
- [23] R. Balili, V. Hartwell, D. Snoke, L. Pfeiffer, and K. West. *Bose-Einstein condensation of microcavity polaritons in a trap*. Science **316**(5827), 1007 (2007).
- [24] H. Deng, D. Press, S. Götzinger, G. S. Solomon, R. Hey, K. H. Ploog, and Y. Yamamoto. *Quantum degenerate exciton-polaritons in thermal equilibrium*. Phys. Rev. Lett. **97**, 146402 (2006).
- [25] I. Carusotto and C. Ciuti. *Quantum fluids of light*. Rev. Mod. Phys. **85**, 299 (2013).

- [26] A. Amo, J. Lefrere, S. Pigeon, C. Adrados, C. Ciuti, I. Carusotto, R. Houdre, E. Giacobino, and A. Bramati. *Superfluidity of polaritons in semi-conductor microcavities*. Nature Physics **5**, 805 to 810 (2009).
- [27] S. Utsunomiya, L. Tian, G. Roumpos, C. W. Lai, T. F. N. Kumada, M. Kuwata-Gonokami, A. Loer, and S. Ho. *Observation of Bogoliubov excitations in exciton polariton condensates*. Nature Physics **4**, 700 (2008).
- [28] V. Kohnle, Y. Léger, M. Wouters, M. Richard, M. T. Portella-Oberli, and B. Deveaud-Plédran. *From single particle to superfluid excitations in a dissipative polariton gas*. Phys. Rev. Lett. **106**, 255302 (2011).
- [29] K. G. Lagoudakis, B. Pietka, M. Wouters, R. André, and B. Deveaud-Plédran. *Coherent oscillations in an exciton-polariton Josephson junction*. Phys. Rev. Lett. **105**, 120403 (2010).
- [30] K. G. Lagoudakis, M. Wouters, M. Richard, A. Baas, I. Carusotto, R. Andre, L. S. Dang, and B. Deveaud-Pledran. *Quantized vortices in an excitonpolariton condensate*. Nature Physics **4**, 706 (2008).
- [31] K. G. Lagoudakis, T. Ostatnický, A. V. Kavokin, Y. G. Rubo, R. André, and B. Deveaud-Plédran. *Observation of Half-Quantum Vortices in an Exciton-Polariton Condensate*. Science **326**, 974 (2009).
- [32] D. Sanvitto, F. M. Marchetti, M. H. Szymaska, G. Tosi, M. Baudisch, F. P. Laussy, D. N. Krizhanovskii, M. S. Skolnick, L. Marrucci, A. Lematre, J. Bloch, C. Tejedor, and L. Via. *Persistent currents and quantized vortices in a polariton superfluid*. Nature Physics **6**, 527 (2010).
- [33] A. Amo, S. Pigeon, D. Sanvitto, V. G. Sala, R. Hivet, I. Carusotto, F. Pisanello, G. Lemenager, R. Houdre, E. Giacobino, C. Ciuti, and A. Bramati. *Hydrodynamic solitons in polariton superfluids*. Science **332**, 1167 (2011).
- [34] A. Verger, C. Ciuti, and I. Carusotto. *Polariton quantum blockade in a photonic dot*. Physical Review B **73**(19), 193306 (2006).
- [35] D. Jaksch, J. I. Cirac, P. Zoller, S. L. Rolston, R. Côté, and M. D. Lukin. *Fast quantum gates for neutral atoms*. Phys. Rev. Lett. **85**, 2208 (2000).
- [36] C. Chin, R. Grimm, P. Julienne, and E. Tiesinga. *Feshbach resonances in ultracold gases*. Rev. Mod. Phys. **82**, 1225 (2010).
- [37] I. Carusotto, T. Volz, and A. Imamoglu. *Feshbach blockade: Single photon nonlinear optics using resonantly enhanced cavity polariton scattering from biexciton states*. Europhysics Letters **90**, 37001 (2010).
- [38] N. Takemura, S. Trebaol, M. Wouters, M. Portella-Oberli, and B. Deveaud. *Polaritonic Feshbach resonance*. Nature Physics **10**, 500 (2014).

- [39] V. Negoita, D. W. Snoke, and K. Eberl. *Stretching quantum wells: A method for trapping free carriers in gas heterostructures*. Applied Physics Letters **75**(14), 2059 (1999).
- [40] E. Wertz, L. Ferrier, D. D. Solnyshkov, R. Johne, D. Sanvitto, A. Lematre, I. Sagnes, R. Grousson, A. V. Kavokin, P. Senellart, and et. al. *Spontaneous formation and optical manipulation of extended polariton condensates*. Nature Physics **6**, 860 (2010).
- [41] A. Amo, S. Pigeon, C. Adrados, R. Houdré, E. Giacobino, C. Ciuti, and A. Bramati. *Light engineering of the polariton landscape in semiconductor microcavities*. Phys. Rev. B **82**, 081301 (2010).
- [42] O. El Daif, A. Baas, T. Guillet, J.-P. Brantut, R. I. Kaitouni, J. L. Staehli, F. Morier-Genoud, and B. Deveaud. *Polariton quantum boxes in semiconductor microcavities*. Applied Physics Letters **88**(6), 061105 (2006).
- [43] L. Ferrier, E. Wertz, R. Johne, D. D. Solnyshkov, P. Senellart, I. Sagnes, A. Lemaitre, G. Malpuech, and J. Bloch. *Interactions in confined polariton condensates*. Phys. Rev. Lett. **106**, 126401 (2011).
- [44] S. Azzini, D. Gerace, M. Galli, I. Sagnes, R. Braive, A. Lematre, J. Bloch, and D. Bajoni. *Ultra-low threshold polariton lasing in photonic crystal cavities*. Applied Physics Letters **99**(11), 111106 (2011).
- [45] C. Grossmann, C. Coulson, G. Christmann, I. Farrer, H. E. Beere, D. A. Ritchie, and J. J. Baumberg. *Tuneable polaritonics at room temperature with strongly coupled tamm plasmon polaritons in metal/air-gap microcavities*. Applied Physics Letters **98**(23), 231105 (2011).
- [46] S. Dufferwiel, F. Fras, A. Trichet, P. M. Walker, F. Li, L. Giriunas, M. N. Makhonin, L. R. Wilson, J. M. Smith, E. Clarke, M. S. Skolnick, and D. N. Krizhanovskii. *Strong exciton-photon coupling in open semiconductor microcavities*. Applied Physics Letters **104**(19), 192107 (2014).
- [47] B. Besga, C. Vaneph, J. Reichel, J. Esteve, A. Reinhard, J. Miguel-Sanchez, A. Imamoglu, and T. Volz. *Polariton boxes in a tunable fiber cavity*. ArXiv e-prints (2013). [1312.0819](#).
- [48] J. Miguel-Sanchez, A. Reinhard, E. Togan, T. Volz, A. Imamoglu, B. Besga, J. Reichel, and J. Esteve. *Cavity quantum electrodynamics with charge-controlled quantum dots coupled to a fiber Fabry–Perot cavity*. New Journal of Physics **15**, 045002 (2013).
- [49] A. Reinhard. *Strong Photon-Photon Interactions in Solid State Cavity QED*. Ph.D. thesis, ETH Zürich (2013).
- [50] Y. Wu and X. Yang. *Strong-Coupling Theory of Periodically Driven Two-Level Systems*. Physical Review Letters **98**(1), 013601 (2007).

- [51] I. V. Volovich. *Photon Antibunching, Sub-Poisson Statistics and Cauchy-Bunyakovsky and Bell's Inequalities*. ArXiv e-prints (2011). [1106.1892](#).
- [52] R. H. Brown and R. Q. Twiss. *A test of a new type of stellar interferometer on sirius*. Nature **178**, 1064 to 1068 (1956).
- [53] Y. Yamamoto and A. Imamogulu. *Mesoscopic Quantum Optics* (John Wiley and Sons Inc, New Jersey, USA, 1999).
- [54] T. Aichele, A. Tribu, G. Sallen, J. Bocquel, E. Bellet-Amalric, C. Bougerol, J.-P. Poizat, K. Kheng, R. André, S. Tatarenko, and H. Mariette. *CdSe quantum dots in ZnSe nanowires as efficient source for single photons up to 220 K*. Journal of Crystal Growth **311**, 2123 (2009).
- [55] S. Franchi, G. Trevisi, L. Seravalli, and P. Frigeri. *Quantum dot nanostructures and molecular beam epitaxy*. Progress in Crystal Growth and Characterization of Materials **47**(23), 166 (2003). Vapour Growth of Bulk Crystals and Epitaxy: Part I Vapour Growth of Bulk Crystals and Epitaxy: Part I.
- [56] I. N. Stranski and L. V. Krastanow. *Abhandlungen der Mathematisch-Naturwissenschaftlichen Klasse Iib*. Akademie der Wissenschaften Wien **146**, 797 (1939).
- [57] D. Leonard, M. Krishnamurthy, C. M. Reaves, S. P. Denbaars, and P. M. Petroff. *Direct formation of quantum sized dots from uniform coherent islands of ingaas on gaas surfaces*. Applied Physics Letters **63**(23), 3203 (1993).
- [58] M. Winger. *Mesoscopic Cavity QED with a Single Quantum Dot*. Ph.D. thesis, ETH Zürich (2009).
- [59] J. D. Joannopoulos, P. R. Villeneuve, and S. Fan. *Photonic crystals*. Solid State Communications **102**(2), 165 (1997).
- [60] K. Hennessy, A. Badolato, M. Winger, D. Gerace, M. Atatre, S. Gulde, S. Flt, E. L. Hu, and A. Imamolu. *Quantum nature of a strongly coupled single quantum dotcavity system*. Nature **445**, 896 to 899 (2007).
- [61] H. Lana and Y. Dinga. *Ordering, positioning and uniformity of quantum dot arrays*. Nano Today **7**, 94 to 123 (2012).
- [62] F. Illuminati. *Quantum optics: Light does matter*. Nature Physics **2**, 803 (2006).
- [63] A. Dousse, L. Lanco, J. Suffczyński, E. Semenova, A. Miard, A. Lemaître, I. Sagnes, C. Roblin, J. Bloch, and P. Senellart. *Controlled light-matter coupling for a single quantum dot embedded in a pillar microcavity using far-field optical lithography*. Phys. Rev. Lett. **101**, 267404 (2008).

- [64] C. Schneider, A. Huggerberger, M. Gschrey, P. Gold, S. Rodt, A. Forchel, S. Reitzenstein, S. Hfing, and M. Kamp. *In(ga)as/gaas site-controlled quantum dots with tailored morphology and high optical quality*. *physica status solidi (a)* **209**(12), 2379 (2012).
- [65] M. Tavis and F. W. Cummings. *Exact solution for an N-molecule-radiation-field Hamiltonian*. *Phys. Rev.* **170**, 379 (1968).
- [66] H. Primakoff and T. Holstein. *Many-body interactions in atomic and nuclear systems*. *Phys. Rev.* **55**, 1218 (1939).
- [67] B. Besga. *Coherent control with polaritons*. Lecture notes (2014).
- [68] V. Savona. *Polariton Bose-Einstein condensation: Overview and perspectives*. Lecture Notes (2012).
- [69] K. Vahala. *Optical microcavities*. *Nature* **424**, 839 to 846 (2003).
- [70] L. Ferrier, E. Wertz, R. Johne, D. D. Solnyshkov, P. Senellart, I. Sagnes, A. Lemaître, G. Malpuech, and J. Bloch. *Interactions in confined polariton condensates*. *Phys. Rev. Lett.* **106**, 126401 (2011).
- [71] L. für Technische Physik der Universität Würzburg. *Spectroscopy III/V*. website publication. URL [http://www.physik.uni-wuerzburg.de/institute\\_einrichtungen/physikalisches\\_institut/technische\\_physik/tep/work\\_groups/spectroscopy\\_iiiv/](http://www.physik.uni-wuerzburg.de/institute_einrichtungen/physikalisches_institut/technische_physik/tep/work_groups/spectroscopy_iiiv/).
- [72] C. Deutsch. *High finesse Fabry-Pérot resonators: production, characterisation and applications*. Ph.D. thesis, Ludwig-Maximilians Universität München (2008).
- [73] II-IV InfraRed. *Reflective phase retarders*. website catalogue.
- [74] B. Gu and Y. Cui. *Nonparaxial and paraxial focusing of azimuthal-variant vector beams*. *Opt. Express* **20**(16), 17684 (2012).
- [75] L. Andrews. *Special Functions of Mathematics for Engineers: Second Edition* (SPIE Press: Oxford Science Productions, USA, 1998).
- [76] D. Hunger, T. Steinmetz, Y. Colombe, C. Deutsch, T. W. Hänsch, and J. Reichel. *A fiber Fabry-Perot cavity with high finesse*. *New Journal of Physics* **12**(6), 065038 (2010).
- [77] A. Kavokin, J. Baumber, G. Malpuech, and F. Laussy. *Microcavities, Revised Edition* (Oxford University Press, 2011).
- [78] V. Savona. *Linear optical properties of semiconductor microcavities with embedded quantum wells*. *Lecture Notes in Physics* **531**, 174 to 179 (1999).
- [79] C. Symonds, G. Lheureux, J. P. Hugonin, J. J. Greffet, J. Laverdant, G. Brucoli, A. Lemaître, P. Senellart, and J. Bellessa. *Confined tamm plasmon lasers*. *Nano Letters* **13**(7), 3179 (2013).

- [80] C. Deutsch. *High Finesse fibre Fabry-Pérot resonators: Production, characterisation and applications*. Ph.D. thesis, Fakultät für Physik, Ludwig-Maximilians Universität München (2008).
- [81] J. Benedikter, T. Hümmer, M. Mader, B. Schlederer, J. Reichel, T. W. Hänsch, and D. Hunger. *Transverse-mode coupling and diffraction loss in tunable Fabry-Pérot microcavities*. ArXiv e-prints (2015). [1502.01532](#).
- [82] S. Dufferwiel, F. Fras, A. Trichet, P. M. Walker, F. Li, L. Giriunas, M. N. Makhonin, L. R. Wilson, J. M. Smith, E. Clarke, M. S. Skolnick, and D. N. Krizhanovskii. *Strong exciton-photon coupling in open semiconductor microcavities*. Applied Physics Letters **104**(19), 192107 (2014).
- [83] N. Takemura, S. Trebaol, M. Wouters, M. Wouters, M. Portella-Oberli, and B. Deveaud. *Polaritonic feshbach resonance*. Nature Physics **10**, 500 (2014).
- [84] R. O. Umucallar and I. Carusotto. *Fractional Quantum Hall states of photons in an array of dissipative coupled cavities*. Phys. Rev. Lett. **108**, 206809 (2012).
- [85] I. Carusotto, D. Gerace, H. E. Tureci, S. De Liberato, C. Ciuti, and A. Imamoglu. *Fermionized photons in an array of driven dissipative nonlinear cavities*. Phys. Rev. Lett. **103**, 033601 (2009).
- [86] T. Jacqmin, I. Carusotto, I. Sagnes, M. Abbarchi, D. D. Solnyshkov, G. Malpuech, E. Galopin, A. Lemaitre, J. Bloch, and A. Amo. *Direct observation of Dirac cones and a flatband in a honeycomb lattice for polaritons*. Phys. Rev. Lett. **112**, 116402 (2014).
- [87] R. O. Umucallar and I. Carusotto. *Fractional quantum hall states of photons in an array of dissipative coupled cavities*. Phys. Rev. Lett. **108**, 206809 (2012).
- [88] J. Zhao, D. Jin, E. P. Schartner, Y. Lu, Y. Liu, A. V. Zvyagin, L. Zhang, J. M. Dawes, P. Xi, J. A. Piper, E. M. Goldys, , and T. M. Monro. *Single-nanocrystal sensitivity achieved by enhanced upconversion luminescence*. Nature Nanotechnology **8**, 729 (2013).
- [89] R. Albrecht, A. Bommer, C. Deutsch, J. Reichel, and C. Becher. *Coupling of a single nitrogen-vacancy center in diamond to a fiber-based microcavity*. Phys. Rev. Lett. **110**, 243602 (2013).
- [90] H. Kaupp, C. Deutsch, H.-C. Chang, J. Reichel, T. W. Hänsch, and D. Hunger. *Scaling laws of the cavity enhancement for nitrogen-vacancy centers in diamond*. Phys. Rev. A **88**, 053812 (2013).
- [91] L. Rogers, K. Jahnke, T. Teraji, L. Marseglia, C. Müller, B. Naydenov, H. Schauffert, C. Kranz, J. Isoya, L. McGuinness, and F. Jelezko. *Multiple intrinsically identical single-photon emitters in the solid state*. Nature Communications **5** (2014).
- [92] K. Xia and J. Twamley. *Solid state optical interconnect between distant superconducting quantum chips*. ArXiv e-prints (2014). [1408.5972](#).